Title
Cell mechanotype in cancer progression and metastasis

Author
Gill, Navjot Kaur

Publication Date
2018

Peer reviewed|Thesis/dissertation

UNIVERSITY OF CALIFORNIA

Los Angeles

Cell mechanotype in cancer progression and metastasis

A dissertation submitted in partial satisfaction of the

requirements for the degree Doctor of Philosophy

in Molecular, Cellular and Integrative Physiology

by

Navjot Kaur Gill

2018

ABSTRACT OF THE DISSERTATION

Cell mechanotype in cancer progression and metastasis

by

Navjot Kaur Gill

Doctor of Philosophy in Molecular, Cellular and Integrative Physiology

University of California, Los Angeles, 2018

Professor Amy Catherine Rowat, Chair

Cell mechanical phenotype or 'mechanotype' is a label-free biomarker of cell state in physiological and disease contexts ranging from stem cell differentiation to cancer progression. However, to harness deformability as a phenotype for drug screening applications requires a method that can simultaneously measure hundreds of samples in parallel. Moreover, a systems-level understanding of molecular mediators of cellular mechanotype is lacking. In this dissertation, I present a simple and scalable technique, called parallel microfiltration (PMF), to measure cell deformability of multiple samples in parallel. I also demonstrate the application of PMF to screen cancer cells based on their mechanotype across multiple cancer types. This dissertation also demonstrates how PMF can interface with existing high throughput facilities. To achieve high throughput screening using filtration, I developed high-throughput filtration (HTF), which utilizes a customized arrays of individual microfluidic filtration devices in a standard multiwell format to enable mechanotype-screening of hundreds of samples in parallel. Additionally, this dissertation presents a mechanotype-screen of cisplatin-resistant ovarian cancer cells treated with a library of small molecules to identify synergistic anti-cancer drugs. Finally, my thesis also presents an

investigation of key cellular and nuclear molecular mediators of altered cell deformability using these mechanotyping methods; these findings identify novel molecular mediators of cancer cell mechanotype and also provide unique insight into potential mechanisms of a devastating neurological movement disorder, dystonia. Taken together, this dissertation presents novel high throughput cellular mechanotyping methods that enable measurements of cell deformability with unprecedented throughput, which should enable us to harness knowledge of mechanotype to identify novel treatment strategies for cancer and other diseases.

The dissertation of Navjot Kaur Gill is approved.

Lily Wu

Luisa M Iruela-Arispe

Kate Lawrenson

Amy Catherine Rowat, Chair

University of California, Los Angeles

2018

DEDICATION

I dedicate this dissertation to my loving parents, Jatinder Jit Singh Gill and Manjit Kaur Gill. You have always motivated me and inspired me to be my best self. I thank you for always supporting me through everything and always standing by me. I also thank all my mentors leading up to and during this experience. I especially thank Shiladitya Sengupta for his mentorship and support in my life, and Amy Rowat for her mentorship and guidance during my graduate work.

TABLE OF CONTENTS

ACKNOWLEDGEMENTS

Chapter 1. Adapted from *Qi, Gill, et al.* 2015, *Nature Scientific Reports*. ACR, DQ, and NKG designed research; DQ, NKG, and BTH performed research; DQ, NKG, and ACR analyzed data; CS, JS, OD, JYR, and RW contributed cell lines; DQ, NKG, and ACR wrote the paper.

Chapter 2. Adapted from *Gill, et al.* 2018, in press at *Lab on a Chip*. ACR, DQ and NKG invented the technology and designed the experiments. NKG performed all experiments. CL contributed to experiments and data collection. KDN conducted simulations. LL, DQ, BT, and RD contributed to design of the device and experimental setup. OD, JR, RW, BK, KL, MRS and MRF contributed cells and biological insight. NKG and ACR wrote the manuscript. All authors reviewed the manuscript.

Chapter 3. Adapted from *Gill, et al.*, in preparation. NKG conducted the experiments. BT and FA assisted with the experiments. NKG, ACR, RD, KL and BK designed the research. NKG and ACR wrote the manuscript.

Chapter 4. Adapted from *Gill, et al.*, submitted to *Frontiers in Cell and Developmental Biology*. WTD and BB established the cell lines. This work was funded in part by the NIH (R01 GM129374-01 to GWGL, and AR007612 to CAS, RO1 AG047192 to LGF). NKG conducted all experiments. NKG, ACR and GWGL wrote the manuscript.

The Molecular Screening Shared Resource at California NanoSystems Institute and staff supported the high-throughput screening. The Integrated Systems Nanofabrication Cleanroom at the California NanoSystems Institute and its staff supported the fabrication of the microfluidic devices through training and facilities.

The work has been supported by the National Science Foundation (CAREER DBI-1254185 to ACR), Department of Defense (Ovarian Cancer Research Fund Pilot Award), Eureka scholarship and Farber Family Foundation.

VITA

EDUCATION

B. Tech, Biotechnology, specialization in medical biotechnology (2012)

School of Bioengineering, SRM University, Chennai, India

HONORS

Farber Family scholar (2017-2018), Farber Family Scholarship, Los Angeles, CA

Eureka Scholarship (2015-2016), Department of Integrative Biology and Physiology, UCLA

University fellowship (2008-2012), SRM University, Chennai, India

Prime Minister's Merit Scholarship (2008-2012), Government of India

RESEARCH POSITIONS

Molecular, Cellular and Integrative Physiology Graduate Student Researcher (2013-2018), University of California, Los Angeles

Rowat Lab, Department of Integrative Biology and Physiology

Undergraduate Student Researcher (2011-2013), Brigham and Women's Hospital, Boston, MA

Sengupta Lab, Harvard-MIT Health Sciences and Technology

PUBLICATIONS

1. Qi D*, **Gill N*,** Santiskulvong C, Sifuentes J, Dorigo O, Rao J, Harding B, Wiedemeyer R, Rowat A C. "Screening cell mechanotype by parallel microfiltration." *Nature Scientific Reports* (2015). **5**: p. 17595.

2. Kim T H, **Gill N**, Nyberg K D, Nguyen A N, Hohlbauch S V, Geisse N A, Nowell C J, Sloan E K, Rowat A C. "Cancer cells are less deformable and more invasive with activation of beta-adrenergic receptor signaling." *Journal of Cell Science* (2016). **129**(**24**):4563-4575.

3. **Gill N**, Qi D, Kim T H, Chan C, Nguyen A N, Nyberg K D, Rowat A C. “A protocol for screening cells based on deformability using parallel microfiltration.” *Nature Protocol Exchange* (2017). doi:10.1038/protex.2017.101

4. Nyberg K D, Bruce S L, Nguyen A V, Chan C K, **Gill N**, Kim T H, Sloan E K, Rowat A C. Predicting cancer cell invasion by single-cell physical phenotyping. *Integrative Biology* (2018). **10**(4): p. 218-231.

5. Sobreiro M R, Chen J F, Novitskya T, You S, Morley S, Steadman K, **Gill N**, Eskaros A, Rotinen M, Chu C Y, Chung L W K, Tanaka H, Yang W, Knudsen B S, Tseng H R, Rowat A C, Posadas E M, Zijlstra A, Di Vizio D, Freeman M R. “Emerin deregulation links nuclear shape instability to metastatic potential.” *Cancer Research* (2018). **78**(**21**): p. 6085-6097.

MANUSCRIPTS SUBMITTED/UNDER REVIEW

1. **Gill N**, Ly C, Nyberg K, Lee L, Qi D, Tofig B, Reis-Sobreiro M, Dorigo O, Rao J, Wiedemeyer R, Karlan B, Lawrenson K, Freeman M R, Damoiseaux R, Rowat A C. “A scalable filtration method for high throughput screening based on cell deformability.” *Lab on a Chip,* in press.

2. **Gill N**, Ly C, Kim P, Fong L G, Young S G, Saunders C A, Luxton G W G, Rowat A C. “DYT1 dystonia patient-derived fibroblasts have increased deformability and susceptibility to damage by mechanical forces.” *Frontiers in Cell and Developmental Biology*, submitted.

INTRODUCTION

Cell mechanical phenotype, or 'mechanotype', is altered in various physiological and disease contexts, including malignant transformation of cells in cancer[1,2]. During cancer metastasis, primary tumor cells invade adjacent tissues, intravasate into the circulatory system, and colonize a secondary site[3]. Acquisition of invasive cell phenotype in the process of metastasis is marked by epithelial-to-mesenchymal transition (EMT)[4]. During EMT, cells exhibit a progressive loss of epithelial signature markers, such as E-cadherin and laminin-1, as well as gain of characteristic mesenchymal markers, such as vimentin and N-cadherin[4]. In addition to phenotypic and gene expression changes, alteration of cell mechanical properties is observed during invasion; more invasive cancer cells tend to be more compliant than benign tumor cells[5-9]. While the development of treatment strategies targeting hallmark phenotypes of cancer cells[10] has led to significant progress in improving patient survival and disease outcome[11-15], metastasis and recurrence due to chemoresistance remain a major clinical challenge[16-23]. Cell mechanotype could thus be used as an additional target phenotype for identification of synergistic cancer therapeutics.

Parallel microfiltration (PMF) mechanotyping platform

While cell mechanotype has potential as a label-free biomarker for cancer diagnosis[24], to harness deformability—or the ability of cells to deform under mechanical stress—as a phenotype for drug screening applications requires a method that can simultaneously measure hundreds of samples in parallel in a high-throughput manner. Although existing techniques, such as micropipette aspiration[25,26] and atomic force microscopy[8,27], provide detailed insights into viscoelastic behavior of cells, these techniques require sequential measurement of samples, resulting in limited throughput. By contrast, simultaneous measurements of the deformability of multiple samples could enable scale up and application of mechanotyping in drug screening.

This dissertation presents a method, called parallel microfiltration (PMF), for parallel measurements of cell deformability across multiple samples. An applied pressure is used to drive cell suspension through porous membrane of defined pore size; measurements of cell deformability are obtained by quantifying the fraction of sample retained above the membrane. More deformable cells readily deform through the pores and result in reduced retention volume, whereas less deformable cells tend to occlude the pores resulting in higher retention volume. Using PMF, human ovarian cancer cells with induced EMT by overexpression of transcription factors (Snail, Slug) are found to be more deformable than the epithelial-type cells. Moreover, I found that cisplatin-resistant ovarian cancer cells are more deformable compared to drug-sensitive cells[28,29].

This thesis also presents a high throughput filtration (HTF) method, which enables the parallel microfiltration technology to interface with existing high throughput facilities and enable screening of cells. The core of HTF is a custom-fabricated array of 96 microfiltration devices; each device contains a series of pillars with well-defined micron-scale gaps that are smaller than the diameter of single cells. Cells are driven to passively deform through the gaps in response to applied pressure. The ability of cells to deform through the gaps determines the fluidic resistance of a single device; less deformable cells occlude the gaps and result in less flow through the filtration device, and thus a smaller filtrate volume. Multiwell input and rapid measurements of the output filtrate volume using plate reader enable integration of HTF in automated sample handling platforms. HTF measurements are validated by filtration of epithelial and mesenchymal-type ovarian cancer cells in parallel, malignant versus benign breast cancer cells, prostate cancer cells with varying invasive ability, cells treated with common chemotherapy drug, paclitaxel, as well as cytoskeletal and nuclear perturbing drugs that modulate cell deformability.

High-throughput cell mechanotype screening

Phenotypic assays provide a promising approach to identify effective drugs[30]. Typical screens based on molecular readouts, such as gene or protein expression[31-33], and cellular metrics, such as proliferation[34,35], apoptosis[36,37], or invasion[38,39], have successfully identified anti-cancer drugs with clinical efficacy[40,41]. Since the deformability of cancer cells is associated with cellular invasion[42-45], compounds that make cancer cells stiffer may also decrease their invasion. Harnessing the intrinsic deformability of cells as an alternative phenotype for screening thousands of compounds in chemical libraries has exciting potential to identify synergistic anti-cancer drugs.

This dissertation presents the first high throughput cell deformability-based screen. Using the PMF mechanotyping platform, cisplatin-resistant human ovarian cancer cells are screened against the Library of Pharmacologically Active Compounds (LOPAC), containing 1280 FDA-approved small molecules; hits are identified as compounds that lead to significant decrease in deformability of cells. Follow-up assays confirm the effects of lead compounds on cell deformability, viability, cell cycle stage, and invasion. This unprecedented ability to screen cells based on their deformability also enables meta-analysis to identify key molecular hubs underlying the altered cell mechanotype.

Molecular mediators of cell mechanotype

While the role of cytoskeleton components, such as actin, microtubules, and intermediate filaments, in regulation of cell mechanotype is well established[46-48], the role of nuclear proteins in mediating cell mechanotype is not well understood. This work highlights application of PMF mechanotyping technology to enable targeted mechanistic studies to investigate key molecular mediators that regulate cell deformability. Specifically, I found that mechanical integration of the nucleus and cytoskeleton via linkers of nucleoskeleton and cytoskeleton (LINC) complex and associated proteins play a critical role in regulating deformability of cells. I found that deletion of

or loss-of-function mutation in genes encoding the components of the LINC complex and associated proteins, relevant in devastating physiological disorders, such as progeria[49] and dystonia[50], lead to significant changes in cell deformability. I also extended these findings to provide insight into DYT1 dystonia, a neurological movement disorder, that is caused by a loss-of-function mutation in the *DYT1*/*TOR1A* gene that encodes torsinA protein[50]. Fibroblasts isolated from DYT1 dystonia patients exhibit increased deformability compared to normal fibroblasts, and after exposure to mechanical stretching, DYT1 fibroblasts exhibit nuclei with greater strain and decreased cell viability. These findings further establish altered cell mechanotype as a potential mechanism driving pathogenesis of diverse diseases, from cancer to dystonia.

References

1. D. A. Fletcher and D. Mullins, *Nature*, 2010. Cell mechanics and the cytoskeleton. **463**(7280): p. 485-492.
2. S. Suresh, *Acta Biomater*, 2007. Biomechanics and biophysics of cancer cells. **3**(4): p. 413-38.
3. S. Valastyan and R. A. Weinberg, *Cell*, 2011. Tumor metastasis: molecular insights and evolving paradigms. **147**(2): p. 275-92.
4. R. Kalluri and R. A. Weinberg, *J Clin Invest*, 2009. The basics of epithelial-mesenchymal transition. **119**(6): p. 1420-8.
5. V. Swaminathan, K. Mythreye, E. T. O'Brien, A. Berchuck, G. C. Blobe and R. Superfine, *Cancer Res*, 2012. Mechanical stiffness grades metastatic potential in patient tumor cells and in cancer cell lines. **71**(15): p. 5075-80.
6. W. Xu, R. Mezencev, B. Kim, L. Wang, J. McDonald and T. Sulchek, *PLoS One*, 2012. Cell Stiffness Is a Biomarker of the Metastatic Potential of Ovarian Cancer Cells. **7**: p. e46609.

7. M. Plodinec, M. Loparic, C. A. Monnier, E. C. Obermann, R. Zanetti-Dallenbach, P. Oertle, J. T. Hyotyla, U. Aebi, M. Bentires-Alj, R. Y. Lim and C. A. Schoenenberger, *Nat Nanotechnol*, 2012. The nanomechanical signature of breast cancer. **7**(11): p. 757-65.

8. S. E. Cross, Y. S. Jin, J. Rao and J. K. Gimzewski, *Nat Nanotechnol*, 2007. Nanomechanical analysis of cells from cancer patients. **2**: p. 780-783.

9. J. Guck, S. Schinkinger, B. Lincoln, F. Wottawah, S. Ebert, M. Romeyke, D. Lenz, H. M. Erickson, R. Ananthakrishnan, D. Mitchell, J. Kas, S. Ulvick and C. Bilby, *Biophys J*, 2005. Optical deformability as an inherent cell marker for testing malignant transformation and metastatic competence. **88**(5): p. 3689-98.

10. D. Hanahan and R. A. Weinberg, *Cell*, 2011. Hallmarks of cancer: the next generation. **144**(5): p. 646-74.

11. J. K. Chan, M. K. Cheung, A. Husain, N. N. Teng, D. West, A. S. Whittemore, J. S. Berek and K. Osann, *Obstet Gynecol*, 2006. Patterns and progress in ovarian cancer over 14 years. **108**(3 Pt 1): p. 521-8.

12. J. D. Wright, L. Chen, A. I. Tergas, S. Patankar, W. M. Burke, J. Y. Hou, A. I. Neugut, C. V. Ananth and D. L. Hershman, *Obstet Gynecol*, 2015. Trends in relative survival for ovarian cancer from 1975 to 2011. **125**(6): p. 1345-52.

13. T. Shimada, T. Saito, M. Shimokawa, K. Shimamoto, S. Matsushita, S. Yamaguchi, K. Ariyoshi and M. Okadome, *Jpn J Clin Oncol*, 2017. Improvement in the prognosis of ovarian cancer in the era before addition of molecular targeting therapy. **47**(6): p. 494-498.

14. A. Kim, Y. Ueda, T. Naka and T. Enomoto, *J Exp Clin Cancer Res*, 2012. Therapeutic strategies in epithelial ovarian cancer. **31**: p. 14.

15. J. Y. Lee, S. Kim, Y. T. Kim, M. C. Lim, B. Lee, K. W. Jung, J. W. Kim, S. Y. Park and Y. J. Won, *BMC Cancer*, 2018. Changes in ovarian cancer survival during the 20 years before the era of targeted therapy. **18**(1): p. 601.

16. C. N. Qian, Y. Mei and J. Zhang, *Chin J Cancer*, 2017. Cancer metastasis: issues and challenges. **36**(1): p. 38.

17. H. Zahreddine and K. L. Borden, *Front Pharmacol*, 2013. Mechanisms and insights into drug resistance in cancer. **4**: p. 28.

18. T. R. Wilson, P. G. Johnston and D. B. Longley, *Curr Cancer Drug Targets*, 2009. Anti-apoptotic mechanisms of drug resistance in cancer. **9**(3): p. 307-19.

19. P. S. Steeg, *Nat Rev Cancer*, 2016. Targeting metastasis. **16**(4): p. 201-18.

20. X. Guan, *Acta Pharm Sin B*, 2015. Cancer metastases: challenges and opportunities. **5**(5): p. 402-18.

21. P. S. Steeg and D. Theodorescu, *Nat Clin Pract Oncol*, 2008. Metastasis: a therapeutic target for cancer. **5**(4): p. 206-19.

22. I. J. Fidler and M. L. Kripke, *Cancer Metastasis Rev*, 2015. The challenge of targeting metastasis. **34**(4): p. 635-41.

23. M. Nikolaou, A. Pavlopoulou, A. G. Georgakilas and E. Kyrodimos, *Clin Exp Metastasis*, 2018. The challenge of drug resistance in cancer treatment: a current overview. **35**(4): p. 309-318.

24. H. T. Tse, D. R. Gossett, Y. S. Moon, M. Masaeli, M. Sohsman, Y. Ying, K. Mislick, R. P. Adams, J. Rao and D. Di Carlo, *Sci Transl Med*, 2013. Quantitative diagnosis of malignant pleural effusions by single-cell mechanophenotyping. **5**(212): p. 212ra163.

25. R. M. Hochmuth and D. Needham, *Biorheology*, 1990. The viscosity of neutrophils and their transit times through small pores. **27**(6): p. 817-28.

26. S. Chien and K. L. P. Sung, *Biophysical Journal*, 1984. Effect of Colchicine on Viscoelastic Properties of Neutrophils. **46**(3): p. 383-386.

27. M. J. Rosenbluth, W. A. Lam and D. A. Fletcher, *Biophys J*, 2006. Force microscopy of nonadherent cells: a comparison of leukemia cell deformability. **90**(8): p. 2994-3003.

28. D. Qi, N. Kaur Gill, C. Santiskulvong, J. Sifuentes, O. Dorigo, J. Rao, B. Taylor-Harding, W. Ruprecht Wiedemeyer and A. C. Rowat, *Sci Rep*, 2015. Screening cell mechanotype by parallel microfiltration. **5**: p. 17595.

29. M. A. Tsai, R. E. Waugh and P. C. Keng, *Biophys J*, 1998. Passive mechanical behavior of human neutrophils: effects of colchicine and paclitaxel. **74**(6): p. 3282-91.

30. D. C. Swinney, *Clin Pharmacol Ther*, 2013. Phenotypic vs. target-based drug discovery for first-in-class medicines. **93**(4): p. 299-301.

31. K. Guo, A. A. Shelat, R. K. Guy and M. B. Kastan, *J Biomol Screen*, 2014. Development of a cell-based, high-throughput screening assay for ATM kinase inhibitors. **19**(4): p. 538-46.

32. T. Miyagi, B. Shiotani, R. Miyoshi, T. Yamamoto, T. Oka, K. Umezawa, T. Ochiya, M. Takano and H. Tahara, *Cancer Sci*, 2014. DSE-FRET: A new anticancer drug screening assay for DNA binding proteins. **105**(7): p. 870-4.

33. A. M. Baker, W. Huang, X. M. Wang, M. Jansen, X. J. Ma, J. Kim, C. M. Anderson, X. Wu, L. Pan, N. Su, Y. Luo, E. Domingo, T. Heide, A. Sottoriva, A. Lewis, A. D. Beggs, N. A. Wright, M. Rodriguez-Justo, E. Park, I. Tomlinson and T. A. Graham, *Nat Commun*, 2017. Robust RNA-based in situ mutation detection delineates colorectal cancer subclonal evolution. **8**(1): p. 1998.

34. H. L. Martin, M. Adams, J. Higgins, J. Bond, E. E. Morrison, S. M. Bell, S. Warriner, A. Nelson and D. C. Tomlinson, *PLoS One*, 2014. High-content, high-throughput screening for the identification of cytotoxic compounds based on cell morphology and cell proliferation markers. **9**(2): p. e88338.

35. A. H. Wong, H. Li, Y. Jia, P. I. Mak, R. Martins, Y. Liu, C. M. Vong, H. C. Wong, P. K. Wong, H. Wang, H. Sun and C. X. Deng, *Sci Rep*, 2017. Drug screening of cancer cell lines and human primary tumors using droplet microfluidics. **7**(1): p. 9109.

36. L. Zhang, Z. Yang, L. Granieri, A. Pasculescu, A. Datti, S. L. Asa, Z. Xu and S. Ezzat, *Oncotarget*, 2016. High-throughput drug library screening identifies colchicine as a thyroid cancer inhibitor. **7**(15): p. 19948-59.

37. O. S. Frankfurt and A. Krishan, *Anticancer Drugs*, 2003. Apoptosis-based drug screening and detection of selective toxicity to cancer cells. **14**(7): p. 555-61.

38. N. A. Evensen, J. Li, J. Yang, X. Yu, N. S. Sampson, S. Zucker and J. Cao, *PLoS One*, 2013. Development of a high-throughput three-dimensional invasion assay for anti-cancer drug discovery. **8**(12): p. e82811.

39. H. A. Kenny, M. Lal-Nag, E. A. White, M. Shen, C. Y. Chiang, A. K. Mitra, Y. Zhang, M. Curtis, E. M. Schryver, S. Bettis, A. Jadhav, M. B. Boxer, Z. Li, M. Ferrer and E. Lengyel, *Nat Commun*, 2015. Quantitative high throughput screening using a primary human three-dimensional organotypic culture predicts in vivo efficacy. **6**: p. 6220.

40. G. Cassinelli, *Tumori*, 2016. The roots of modern oncology: from discovery of new antitumor anthracyclines to their clinical use. **2016**(3): p. 226-35.

41. G. W. Aherne, E. McDonald and P. Workman, *Breast Cancer Res*, 2002. Finding the needle in the haystack: why high-throughput screening is good for your health. **4**(4): p. 148-54.

42. W. Xu, R. Mezencev, B. Kim, L. Wang, J. McDonald and T. Sulchek, *PLoS One*, 2012. Cell stiffness is a biomarker of the metastatic potential of ovarian cancer cells. **7**(10): p. e46609.

43. T. H. Kim, N. K. Gill, K. D. Nyberg, A. V. Nguyen, S. V. Hohlbauch, N. A. Geisse, C. J. Nowell, E. K. Sloan and A. C. Rowat, *J Cell Sci*, 2016. Cancer cells become less deformable and more invasive with activation of beta-adrenergic signaling. **129**(24): p. 4563-4575.

44. A. V. Nguyen, K. D. Nyberg, M. B. Scott, A. M. Welsh, A. H. Nguyen, N. Wu, S. V. Hohlbauch, N. A. Geisse, E. A. Gibb, A. G. Robertson, T. R. Donahue and A. C. Rowat,

Integr Biol (Camb), 2016. Stiffness of pancreatic cancer cells is associated with increased invasive potential. **8**(12): p. 1232-1245.

45. K. D. Nyberg, S. L. Bruce, A. V. Nguyen, C. K. Chan, N. K. Gill, T. H. Kim, E. K. Sloan and A. C. Rowat, *Integr Biol (Camb)*, 2018. Predicting cancer cell invasion by single-cell physical phenotyping. **10**(4): p. 218-231.
46. A. F. Pegoraro, P. Janmey and D. A. Weitz, *Cold Spring Harb Perspect Biol*, 2017. Mechanical Properties of the Cytoskeleton and Cells. **9**(11).
47. R. C. Donehower, *Stem Cells*, 1996. The clinical development of paclitaxel: a successful collaboration of academia, industry and the National Cancer Institute. **14**(1): p. 25-8.
48. J. E. Liebmann, J. A. Cook, C. Lipschultz, D. Teague, J. Fisher and J. B. Mitchell, *Br J Cancer*, 1993. Cytotoxic studies of paclitaxel (Taxol) in human tumour cell lines. **68**(6): p. 1104-9.
49. N. Y. Chen, P. Kim, T. A. Weston, L. Edillo, Y. Tu, L. G. Fong and S. G. Young, *Proc Natl Acad Sci U S A*, 2018. Fibroblasts lacking nuclear lamins do not have nuclear blebs or protrusions but nevertheless have frequent nuclear membrane ruptures. **115**(40): p. 10100-10105.
50. L. Ozelius, J. Hewett, C. Page, S. Bressman, P. Kramer, C. Shalish, D. de Leon, M. Brin, D. Raymond, D. Corey, S. Fahn, N. Risch, A. Buckler, J. Gusella and X. Breakefield, *Nat Genet*, 1997. The early-onset torsion dystonia gene (DYT1) encodes an ATP-binding protein. **17**(1): p. 40-8.

CHAPTER 1

Screening Cell Mechanotype by Parallel Microfiltration

Abstract

Cell mechanical phenotype or 'mechanotype' is emerging as a valuable label-free biomarker. For example, marked changes in the viscoelastic characteristics of cells occur during malignant transformation and cancer progression. Here we describe a simple and scalable technique to measure cell mechanotype: this parallel microfiltration assay enables multiple samples to be simultaneously measured by driving cell suspensions through porous membranes. To validate the method, we compare the filtration of untransformed and $HRas^{V12}$-transformed murine ovary cells and find significantly increased deformability of the transformed cells. Inducing epithelial-to-mesenchymal transition (EMT) in human ovarian cancer cells by overexpression of key transcription factors (Snail, Slug, Zeb1) or by acquiring drug resistance produces a similar increase in deformability. Mechanistically, we show that EMT-mediated changes in epithelial (loss of E-Cadherin) and mesenchymal markers (vimentin induction) correlate with altered mechanotype. Our results demonstrate a method to screen cell mechanotype that has potential for broader clinical application.

Introduction

Cells are viscoelastic materials whose mechanotype is altered in diseases from malaria to cancer[1,2]. For example, malignant cells across different types of cancers are consistently 2-5× softer than benign cells both *in vitro* and *in situ*[3-6]. Cell mechanotype also grades metastatic potential: highly invasive human ovarian carcinoma cells are up to 5× softer than less invasive cells[3,4]. Mechanotyping of patient samples shows potential for clinical diagnoses of cancer[7]. Moreover, the compliance of cancer cells is altered by chemotherapy drugs. For example,

leukemia cells exhibit a ~10^2-fold increase in elastic modulus after being treated with dexamethasone and daunorubicin[8]. While cell mechanotype has potential as a biomarker in cancer diagnosis and for identifying effective drug treatments, to efficiently screen cell mechanotype for fundamental research and clinical applications requires a simple and scalable method.

Various techniques provide quantitative insight into the viscoelastic behavior of cells including micropipette aspiration[9,10], atomic force microscopy[6,11], and cantilever compression[12,13]. These methods enable detailed characterization of the force-deformation response of typically <10^2 individual cells, which limit the number of independent samples that can be probed within a reasonable timescale. An alternative way to measure cell deformability is to filter cells through membranes with micron-scale pores[14-16]; however, these measurements are performed sequentially, which limits scale-up. More recently, microfluidic methods enable more efficient measurements of cell mechanotype: real-time deformability cytometry probes the deformation of single cells at ~100 cells/s[17] and requires over 1 hour to obtain data on a single sample from the initial state of cells in culture. Cells can also be deformed by the shear and compressive stresses generated as cells flow through micron-scale constrictions[18-20], or through opposing fluid streams[21]; while these methods enable measurements at rates of up to ~2,000 cells/sec, the total measurement time for a single sample is approximately 1.5 hours as high-speed imaging and intensive computational analysis is required; this also challenges the measurement of different samples in parallel. If we could rapidly assess the deformability of multiple samples in a single measurement, we could harness the intrinsic mechanotype of cells for practical applications.

Here we describe a parallel microfiltration (PMF) method that enables simultaneous measurements of cell mechanotype across multiple samples. We use uniform air pressure to drive cell suspensions through porous membranes; the relative deformability of a cell sample is

quantified by the fraction of sample retained above the membrane. Herein we describe PMF design principles and operation parameters. Based on our experimental results and theoretical considerations, we develop a simple model that provides a physical explanation of PMF and allows us to relate our experimental data to cell deformability. We validate the method by mechanotyping a variety of cancer cell types, including epithelial and mesenchymal-type cells, as well as cells treated with chemotherapy drugs. We focus on human promyelocytic leukemia (HL-60) and ovarian cancer cells, as the mechanotype of these cells has been characterized using other complementary techniques[3,4,11,22,23].

Results

Parallel microfiltration concept. The essential components of the PMF device are shown in **Figure 1a**. Polycarbonate membranes are sandwiched between two custom-fabricated 96-well plates; using membranes with varying pore sizes can enable filtration through multiple pore sizes in a single run. We place cell suspensions in the top wells, and apply a uniform pressure gradient across the membrane for a defined period of time. To quantify the filtration of each individual cell sample, we measure the fraction of the initial mass of cell suspension that is retained in the top well, which is the percentage (%) retention; equivalently, the number of retained cells can also be measured (**Supplementary Fig. 1**).

Modeling membrane filtration. To understand the essential operation parameters and physical mechanism underlying PMF, we consider fluid flow through porous media, as described by Darcy's Law, $Q = dV/dt = \Delta PAk/L\mu$, where Q is the flow rate; V, the flow volume; t, the time; ΔP, the pressure applied to drive the cell suspension to flow through the micron-scale pores; A, the cross-sectional flow area; L, the membrane thickness; μ, the dynamic viscosity of the cell medium; and k, the membrane permeability. When a cell is larger than a pore, it is subject to external stresses that cause it to deform. Whether or not a cell occludes a pore depends on the

driving pressure, cell and pore sizes, surface properties, and the cell's intrinsic mechanical properties[9,24]. In each experiment, we maintain constant driving pressure and consistent cell-to-pore size ratios across different cell samples (**Supplementary Fig. 2**). Previous observations show that the viscoelastic properties of cells, rather than surface interactions, dominate their deformation into a micron-scale pore[25]; we also minimize surface interactions by passivating the wells prior to filtration (**Methods**). We cannot exclude that altered cell surface properties contribute to cell filtration behavior, since friction forces between the cell and pore depend on both cell surface properties[25] and deformability[26]. Yet cell deformability plays a central role in % retention measurements: we observe major decrease in % retention for cells whose F-actin structures are disrupted by treatment with cytochalasin D **(Supplementary Fig. 3)**. On the other hand, stabilization of F-actin with colchicine treatment results in increased % retention (**Supplementary Fig. 3a**). These results are consistent with previous reports of how pharmacologic and genetic perturbations of cytoskeletal or nuclear structures impact the ability of cells to deform through micron-scale pores; these perturbations primarily alter cell deformability, rather than cell surface properties[18,25]. Taken together, these results substantiate that the fraction of cells that occlude the pores at a set pressure depends on differences in cell mechanical properties[8,19] and dictates the total volumetric flow: a larger fraction of occluded pores results in less flow through the membrane, and consequently fewer cells will transit through the pores.

To model the filtration process, we consider the time-dependence of membrane occlusion. In a given time window, Δt, a defined number of cells, *N*, that arrive at the membrane and transit the pores is determined by

$$N(\Delta t) = \sum_{i=0}^{j-1} n_0(1-\chi)^i \qquad (1)$$

where n_0 is the total number of pores in the filtration area, χ is the fraction of cells that occlude the pores, and j is the total number of iterations. We fit this simple model to the measured filtration data by adjusting only one parameter, χ, which reflects cell mechanotype. A lower χ value indicates that a smaller fraction of cells occlude the pores; this is consistent with a sample of softer cells, the majority of which readily deform through the micron-scale constrictions in response to applied pressure. By contrast, a higher χ value indicates that a larger fraction of cells occlude the pores on the experimental timescale, reflecting a sample of cells that are on average more resistant to deforming through pores of a particular size at a given pressure[18,19,24].

Optimizing sample cell density. The cell density is critical for filtration: with a low cell density, the number of pores exceeds the number of cells, and there is negligible change in the cell suspension flow rate. By contrast, if the cell density is too high, pores are rapidly occluded; similar jamming phenomenon is observed for colloidal suspensions[27-29]. To establish a suitable cell density for filtration, we determine the % retention of HL-60 and ovarian cancer cell samples across a range of densities from ~10^5 to 10^7 cells/ml. With increasing cell density we observe that the percentage of sample retained increases monotonically (**Fig. 1b**). One possible origin of this increased retention could be an increased viscosity of the cell suspension due to the higher cell density. However, according to Einstein's equation to describe the effect of particle volume fraction, ϕ, on viscosity, $\eta = \eta_s(1+2.5\phi)$, where η_s is the solvent/medium viscosity. By Darcy's law, the increase in viscosity between cell samples with concentrations of 10^5 *versus* 10^7 cells/ml would result in less than a 2% variation in suspension flow rate. Thus, the observed ~3-fold increase in % retention cannot be attributed to the altered viscosity of the cell suspension but rather the progressive occlusion of pores.

To evaluate how well our model describes the data, we obtain the best fit of **Equation 1** with χ as the sole fitting parameter (**Fig. 1b,c**). For filtration through 5 μm pores, χ = 0.44, whereas χ = 0.05 for 8 μm pores, reflecting that a smaller fraction of cells occlude the larger pores. Importantly, these results guide us to choose an initial density of less than 10^6 cells/ml, which equates to a cell-to-pore number ratio of ~10 and ensures measurable filtration in the regime below which % retention saturates with increasing cell density.

Establishing membrane pore size and filtration pressure. When setting up PMF to assay a particular cell type, both pore size and applied pressure must be selected to optimize the dynamic range of filtration. The cell-to-pore size ratio is typically ~1.2 – 3.1 (**Supplementary Fig. 2**). The optimal driving pressure depends on the fluidic resistance of the membrane, which is determined by its physical characteristics, such as the size and density of pores, as well as the physical properties of the cells. The applied pressure should be large enough to ensure that cells can deform and transit across the membrane, yet not so excessive that all cells transit through, precluding any measurement of cell mechanotype. To validate PMF, we use HL-60 cells, whose mechanical properties are well characterized[11,30]. We establish the driving pressure for filtration through 5 μm pore membranes by performing a pressure sweep from 0.7 to 6.2 kPa. Across this pressure range, we observe a linear dependence of % retention on pressure (**Fig. 1c**). We then simultaneously filter HL-60 cells and neutrophil-type HL-60 (dHL-60) cells that are differentiated using all-trans retinoic acid (ATRA). These two cell types have similar sizes (**Supplementary Fig. 2**) but distinct mechanical properties[11,30]. While the pressure response is linear for both cell types, there is a marked difference in slope (**Fig. 1c**), reflecting the difference in cell mechanotype. Fitting our model to this data reveals a larger χ parameter for HL-60 cells (χ = 0.19, R^2 = 0.93) than dHL-60 cells (χ = 0.07, R^2 = 0.99), indicating that dHL-60 cells are softer than HL-60 cells. Our results are consistent with previous findings that dHL-60 cells are 2-fold more compliant than HL-60

cells[30], and have a lower Young's modulus, $E_{dHL\text{-}60}$ ~156 Pa *versus* $E_{HL\text{-}60}$ cells ~855 Pa[11]. We also analyze the pair of human ovarian cancer cells, OVCA433-GFP (control) and OVCA433 that overexpresses *SNAI1*=Snail (OVCA433-Snail) that has undergone epithelial-to-mesenchymal transition (EMT). Previous studies indicate that cancer cell mechanotype is altered with EMT[22,23,31,32]. We observe that the mesenchymal-like OVCA433-Snail cells are softer than the OVCA433-GFP control cells, as shown by the greater reduction in % retention with increasing pressure; fitting our model to this data reveals a larger χ parameter for the OVCA433-GFP cells (χ = 0.05, R^2 =0.95) compared to the OVCA433-Snail cells (χ = 0.01, R^2 = 0.69).

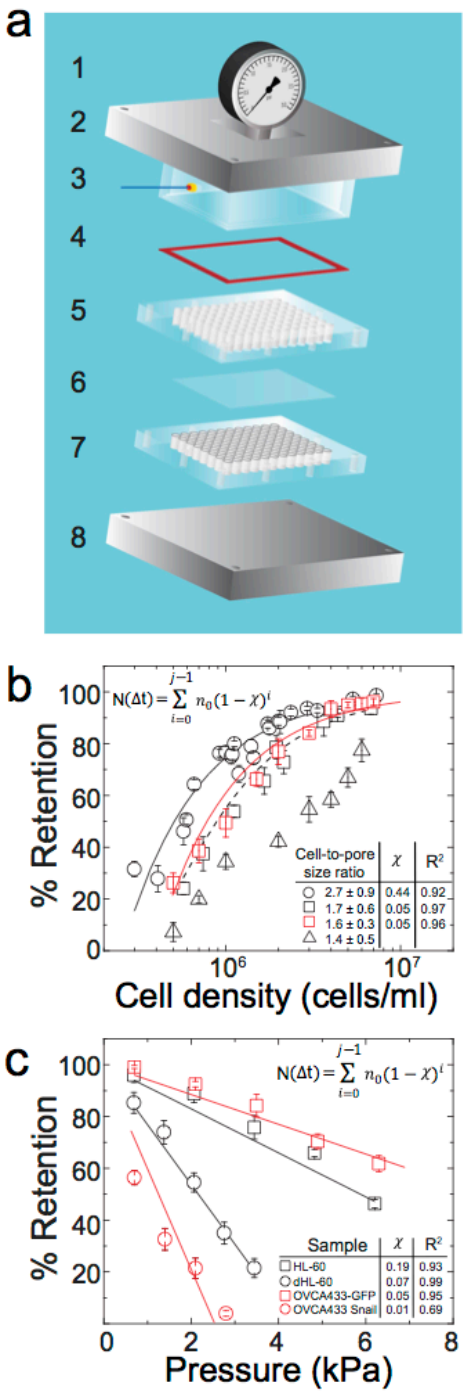

Figure 1 | **Overview of the parallel microfiltration (PMF) platform. (a)** Schematic illustration of the parallel filtration platform. 1: Pressure gauge; 2: Aluminum plate for assembling; 3: Pressure chamber. An air pressure source (**Supplementary Fig. 10**) connects *via* the blue tube; 4: Silicone sealing pad; 5: 96-well loading plate; 6: Porous membrane; 7: 96-well bottom plate with O-rings (black); 8: Aluminum plate for assembling. **(b)** Dependence of HL-60 cell filtration on cell density through membranes of 5, 8, and 10 μm pores. Black circles: 5 μm pore membrane, 3.4 kPa applied for 20 s; black squares: 8 μm pore membrane, 0.7 kPa applied for 20 s; black triangles: 10 μm pore membrane, 0.7 kPa applied for 20 s. Red squares show filtration of ovarian cancer

cells (OVCA433-Snail) through 10 μm pore membrane, 2.1 kPa for 50s. Lines represent model fitting obtained using the least squares method: solid lines for fitting data shown by black circles and red squares; fitting of the black squares is denoted with a dashed line. **(c)** Pressure dependence of HL-60 control (black squares) *versus* ATRA-treated (dHL-60, black circles) cell filtration with 5 μm pore membrane for 20 s. Filtration of ovarian cancer cells OVCA433-GFP control (red squares) *versus* OVCA433-Snail (red circles) with 10 μm pore membrane for 50 s. For **b** and **c**, filtration and modeling parameters are shown in the insets. Solid lines represent model fitting obtained using the least squares method. Each data point represents mean ± S.D.

Predicting epithelial *versus* mesenchymal-type cells based on mechanotype. To test the utility of PMF in screening cancer cell mechanotype, we establish a pore size of 10 μm and driving pressure of 2.1 kPa (**Fig. 1c**) for filtration of representative epithelial and mesenchymal-type ovarian cancer cells (**Fig. 2d**). We first validate how transformation of murine ovarian surface epithelial cells (MOSE) by the *HRAS^{V12}* oncogene[33] impacts cell filtration. The mock-transformed (pWZL) MOSE cells show 90 ± 1% retention, whereas the HRas^{V12}-expressing MOSE cells show 32 ± 3% retention, indicating the transformed cells are more deformable (**Fig. 2a**). The MOSE-HRas^{V12} cells also show reduced E-cadherin and elevated vimentin levels, which is consistent with mesenchymal phenotype (**Fig. 2b**). Another hallmark of mesenchymal-type cells is their greater propensity for colony formation in soft agar compared to epithelial-type cells[34]. Indeed, the MOSE-HRas^{V12} cells form a larger number of colonies compared to the mock-transformed control (**Supplementary Fig. 4**). We also tested MOSE cells engineered to overexpress cyclin E1, which is encoded by *CCNE1,* a less potent oncogene in this system. These cells express similar levels of E-Cadherin as the MOSE control cells and form only a small number of colonies in soft agar (**Supplementary Fig. 4**). Consistent with their epithelial phenotype, MOSE-Cyclin E1 cells exhibit similar retention to the MOSE control cells (**Fig. 2a**).

HRAS^{V12}-mediated transformation is accompanied by EMT (**Fig. 2**), which has critical implications in cancer: cells with mesenchymal phenotype exhibit enhanced motility and increased propensity to detach from the primary tumor[35]. While key changes in protein expression, such as the reduction in E-Cadherin and increase in vimentin during EMT are well-studied[36,37], the changes that occur in mechanotype are not fully understood. Therefore, we next ask if EMT itself leads to

increased deformability. To address this question, we probe two individual clones of the human ovarian cancer cell line SKOV3 that underwent EMT, acquiring the mesenchymal phenotype in the process of becoming drug-resistant. Both SKOV3^{EMT1} and SKOV3^{EMT2} clones exhibit a reduction in E-cadherin expression (**Fig. 2b**); they also show a reduced % retention compared to the control SKOV3 cells (**Fig. 2a**). These results suggest that the process of EMT is accompanied by reduced stiffness.

To test this hypothesis directly, we overexpress single genes that are master regulators of EMT (*SNAI1*=Snail, *SNAI2*=Slug, *ZEB1*=Zeb1). Here, we use a human ovarian cancer cell line, OVCA433, which has high endogenous levels of E-cadherin. We introduce human transgenes for Snail, Slug and Zeb1 by lentiviral infection and compare the resulting sublines by filtration. Similar to previous results in the SKOV3$^{EMT1/2}$ cell lines, EMT-altered OVCA433 cells have increased deformability, as shown by the lower % retention of the modified cells compared to the non-modified control (**Fig. 1c, Fig. 2a).**

Evaluating the % retention across the entire panel of EMT cells reveals that the mean % retention of all epithelial-like cells is significantly higher than the mesenchymal-like cells, indicating that epithelial-type cells are more resistant to deformation through micron-scale pores than those with mesenchymal phenotype (**Fig. 2a, Supplementary Fig. 5a**). By Western blot analysis, we confirm that across our panel of 10 different EMT related cell types, all samples with retention above 80% are epithelial-like cells and express (i) increased levels of E-Cadherin and/or (ii) decreased levels of vimentin compared to cells with mesenchymal phenotype that show below 65% retention (**Fig. 2b,c**). While epithelial and mesenchymal-type cells show distinct morphologies in culture, the size distributions of cells in suspension are similar, and there is a weak correlation of cell-to-pore size ratio with % retention, indicating that cell size does not significantly alter % retention (**Supplementary Fig. 2c,** correlation coefficient 0.14). Importantly we observe a single large peak

in the cell size distributions, indicating that clustering of epithelial-type cells is not a major contributor to pore occlusion. Imaging of membranes after filtration confirms that 93-98% of occluded pores are occluded by single cells (**Supplementary Fig. 6)**; these results also show that cells do not undergo lysis as they occlude pores. We cannot exclude that altered friction between the cell and wall may impact % retention, especially as cell deformability affects the normal force exerted on the cell, and thus softer cells may experience reduced friction[26]. Indeed, cells with increased metastatic potential show reduced surface friction during transit through pores[38]. However, we do not observe any increase in % retention when mesenchymal-type cells are filtered with BSA treatment that blocks cell-surface interactions (**Supplementary Fig. 7).** We also confirm there are no observable differences in non-specific binding across cell lines (**Supplementary Table 1**). In addition, we find a marked >3-fold reduction in % retention when epithelial-type OVCA433-GFP cells are treated with cytochalasin D (**Supplementary Fig. 3**); these results substantiate that mechanotype plays a major role in determining % retention.

To determine if PMF could inform the user of cell phenotype based on mechanotype alone, we conduct a blind screen across the EMT panel of cell lines, whose identities are not known to the user. These results show that PMF can be used to predict whether cells are more likely to be mesenchymal- or epithelial-like based on their mechanotype (**Supplementary Fig. 5**). We confirm the EMT phenotype of these samples by immunoblotting (**Supplementary Fig. 8**).

To gain insight into the molecular origins of the altered mechanotype in EMT, we perform immunofluorescence and confocal microscopy to investigate the organization of key structural components, such as actin, microtubules, and the nucleus, which are major contributors to mechanotype[8,18,39,40]. We focus our analysis on pairs of cells that exhibit marked differences in mechanotype: mesenchymal-type cells (MOSE $HRAS^{V12}$, OVCA433 ZEB1) show an increased density of cortical actin compared to the control cells (MOSE pWZL blast, OVCA433-GFP) (**Fig.**

2e,f). There are neither observable differences in microtubule structure nor in cell nucleus morphology (**Fig. 2e,g**). We also investigate the nuclear-to-cytoplasmic size ratio, which could also impact cell filtration rates. While the reduced nuclear-to-cytoplasmic size ratio of the Zeb1-expressing cells could help to explain their reduced % retention, the nuclear-to-cytoplasmic size ratio is not significantly different between MOSE HRAS^{V12} and the control pWZL blast cells **(Supplementary Fig. 9)**. Therefore, a reduced nuclear-to-cytoplasmic size ratio is not sufficient to explain the softer mechanotype we observe for all mesenchymal-type cells.

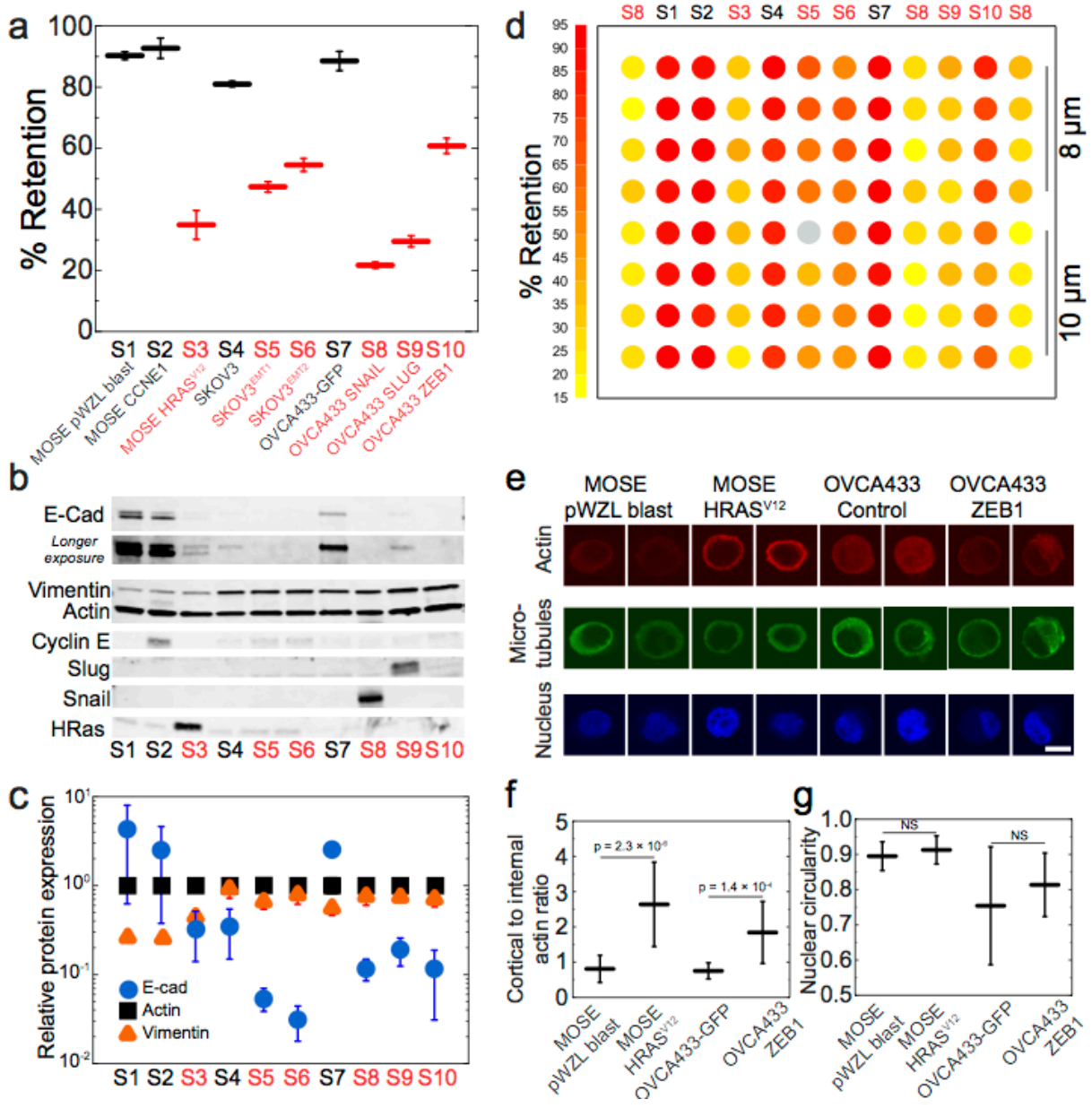

Figure 2 | **Identifying epithelial *versus* mesenchymal cells by mechanotype**. **(a)** Mouse ovarian surface epithelial (MOSE) and human ovarian cancer cells (SKOV3 and OVCA433) are modified to generate a panel of cells that includes epithelial- (black) and mesenchymal-like (red) cell types. Percentage retention of a panel of mouse and human cell lines after filtration with 10 μm pore membrane at 2.1 kPa for 50 s. Each data point represents mean ± S.D. The modified cells show reduced % retention as compared to the non-modified control: Snail: 22 ± 4%, Slug: 33 ± 4%, and Zeb1: 54 ± 5% *versus* control OVCA433-GFP: 91 ± 2%. $SKOV3^{EMT1}$: 44 ± 4% and $SKOV3^{EMT2}$: 52 ± 3% while the control SKOV3 cells: 84 ± 3%. Collectively the % retention of all epithelial-type cells is higher than cells with mesenchymal phenotype: 88 ± 5% vs. 41 ± 14%, $p = 1.8 \times 10^{-15}$. **(b)** Western blot characterization of the cell panel probing for protein biomarkers of epithelial- and mesenchymal-type cells such as E-cadherin (ECad) and vimentin. **(c)** Quantification of E-cadherin and vimentin protein levels normalized to the loading control, actin. Data points represent mean ± S.D. **(d)** Heat map shows % retention for the EMT panel for both 8 and 10 μm membranes. The 10 μm pore size shows reduced variability compared to the 8 μm pore size; therefore we conduct our screens using 10 μm membranes. **(e)** Confocal images of immunolabeled cells. Nuclei are stained with DRAQ5. Two representative images are shown for each cell type. Scale, 10 μm. **(f)** Cortical to internal actin ratio of four representative cell lines from the panel. **(g)** Nuclear circularity.

Detecting the effects of drugs on cell mechanotype. A potentially valuable application of PMF would be to identify effective anti-cancer compounds by screening cells on the basis of mechanotype. An effective chemotherapy strategy is to impair cell division by targeting cytoskeletal components that are essential for proliferation, such as microtubules[41,42]. One common drug is paclitaxel, which is used in treatment of ovarian, breast, and non-small cell lung cancers. To validate the utility of PMF to detect differences in cell deformability following drug response, we treat SKOV3 and OVCA433 cells with paclitaxel at 0.1 to 1000 nM; the IC_{50} for these cells is within this range[43]. We use a pressure of 2.1 kPa, which results in ~45 to 65% retention for the mesenchymal-type cells prior to drug treatment, ensuring a dynamic range for detecting softer or stiffer cells when multiple samples are screened in parallel. Over the range of paclitaxel concentrations, we observe that increasing doses of paclitaxel cause a significant >30% increase in retention (**Fig. 3**). Even for a physiologically relevant dose of 1 nM[43], there is a statistically significant increase in retention for mesenchymal-type cells compared to DMSO-treated control cells. In contrast, epithelial-like cells exhibit a smaller <10% increase in retention. For all measurements, we verify that cell viability remains over 94% (average viability 99%,

Supplementary Table 2). We also confirm that below 1 nM paclitaxel, there are no significant differences in cell size; at higher paclitaxel concentrations, there is a slight increase in cell-to-pore size ratio, yet the difference in % retention is typically within measurement error (**Supplementary Fig. 2**).

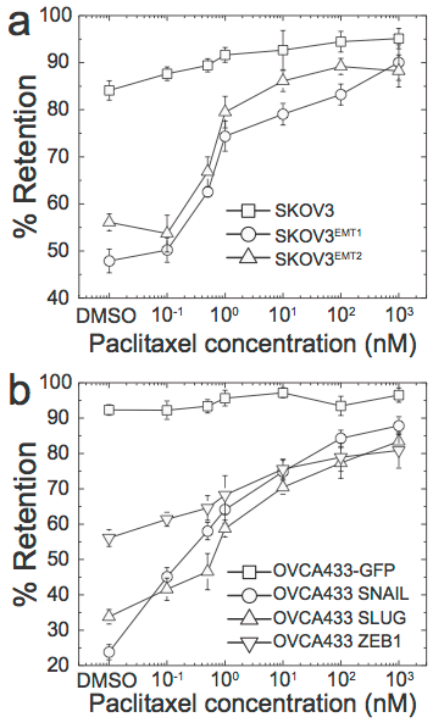

Figure 3 | Effects of paclitaxel on the mechanotype of epithelial *versus* mesenchymal-type cells. Cells are treated with paclitaxel for 24 hrs prior to filtration through a 10 μm membrane. **(a)** Percentage retention of SKOV3 control and modified cells are measured after filtration at 2.1 kPa for 50 s. **(b)** Percentage retention of OVCA433-GFP control and modified cells are measured after filtration at 2.8 kPa applied for 40 s. Compared to the DMSO-treated control cells, there is an increase in % retention of 1 nM-treated cells: 17% ± 2%, $p = 3.1 \times 10^{-3}$ for $SKOV3^{EMT1}$; 23% ± 6%, $p = 1.9 \times 10^{-5}$ for $SKOV3^{EMT2}$; 15% ± 6%, $p = 1.4 \times 10^{-2}$ for OVCA433 SNAIL; 10% ± 6%, $p = 1.2 \times 10^{-2}$ for OVCA433 SLUG; 23% ± 2%, $p = 8.9 \times 10^{-5}$ for OVCA433 ZEB1. We note that with higher applied stresses, epithelial-type cells also exhibit a similar increase in retention (**Supplementary Fig. 14**). Each data point represents mean ± S.D.

Mechanotyping cisplatin-sensitive *versus* -resistant human ovarian cancer cells. To explore EMT in a context relevant to ovarian cancer treatment, we investigate the mechanotype of drug-resistant *versus* -sensitive ovarian cancer cells. A major challenge in treating human ovarian cancer is to distinguish cells that develop resistance to common chemotherapy drugs,

such as cisplatin, which frequently result in recurrence and poor patient outcome[44,45]. If we could apply PMF to detect ovarian cancer cells that are sensitive to cisplatin (SKOV3, OVCAR5) and their drug-resistant counterparts (SKOV3-CisR, OVCAR5-CisR) using cell mechanotype as a biomarker, our assay could have potential application in clinical settings.

We generate drug resistant cells by treatment with cisplatin over 12 months[23]. These cells show similar size compared to their drug-sensitive counterparts (**Supplementary Fig. 2**). PMF reveals that both SKOV3-CisR and OVCAR5-CisR samples have lower % retention compared to the cisplatin sensitive cells (**Fig. 4a**), indicating that the drug-resistant cells are more deformable than their drug-sensitive counterparts. Since the EMT status of these cells had not previously been determined, we perform immunoblotting to verify if these softer, CisR cells also have biochemical markers that characterize mesenchymal-type cells. The SKOV3-CisR cells show reduced levels of E-Cadherin, a common feature of mesenchymal-type cells (**Fig. 4b**). While OVCAR5 cells inherently have low levels of E-Cadherin, the OVCAR5-CisR cells show a marked increase in vimentin levels; this is also a hallmark of cells with mesenchymal phenotype.

To explore the origins of the altered mechanotype in the cisplatin sensitive and resistant cells, we investigate the structure of actin, microtubules, and the nucleus by immunofluorescence and confocal imaging. While microtubules exhibit similar structure in both cell types, the cisplatin sensitive cells have a denser cortical actin network compared to CisR cells (**Fig. 4c,d**). We also observe differences in nuclear morphology: while all cells exhibit nuclei with a variety of morphologies including ovoid and kidney-shapes, the circularity index is reduced for CisR cells, reflecting that their nuclei exhibit more irregular shapes than the cisplatin sensitive cells (**Fig. 4c,e**). Altered physical properties of the nucleus may also contribute to the altered filtration behavior of the CisR cells, as the nucleus rate-limits the transit of cells through micron-scale pores[18].

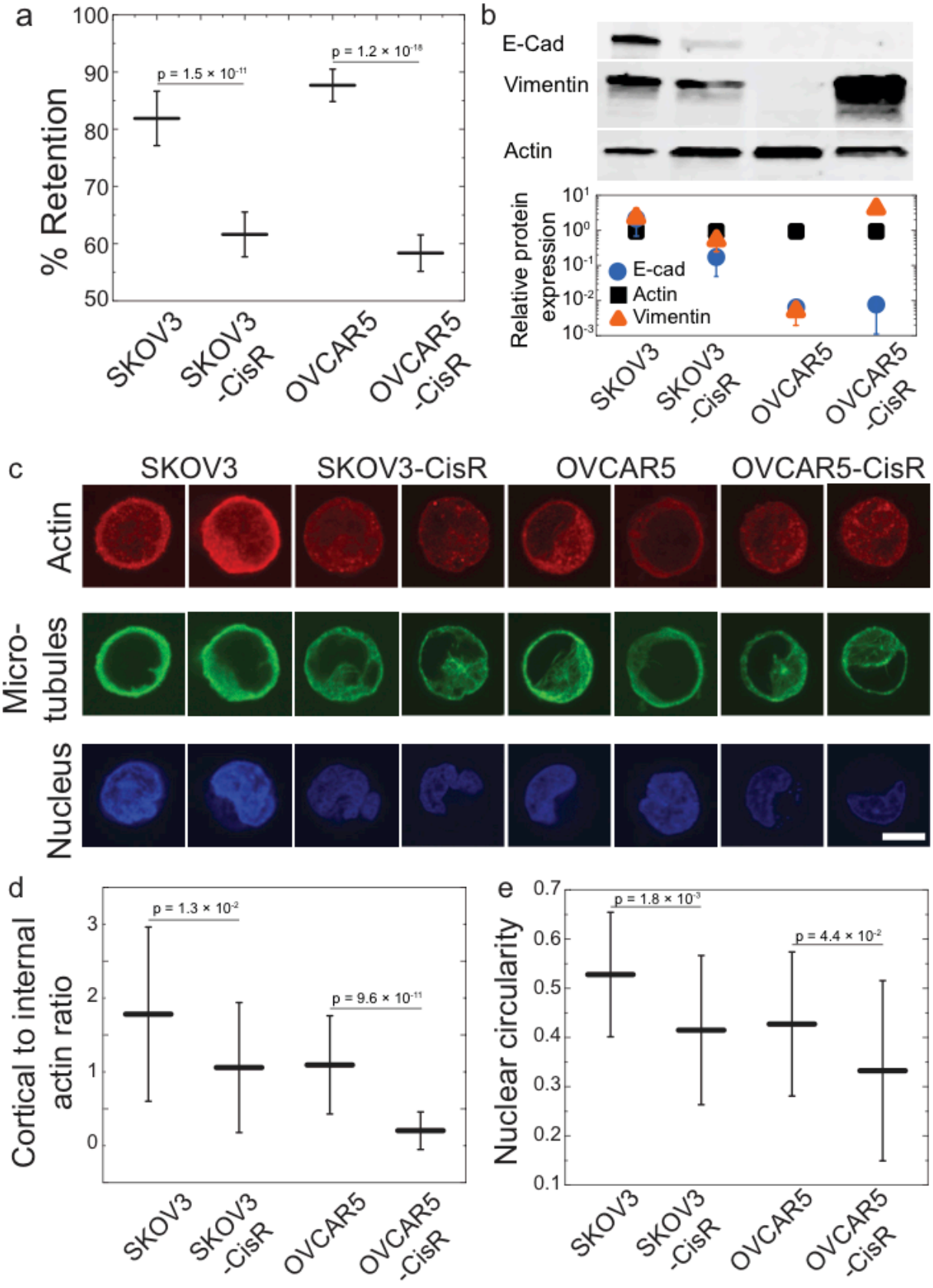
a
% Retention
p = 1.5 × 10-11
p = 1.2 × 10-18
SKOV3
SKOV3 -CisR
OVCAR5
OVCAR5 -CisR
b
E-Cad
Vimentin
Actin
Relative protein expression
E-cad
Actin
Vimentin
c
SKOV3
SKOV3-CisR
OVCAR5
OVCAR5-CisR
Actin
Micro-tubules
Nucleus
d
Cortical to internal actin ratio
p = 1.3 × 10-2
p = 9.6 × 10-11
e
Nuclear circularity
p = 1.8 × 10-3
p = 4.4 × 10-2

Figure 4 | Cisplatin-sensitive and -resistant human ovarian cancer cells show altered mechanotype. (**a**) Percentage retention of cisplatin sensitive cells, SKOV3 and OVCAR5, *versus* cisplatin resistant (CisR) cells, SKOV3-CisR and OVCAR5-CisR, after filtration with 10 μm pore membrane at 2.1 kPa for 50 s. Each data point represents mean ± S.D. (**b**) Western blot analysis and quantification of protein biomarkers for epithelial and mesenchymal-type cells, E-cadherin (ECad) and vimentin protein levels normalized to the actin loading control. Data points represent mean ± S.D. **(c)** Confocal images of immunolabeled cells. Nuclei are stained with DRAQ5. Two representative images are shown for each cell type. Scale, 10 μm. **(d)** Cortical to internal actin ratio. **(e)** Nuclear circularity.

Discussion

Here we show how PMF enables comparative measurements of cell mechanotype simultaneously across multiple cell samples. Using PMF, we observe a strong correlation between biochemical and mechanical phenotypes of cells through EMT, including when induced by acquisition of drug resistance, as well as by overexpression of specific master regulators that are implicated in EMT. We find that the mesenchymal phenotype following EMT, which is associated with cancer progression and drug resistance, results in increased deformability across the cell panel. These findings were made possible by the ability of PMF to screen a panel of cells simultaneously. Moreover, the PMF method is scalable and significantly reduces the time required to analyze individual samples of cells; parallel measurements of cell deformability are not possible using existing methods.

Our results show a marked difference in the mechanotype of epithelial *versus* mesenchymal-type cells. Studies using conventional techniques have indicated a difference in the mechanotype of these cell types[22,23,31,32]. While we observe that mesenchymal-type cells have a softer mechanotype, previous studies revealed that mesenchymal-type cells are stiffer. For example, normal murine mammary gland (NMuMG) cells that are induced through EMT by TGF-beta-1 are more resistant to deformation[31,32]. Similarly, CisR ovarian cancer cells have a higher elastic modulus compared to the drug-sensitive controls[22,23]. However, those results are obtained for cells adhered to glass substrates (E ~ 70 GPa), which tend to have well-developed actin stress

fibers and increased intracellular tension[23]. By contrast, PMF probes cells in a suspended state, where CisR cells have a lower density of cortical actin compared to the cisplatin sensitive cells. The mode of deformation between PMF and other techniques such as AFM is also distinct: PMF measures the ability of whole cells to deform through micron-scale pores that are ~40-70% of their size, whereas AFM indents cells over nm to sub-μm length scales.

While PMF robustly identifies epithelial- *versus* mesenchymal-type cells, the molecular origins of cell mechanotype remain to be fully understood. Dramatic alterations in cytoskeletal architecture occur with EMT. For example, cortical actin reorganizes to form stress fibers and structures that enable directional motility[31]; these modified actin structures can contribute to altered cancer cell mechanotype[4,46]. In the mesenchymal-like cisplatin resistant *versus* sensitive cells, the observed decrease in cortical actin provides a plausible mechanism for their softer mechanotype: levels of cortical actin regulate % retention, as observed in HL-60 and OVCA433-GFP cells treated with cytochalasin D or colchicine to induce either a decrease or increase in F-actin (**Supplementary Fig. 3**). However, in other types of mesenchymal-like cells, we observe an *increase* in cortical actin compared to their epithelial counterparts; this typically causes an increase in cell elastic modulus, and thus cannot fully explain the observed softer mechanotype of all mesenchymal-type cells. The CisR cells also exhibit irregular nuclear structure. Since we cannot dissect the individual contributions of cortical actin and the nucleus, altered % retention could also be caused by altered structure of the cell nucleus, which is a major contributor to cell mechanotype and the ability of cells to transit and migrate through narrow pores[18,47]. Numerous other mechanisms could impact cell mechanotype. For example, several actin-associated proteins are downregulated by Snail, such as CAPG capping protein and gelsolin[36]. Rho-mediated actin remodeling[22] and nuclear lamins[18] can also alter cell mechanical properties. Other factors such as myosin II regulate contractility and motility[48]; the transcription factors YAP1 and TAZ are also implicated in cell

mechanotype[49]. PMF should enable further studies to elucidate the molecular mechanisms of mechanotype, for example by screening cells treated with siRNA or CRISPR libraries.

Our label-free mechanotyping assay also has potential for clinical applications, for example, to screen established cell lines and patient samples for prognosis and drug screening. This robust and high throughput method allows rapid analysis of ~10^5-10^6 cells per sample, which is important due to the cellular heterogeneity within a tumor. While we have investigated here cell samples with relatively uniform cell-to-pore size ratios, PMF screening using a range of pore sizes could enable screening clinical samples that may contain mixed populations of cells with different size distributions. PMF could thus complement and enhance existing methods for evaluating cancer cells and their response to drugs. Considering that key steps in metastasis require large deformations of cells, such as intravasation and extravasation, this simple assay could provide physiologically relevant insights into the behavior of cancer cells. More broadly, PMF could be valuable for identifying compounds that are relevant to other disorders that are characterized by altered cell mechanotype, from malaria to diabetes.

Methods

Cell culture. Human promyelocytic leukemia (HL-60) cells are cultured (5% CO_2, 37°C) in RPMI-1640 media with L-Glutamine (Invitrogen) supplemented with 10% fetal bovine serum (FBS) and 1% penicillin-streptomycin (PenStrep, Gemini BioProducts, Calabasas, USA). To avoid spontaneous differentiation that can arise due to increased HL-60 cell density, we maintain these cells at a density below ~8×10^5 cells/ml. Neutrophil-type cells (dHL-60) are generated by treating HL-60 cells with 5 μM all-trans retinoic acid (ATRA) (1 mM stock in ethanol, Sigma-Aldrich) for 5 days. Human ovarian cancer (SKOV3 and OVCA433) cells are cultured in DMEM (+L-Glutamine, +Glucose, +Sodium Pyruvate) supplemented with 10% FBS, 1% Anti-anti (Gibco), and 2.5 μg/ml Plasmocin Prophylactic (Invivogen). For OVCA433 cells and derivatives (Snail, Slug, Zeb1) as

well as MOSE pWZL blast, we use the same media with the addition of blasticidin S HCl (5 µg/ml, Corning Cellgro); for the MOSE HRAS^{V12} cells, we add hygromycin (4 µl/ml, Corning Cellgro); and for the MOSE CCNE1 cells, puromycin (5 µg/ml, Corning Cellgro). To culture the pairs of cisplatin-sensitive and -resistant cells, SKOV3/SKOV3-CisR and OVCAR5/OVCAR5-CisR, we use DMEM with 10% FBS, 1% Penicilin-Streptomycin, and 10 µM cisplatin (Sigma-Aldrich) for the resistant cells. Adherent cells are harvested by washing with 1× Phosphate-Buffered Saline (PBS, DNase-, RNase- & Protease- free, Mediatech, Manassas, USA), treating with trypsin, and resuspending in fresh medium. To minimize clusters of cells, cell suspensions are passed through a 35 µm filter (BD Falcon) prior to each measurement. The identity of each cell line was confirmed by short tandem repeats (STR) profiling (Laragen Inc).

EMT Transformation. To generate EMT gene expression clones, *SNAI1*, *SNAI2*, and *ZEB1* cDNA (Open Biosystems) are individually inserted into the pLenti6.3/V5-DEST vector (Invitrogen; *ZEB1* and *SNAI2*) or pLenti4/V5-DEST vector (Invitrogen; *SNAI1*) by the Gateway cloning system (Invitrogen). OVCA433 cells are transduced with lentiviral expression plasmids harboring *SNAI1*, *SNAI2*, and *ZEB1* or GFP (control) and selected with 5 µg/mL blasticidin (InvivoGen) for 6 d prior to use. SKOV3^{EMT} cells are established by chronic exposure to a combination of 0.2 µM PD0332991 and 0.2 µM SNS032 for over 12 months (Taylor-Harding et al 2014, Submitted). SKOV3-CisR and OVCAR5-CisR cells are generated by culturing with 10 µM cisplatin over 12 months[23].

Drug treatment. A stock solution of paclitaxel (25-950-CQC, Corning Cellgro) is prepared in DMSO to 1 mM. Cells are treated with the desired concentration of drug for 24 hrs prior to measurements.

Parallel microfiltration. The PMF device is assembled using polycarbonate membranes (Isopore, Millipore) of 5, 8, and/or 10 µm pore diameter. Wells are loaded with 1% w/w bovine

serum albumin (BSA) solution (Fisher) for 1 hr at 37°C, and then emptied and air dried at least 1 hr before each experiment. Cell suspension at a concentration of 0.5 □ 10^6 cells/ml (ovarian cancer cells) and 1.0 □ 10^6 cells/ml (HL-60 cells) is loaded into each well. Well-defined air pressures from 0.7 to 7 kPa are applied using a custom-built manometer (**Supplementary Fig. 10)** and monitored using a pressure gauge (Noshok Inc., Berea, OH, USA). We determine % retention by collecting the sample suspension remaining in the top well and measuring the mass using a precision balance (Northeast Scale Inc., Hookset, NH, USA). To measure cell number and size distributions, we use an automated cell counter (TC20, BioRad). We also verify that cells in suspension do not cluster over our experimental time scale of ~15 minutes **(Supplementary Fig. 11).**

Immunofluorescence staining and image analysis. Cell suspensions are placed in chambers of Millicell EZ slides (Millipore) for ~1.5 hours at 37°C before fixation with paraformaldehyde (4% in PBS) for 20 minutes at room temperature. Cells are then permeabilized with 0.2 % Triton X-100 for 10 minutes and blocked with 3% BSA in PBS for 2 hours. To stain cytoskeletal components, primary and secondary antibodies (Sigma-Aldrich) are sequentially applied to cells for 1 hour: Anti-Actin (CAT#: A2066); Anti-Rabbit IgG F(ab′)2 fragment - Atto 488 (CAT#: 36098; λ_{ex}-500 nm; λ_{em}-522 nm); Monoclonal Anti-α-Tubulin (CAT#: T5168); Anti-Mouse IgG−Atto 550 (CAT#: 43394; λ_{ex}-550 nm; λ_{em}-576 nm). To label the cell nucleus, we use the DNA-intercalating dye, DRAQ5 (Fisher Scientific). Imaging is performed using a confocal microscope (LSM 5 EXCITER, Laser Scanning Microscope, Zeiss) equipped with a 63× objective (63x/1.2 W Korr UV-VIS-IR, C-APOCHROMAT, Zeiss). To measure actin signal, an Argon laser (488 nm) and BP505-530 filter are used; to measure microtubule signal, a Helium-Neon laser (543 nm) and BP560-615 filter are used; to measure nuclear signal, a Helium-Neon laser (633 nm) and LP650 filter are used. Midplane confocal images are analyzed using ImageJ. For analysis of cortical-to-internal actin ratio, we measure the integrated signal of immunostained actin in the whole cell and an

internal region that is 1 μm from the boundary of the cell; actin intensity in the cortical region is determined by subtracting the intensity of the internal region from the total actin intensity in the whole cell. Circularity is calculated as $4\pi A/P^2$, where A and P are the area and perimeter of individual nuclei; for a perfect circle, the circularity value is one.

Western blots. Whole cell protein extracts are separated by SDS-PAGE and transferred onto PVDF membranes using semi-dry transfer (BioRad). After incubation with 5% milk in PBST (10 nM Tris, pH 7.4, 150 nM NaCl, 0.1% Tween 20) for one hour, the membrane is probed with antibodies against proteins of interest including E-cadherin (CAT#: 610181, BD Biosciences), vimentin (CAT#: MS-129-PO, Thermo Scientific), and actin (CAT#: MA5-15739, Thermo Scientific) as a loading control. Antibodies are incubated at 4 °C for 12 h followed by three washes of 10 minutes each in PBST. Proteins are then detected with fluorescent-conjugated antibodies, Goat anti-Mouse IgG IRDye 680LT (CAT#: 827-11080) and Goat anti-Rabbit IgG IRDye 680RD (CAT#: 926-68170). Immunoblots are visualized using a Li-Cor Odyssey Infra-red imaging system.

Soft agar assay. Anchorage-independent growth of MOSE epithelial and mesenchymal-type cells is tested by colony formation in soft agar. We plate 1-ml of DMEM (+L-Glutamine, +Glucose, +Sodium Pyruvate) supplemented with 10% FBS and 1% Anti-anti (Gibco) containing 1.2% agar into each well of a 6-well plate; ~10^4 cells are then suspended in 1% agarose containing culture medium. After 2-3 weeks, colonies are stained with 0.5 mg/ml iodonitrotetrazolium chloride and the number of colonies is determined across triplicate wells for each cell line.

Statistical methods. We perform PMF using 4 wells for a single sample in parallel multiple sample measurements. All data is obtained from at least 3 independent measurements and is expressed as mean ± S.D. We use the Student's t-test method to analyze the results and to obtain p-values.

Numerical modeling. The flow rate is proportional to the number of available pores, $Q(t)=qn(t)$, where q is the flow rate through a single pore and $n(t)$ is the number of open pores at time, t. While q is set by the applied pressure and pore dimensions and thus remains constant throughout a single experiment, the total flow rate, $Q(t)$, changes over time as it is determined by the number of available pores. We model the filtration process using successive iterations over time: in a given time interval, τ, each available pore can be encountered by a single cell. To model filtration for a given set of conditions, we determine τ by $(qc)^{-1}$, which is the time for the fluid volume per cell, $1/c$, to pass through a single pore. Here, c is the density of the cell suspension, which remains relatively constant before and after the filtration measurement (**Supplementary Fig. 12**). In a given time window, Δt, the total number of iterations is $J=\Delta t/\tau$. We use the least squares method to fit our experimental results, where the only adjustable parameter is χ, the fraction of cells that occlude the filtration pores. Other parameters in the model are known: the initial number of pores in the filtration area is obtained by measuring the membrane pore density and total filtration area in a single well (**Supplementary Fig. 13)**; the medium flow rate through single pores is calculated using Poiseuille's law and is in agreement with the experimentally measured values. By considering the fraction of cells that occlude the pores within each time interval, we can recapitulate the decreasing permeability of the membrane: as filtration proceeds, an increasing volume of cell suspension and thus, number of cells, arrive at the pores; the fraction of occluded pores increases; the total flow rate subsequently decreases; and progressively fewer cells are brought to the membrane. A similar time-dependent increase in fluidic resistance is considered in crossflow membrane filtration of colloidal suspensions[50,51].

Supplementary notes

1. Parallel filtration device and measurement. To obtain a pressure-tight seal between the pressure chamber and the top plate, we place a silicone seal (McMaster Carr, USA) in between the top plate and the pressure chamber. Two aluminum plates affixed to the top and bottom of

the ‘sandwich’ are used to clamp the entire setup together (**Fig. 1**). To facilitate flow of cell suspensions through the porous membrane, we drill 1 mm holes into the bottom of each well of the bottom plate (**Supplementary Fig. 15**). Cross-sample contamination and leakage across individual sample wells are prevented by sealing each well with an O-ring; a silicone mat punctuated with holes that correspond to the array of wells can alternatively be used to isolate the contents of individual wells.

2. Protocol for PMF assay. (1) Place silicone mat on bottom plate, or O-rings in each well of the bottom plate (**Fig. 1**). (2) Position porous membranes on top of the bottom plate and sealant. (3) Place the top plate on the membrane/O-rings, using the steel bolts at the edge of the plates to guide the alignment of the top and bottom wells (**Supplementary Fig. 15**); thereafter clamp both plates using the edge steel bolts. (4) To minimize cell-device surface interactions, pretreat the device by placing 800 µl of fresh bovine serum albumin (BSA) solution (1% w/w in de-ionized water, filtered through 0.2 µm Surfactant-Free Cellulose Acetate (SFCA) membrane filter unit (Nalgene, Thermo Scientific) in each top well before use. Incubate the setup at 37^{o}C for one hour. Thereafter, remove the BSA solution from the wells and air dry the device. (5) Place the parallel filtration device in a shallow ~ 7 mm water bath; this prevents sample drainage due to gravity. (6) Measure the density of the cell suspension using a particle/cell analyzer (e.g. BioRad TC20 Cell Counter or Coulter Counter) and then place 750 µl of cell suspension with a concentration of 10^6 cells/ml into each well. (7) Position the pressure chamber and tighten the entire device together to achieve an airtight seal. (8) Apply a well-defined pressure for 20 – 50 s. (9) Remove the pressure chamber and collect the samples retained in the top wells for measurement of retained volume and/or cell number.

3. Pore size dependence of filtration. To determine the pore size dependence of filtration, we use three types of polycarbonate membranes (Isopore, Millipore, USA) with pore sizes of 5, 8,

and 10 μm. Since membrane porosity is essential for filtration, we characterize the membranes using confocal microscopy, taking advantage of the zero-reflection of the hollow area of pores. We observe that some pores are connected together, and define these as pore clusters (**Supplementary Fig. 14**). To obtain the porosity for each membrane, we perform quantitative image analysis using ImageJ to determine the ratio of pore or cluster area to total membrane area, as shown in **Supplementary Table 3**.

Supplementary Figures

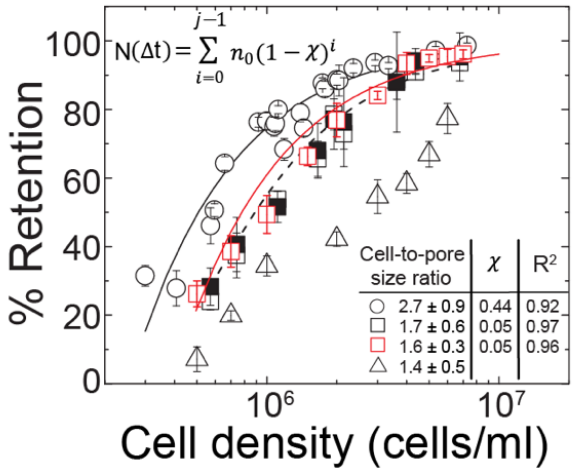

Supplementary Figure 1. Quantification of cell filtration by % retention. Filled squares represent cell number % retention; open symbols show fluid mass % retention; both parameters can be used equivalently to quantify filtration.

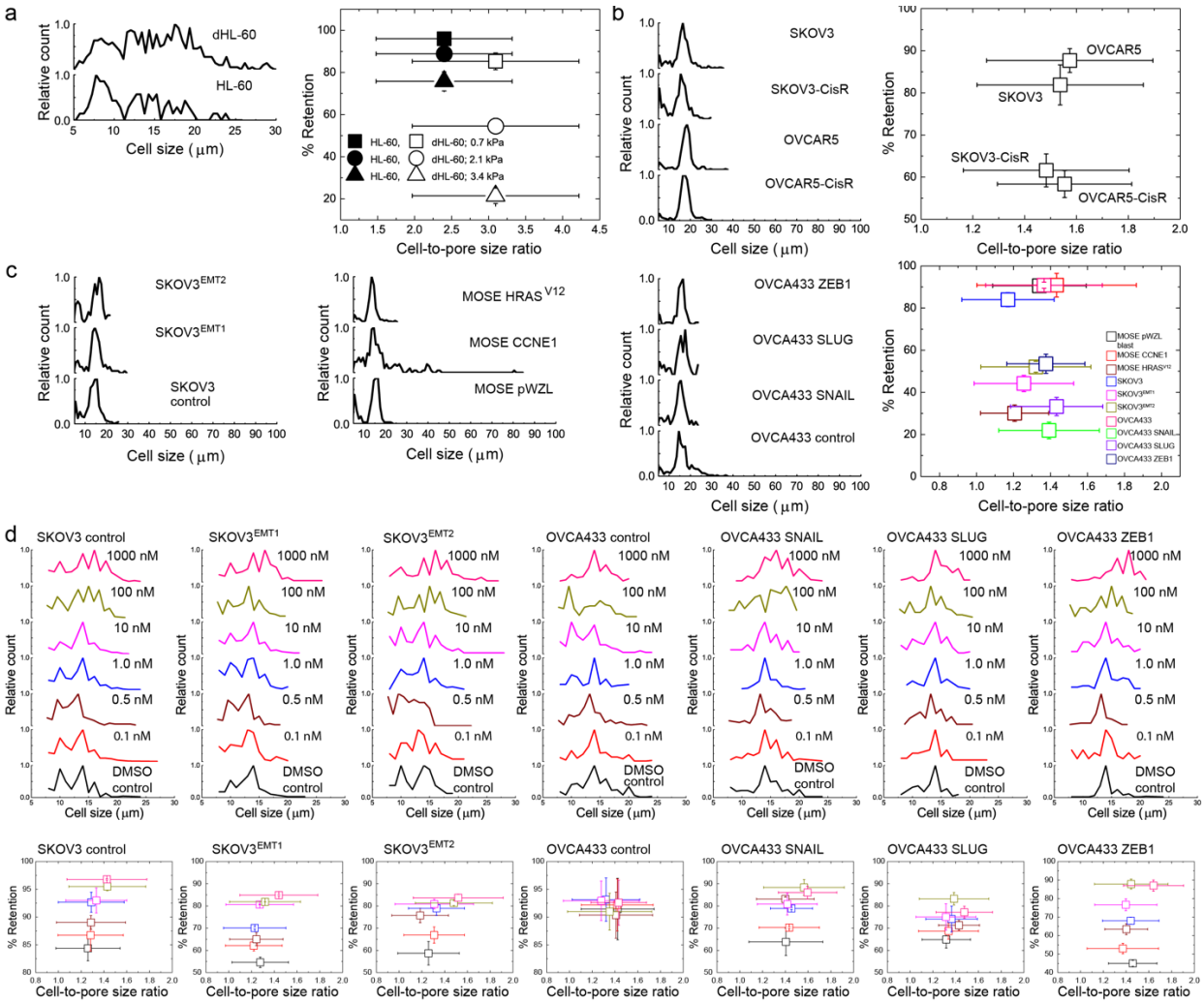

Supplementary Figure 2. Size distribution and filtration of cells. Percentage retention *versus* cell-to-pore size ratios for: **(a)** HL-60 and dHL-60 cells; **(b)** cisplatin-sensitive (CisS) and cisplatin-resistant (CisR) cells; **(c)** epithelial and mesenchymal-type cells in the cell panel; and **(d)** cells treated with paclitaxel and carrier DMSO control.

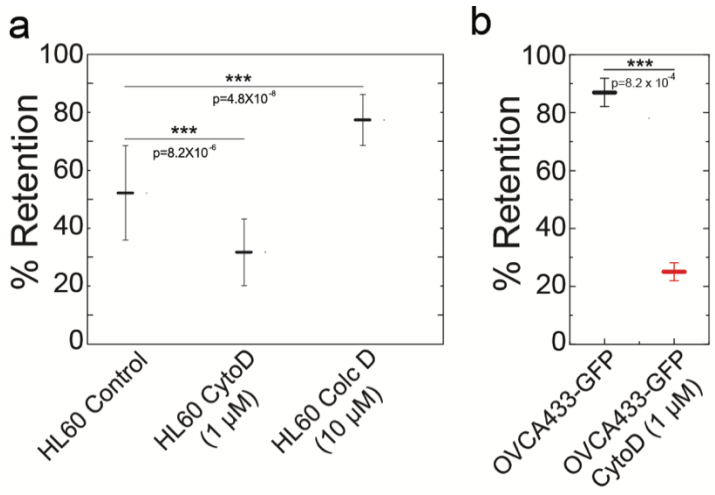

Supplementary Figure 3. Effect of F-actin on filtration. (a) HL-60 cells treated with cytochalasin D (Cyto D) or colchicine (Colc) to induce either a decrease or increase in F-actin. Measurement conditions: 8 μm pore membrane; 0.7 kPa applied for 20 s. (b) OVCA433-GFP cells treated with Cyto D. Mean (Horizontal line) ± S.D. (vertical line). P-values reflect statistical significance determined by Student's t-test.

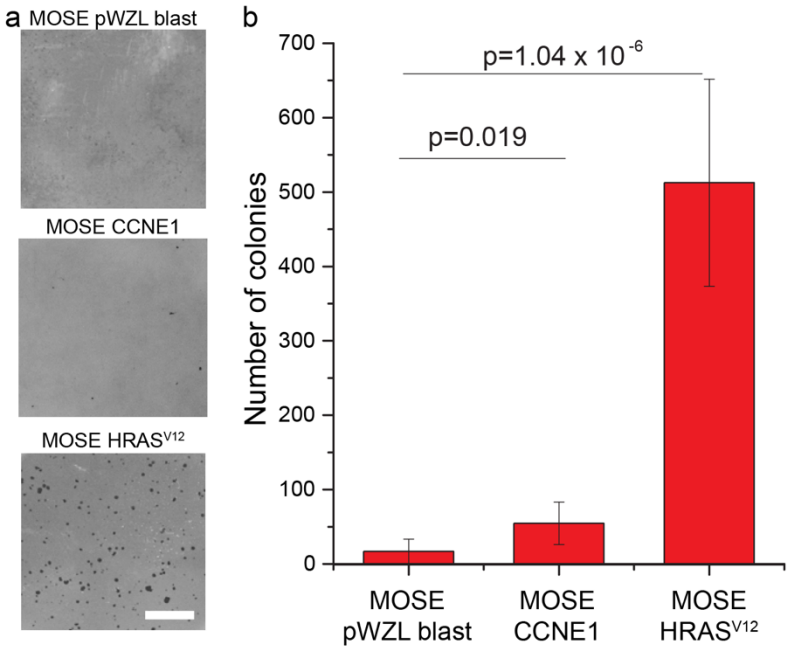

Supplementary Figure 4. Mesenchymal-type cells form colonies in soft agar assay. MOSE control (pWZL blast) cells, MOSE CCNE1, and MOSE HRASV^{12} cells are embedded in soft agar. **(a)** Images of cell colonies labeled with 0.5 mg/ml iodonitrotetrazolium chloride after 21 days. Brightness and contrast of the grayscale images is adjusted (to 122 brightness; 40 contrast) for visualization of MOSE pWZL blast and MOSE HRASV^{12} samples. Scale, 5 mm. **(b)** Quantitative

analysis of colony number reveals that MOSE HRAS^{V12} cells form a greater number of colonies compared to the CCNE1-modified and non-modified control cells. Bar graphs show mean values obtained over 2 independent experiments; vertical lines denote ± S.D.

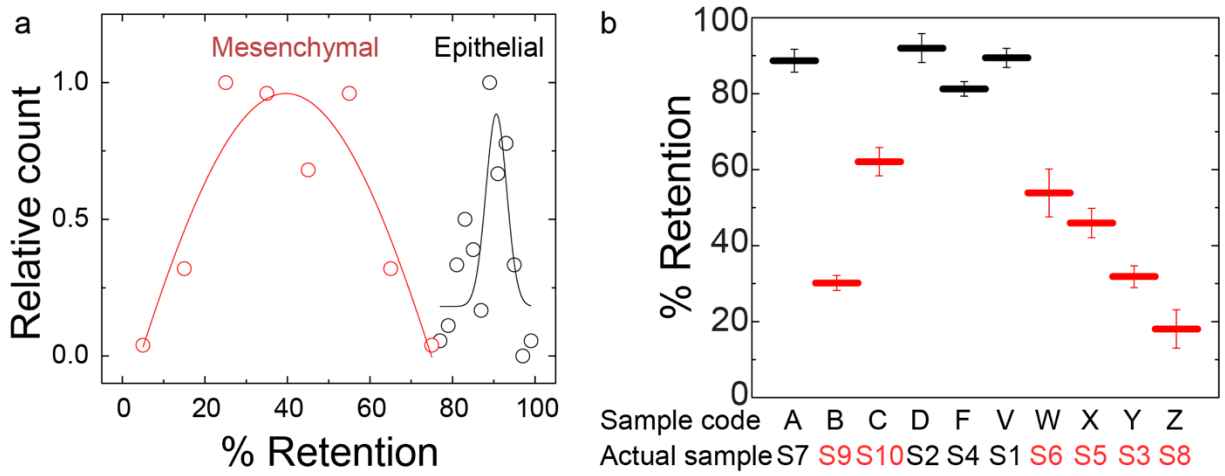

Supplementary Figure 5. Predicting epithelial and mesenchymal-type cells across the EMT cell panel. (a) Probability distributions of % retention for cells across the EMT cell panel. Raw data is obtained from panel reference measurements, as shown in Fig. 2a, and fitting is performed using a single peak Gaussian function. Peak center positions are 39.6 ± 46.1 for mesenchymal cells and 90.6 ± 2.5 for epithelial cells. **(b)** Blind mechanotyping assay performed with the same panel of cell lines using the same measurement conditions as in Fig**. 2a.**

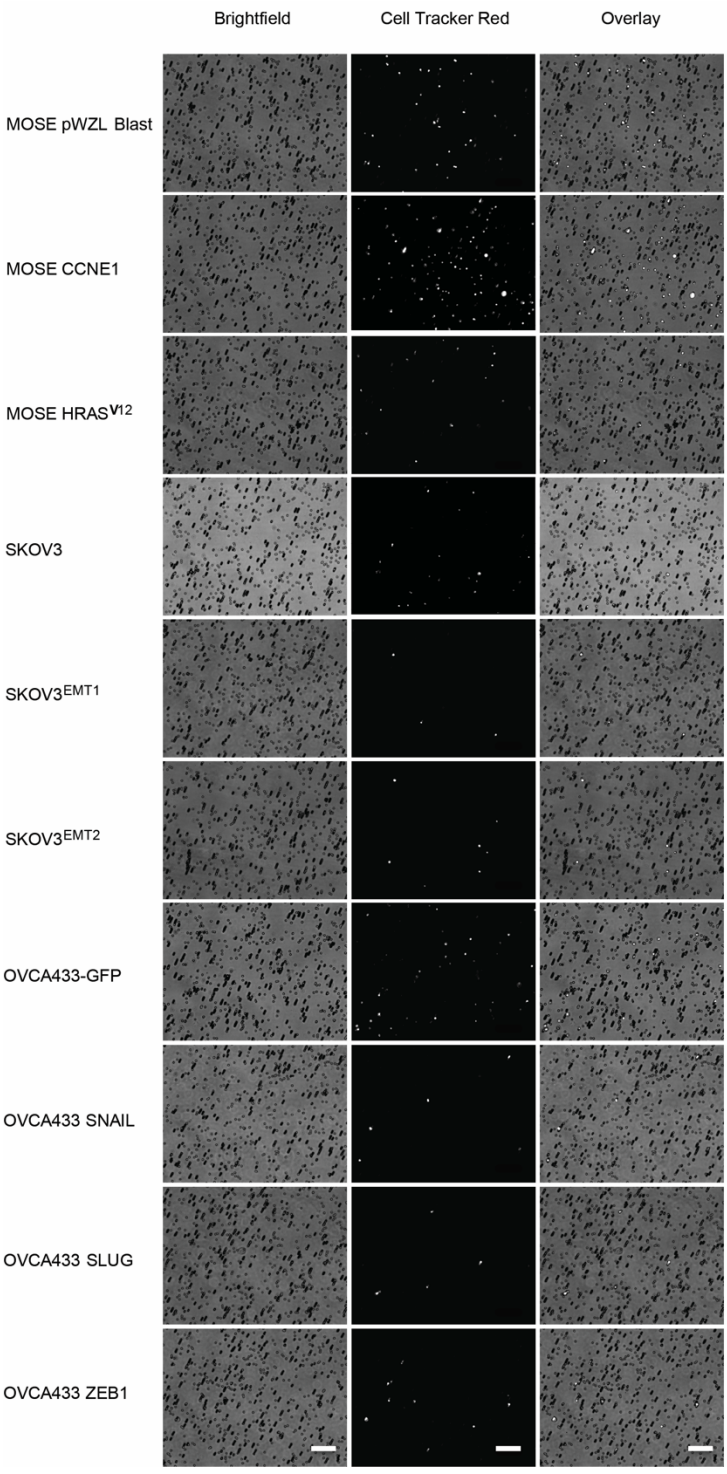

Supplementary Figure 6. Images of membranes after filtration. Fluorescence images reveal cells that are labeled with Cell Tracker dye. Percentage of pores that are occluded by single cells/ cell clusters that are larger than 18 μm are displayed in the right column. Scale, 100 μm.

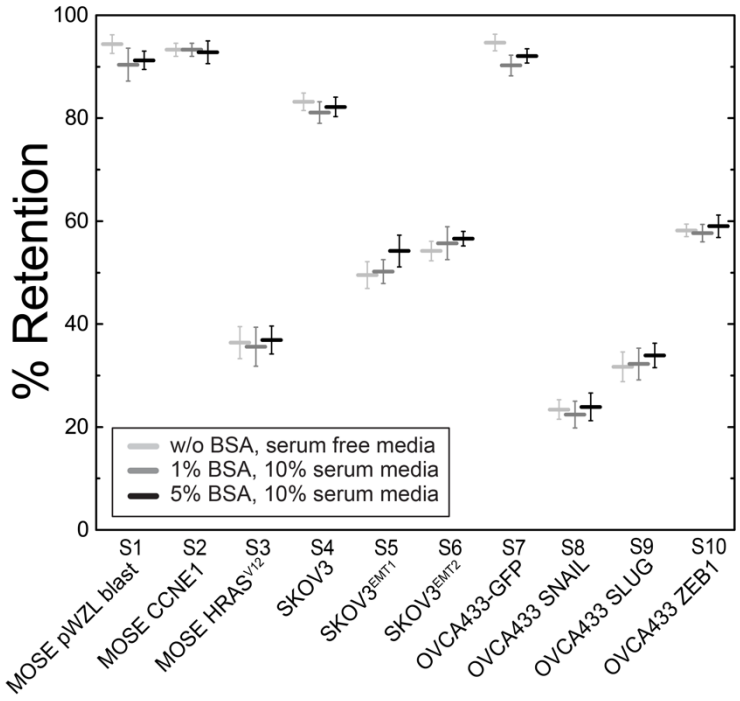

Supplementary Figure 7. Effects of BSA in % retention. Filtration of the panel of ovarian cancer cells is performed with varying concentrations of bovine serum albumin (BSA).

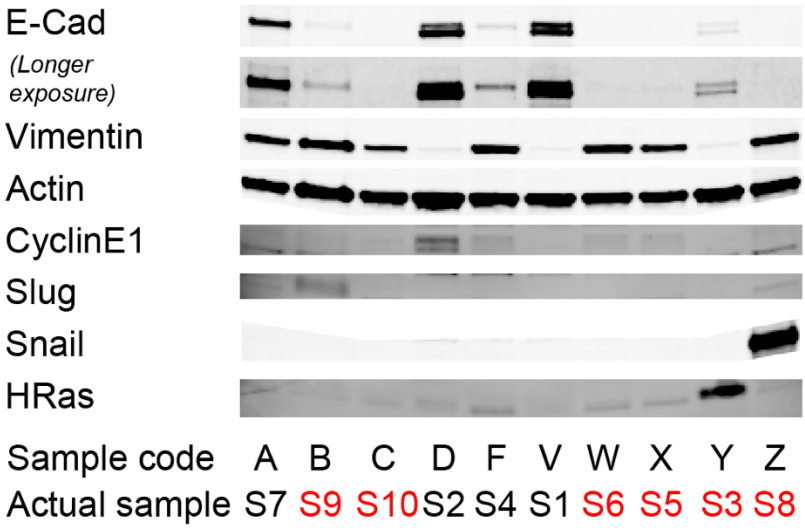

Supplementary Figure 8. Western blot confirmation of epithelial and mesenchymal-type samples run in the blind assay. Black denotes epithelial-type cell samples, while samples of mesenchymal-type cells are shown in red.

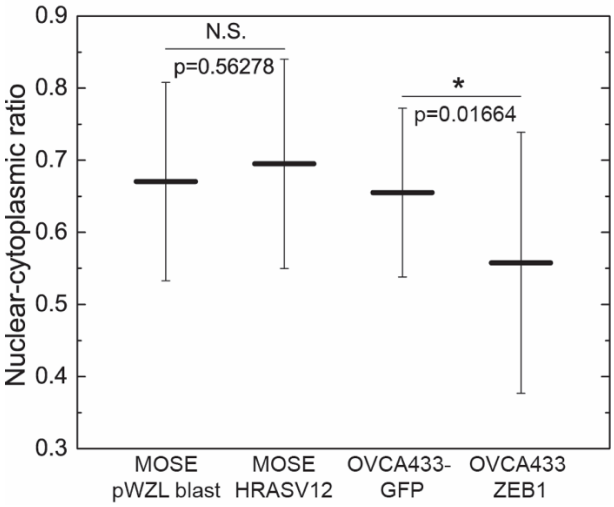

Supplementary Figure 9. Nuclear-to-cytoplasmic ratio of representative epithelial and mesenchymal-type cell lines.

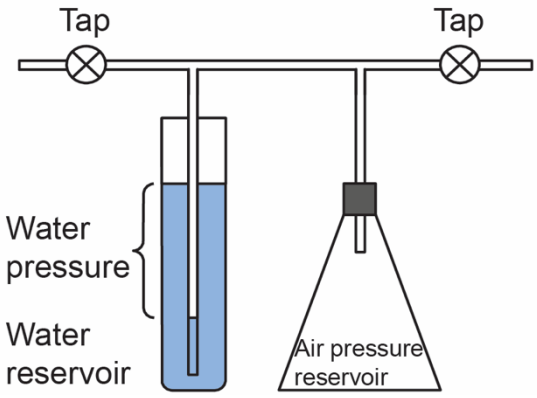

Supplementary Figure 10. Schematic illustration of a manometer. To build desired pressure (0-7 kPa) in the air pressure reservoir: close right tap, open left tap, blow in air from the air source (for example, manometer), and then close left tap. The pressure is indicated as the water pressure height. After a well-defined pressure is established, the right tap is opened to introduce air pressure to the pressure chamber of the parallel microfiltration platform.

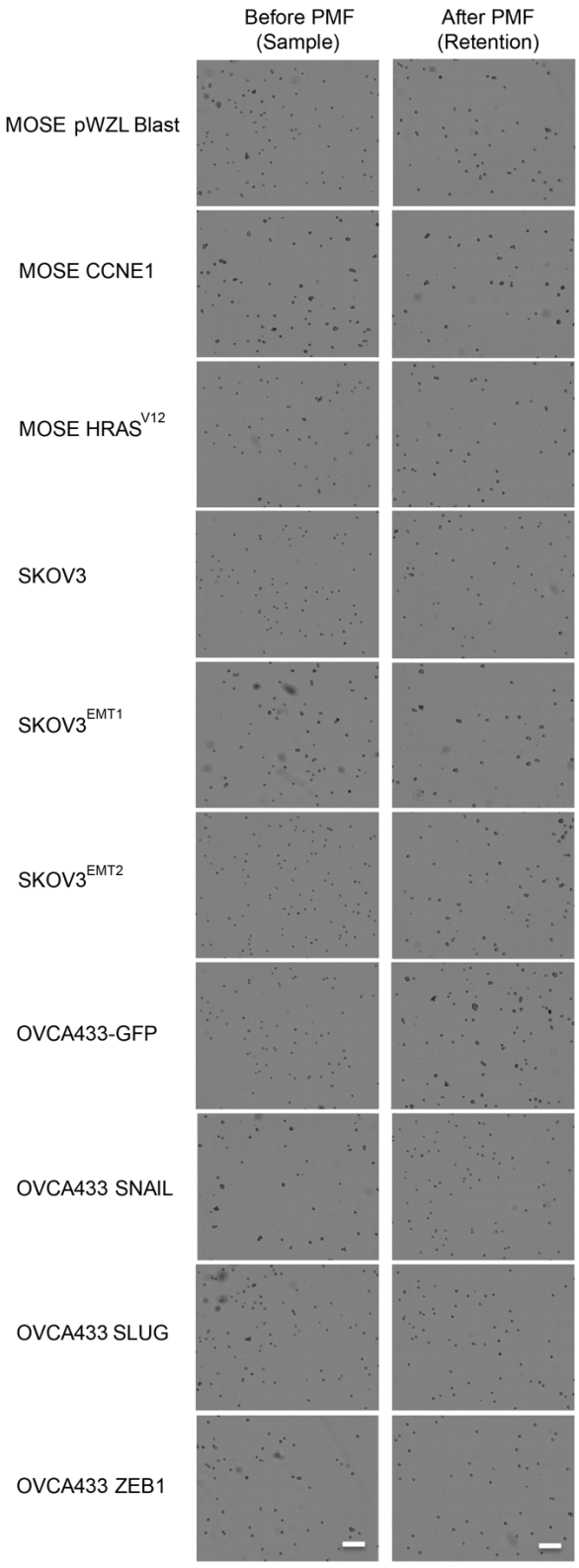

Supplementary Figure 11. Images of cell suspensions before and after PMF. Scale, 100 μm.

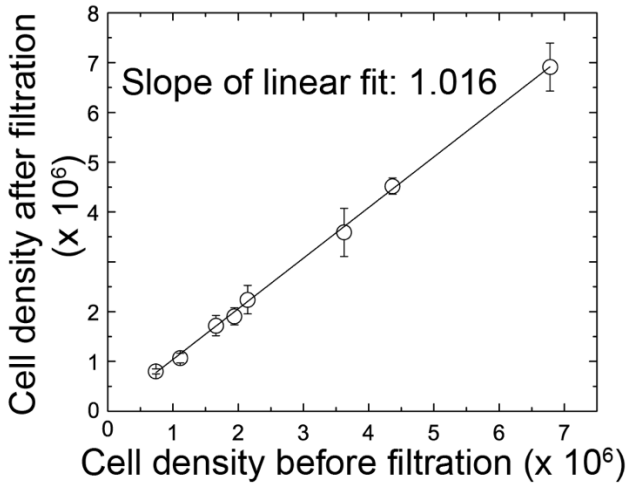

Supplementary Figure 12. Cell density before and after filtration. HL-60 cells are filtered through 8 μm pore membranes at 0.7 kPa for 20 s. After filtration, the cell density is measured from samples retained in top wells. Each data point represents mean ± S.D. Solid line represents linear fit to the data.

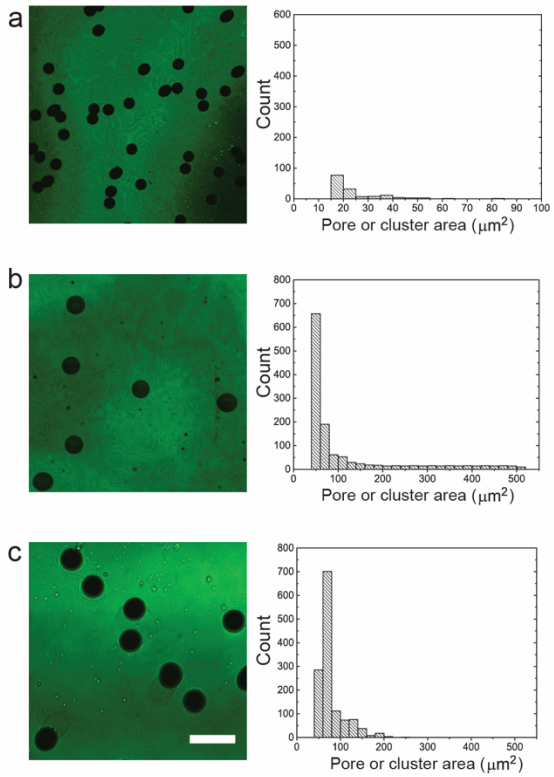

Supplementary Figure 13. Characterization of the porous membranes. (**a**-**c**) Representative images of porous membranes with 5, 8, and 10 μm pores. For each membrane, five confocal images are analyzed using ImageJ to obtain the pore (/cluster) histograms. We define clusters as any porous region that has an area greater than 1.5 pores. Further quantification of membrane porosity is provided in **Supplementary Table 3.** Scale bar, 20 μm.

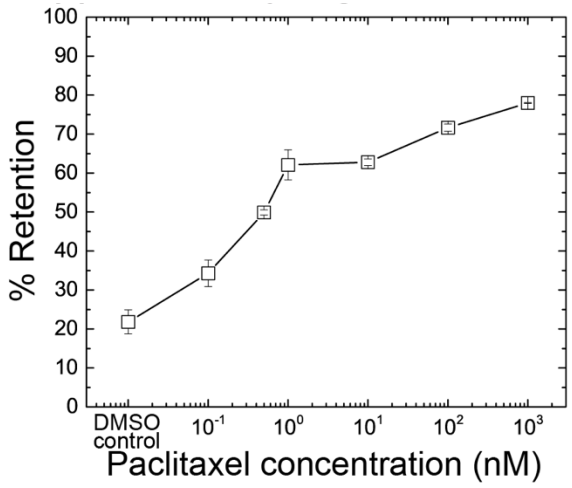

Supplementary Figure 14. Effects of paclitaxel on the filtration behavior of epithelial-like cells. SKOV3 cells are drug-treated 24 hrs prior to being filtered through 10 μm pore membranes at 2.8 kPa for 50 s. Each data point represents mean ± S.D.

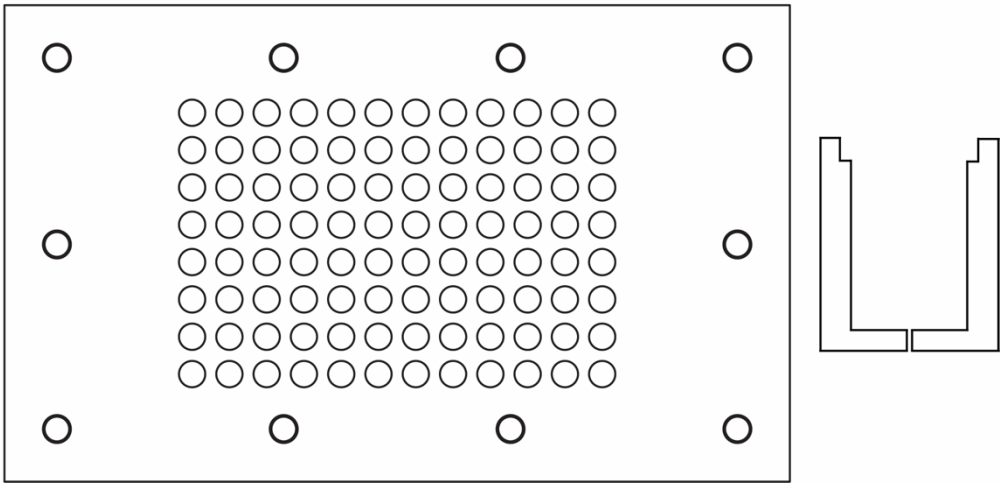

Supplementary Figure 15. Schematic illustration showing design of the 96-well plate. Left: top view of the 96-well plate. Thick circles around the perimeter of the plate represent holes for PMF assembly using steel bolts. Thin circles represent loading wells that each has a diameter of 0.64 cm (¼″) and depth of 2.54 cm (1″). Right: side view of a single well of the bottom plate. The bevelled structure at the top of the well is designed to hold an O-ring. Alternatively, a PDMS sealing mat can be used to achieve an air-tight seal. The bottom 1 mm hole facilitates filtration. Plates are machined out of Perspex (poly(methyl methacrylate) or PMMA). Drawing is not to scale.

Supplementary Tables

Supplementary Table 1. Investigating cell-surface interactions in % retention. Quantification of the number of cells recovered from wells after a filtration experimentation of ~15 min. Cell suspensions were then collected and cell densities were measured. Observed error for cell density measurements is ± 4 x 10^4.

Sample	Cell density of sample before PMF	Cell density of retained fluid after PMF
MOSE pWZL Blast	4.6 x 10^5	4.0 x 10^5
MOSE CCNE1	6.0 x 10^5	5.9 x 10^5
MOSE HRAS^{v12}	4.2 x 10^5	4.2 x 10^5
SKOV3	5.6 x 10^5	5.3 x 10^5
SKOV3^{EMT1}	5.9 x 10^5	5.4 x 10^5
SKOV3^{EMT2}	5.7 x 10^5	5.6 x 10^5
OVCA433-GFP	5.1 x 10^5	5.0 x 10^5
OVCA433 SNAIL	5.2 x 10^5	5.0 x 10^5
OVCA433 SLUG	4.7 x 10^5	4.2 x 10^5
OVCA433 ZEB1	5.1 x 10^5	5.2 x 10^5

Supplementary Table 2. Effect of paclitaxel (TAX) treatment on cell viability. Observed error for cell viability measurements is ± 2%.

Sample/ Conditions	SKOV3	SKOV3^{EMT1}	SKOV3^{EMT2}	OVCA433-GFP	OVCA433 SNAIL	OVCA433 SLUG	OVCA433 ZEB1
No treatment	98%	98%	100%	98%	99%	99%	97%
0.1% DMSO (control)	98%	98%	96%	95%	97%	97%	96%
0.1 nM TAX	98%	98%	98%	94%	98%	95%	98%
0.5 nM TAX	99%	99%	99%	94%	99%	99%	99%
1 nM TAX	96%	96%	98%	95%	99%	99%	96%
10 nM TAX	97%	96%	96%	95%	98%	98%	98%
100 nM TAX	98%	96%	96%	96%	96%	99%	98%
1000 nM TAX	96%	98%	95%	95%	98%	100%	97%

Supplementary Table 3. Characterization of membrane porosity.

Membrane	Total porosity (%) of single pores	Total porosity (%) of pore clusters	Total porosity (%)
5 μm	6.8 ± 0.7	2.5 ± 1.4	9.3 ± 2.0
8 μm	4.0 ± 0.3	0.7 ± 0.1	4.8 ± 0.4
10 μm	6.0 ± 0.3	1.4 ± 0.2	7.3 ± 0.4

References

1 Fletcher, D. A. & Mullins, D. Cell mechanics and the cytoskeleton. *Nature* **463**, 485-492 (2010).

2 Suresh, S. Biomechanics and biophysics of cancer cells. *Acta Biomater* **3**, 413-438 (2007).

3 Swaminathan, V. *et al.* Mechanical stiffness grades metastatic potential in patient tumor cells and in cancer cell lines. *Cancer Res* **71**, 5075-5080 (2012).

4 Xu, W. *et al.* Cell Stiffness Is a Biomarker of the Metastatic Potential of Ovarian Cancer Cells. *PLoS One* **7**, e46609 (2012).

5 Plodinec, M. *et al.* The nanomechanical signature of breast cancer. *Nat Nanotechnol* **7**, 757-765 (2012).

6 Cross, S. E., Jin, Y. S., Rao, J. & Gimzewski, J. K. Nanomechanical analysis of cells from cancer patients. *Nat Nanotechnol* **2**, 780-783 (2007).

7 Tse, H. T. *et al.* Quantitative diagnosis of malignant pleural effusions by single-cell mechanophenotyping. *Sci Transl Med* **5**, 212ra163 (2013).

8 Lam, W. A., Rosenbluth, M. J. & Fletcher, D. A. Chemotherapy exposure increases leukemia cell stiffness. *Blood* **109**, 3505-3508 (2007).

9 Hochmuth, R. M. & Needham, D. The Viscosity of Neutrophils and Their Transit Times through Small Pores. *Biorheology* **27**, 817-828 (1990).

10 Chien, S. & Sung, K. L. P. Effect of Colchicine on Viscoelastic Properties of Neutrophils. *Biophysical Journal* **46**, 383-386 (1984).

11 Rosenbluth, M. J., Lam, W. A. & Fletcher, D. A. Force microscopy of nonadherent cells: a comparison of leukemia cell deformability. *Biophys J* **90**, 2994-3003 (2006).

12 Jonas, O., Mierke, C. T. & Kas, J. A. Invasive cancer cell lines exhibit biomechanical properties that are distinct from their noninvasive counterparts. *Soft Matter* **7**, 11488-11495 (2011).

13 Thoumine, O. & Ott, A. Time scale dependent viscoelastic and contractile regimes in fibroblasts probed by microplate manipulation. *J Cell Sci* **110 (Pt 17)**, 2109-2116 (1997).

14 Reid, H. L., Barnes, A. J., Lock, P. J., Dormandy, J. A. & Dormandy, T. L. A simple method for measuring erythrocyte deformability. *Journal of clinical pathology* **29**, 855-858 (1976).

15 Worthen, G. S., Schwab, B., 3rd, Elson, E. L. & Downey, G. P. Mechanics of stimulated neutrophils: cell stiffening induces retention in capillaries. *Science* **245**, 183-186 (1989).

16 Downey, G. P. & Worthen, G. S. Neutrophil retention in model capillaries: deformability, geometry, and hydrodynamic forces. *J Appl Physiol* **65**, 1861-1871 (1988).

17 Otto, O. *et al.* Real-time deformability cytometry: on-the-fly cell mechanical phenotyping. *Nat Methods* **12**, 199-+ (2015).

18 Rowat, A. C. *et al.* Nuclear envelope composition determines the ability of neutrophil-type cells to passage through micron-scale constrictions. *Journal of Biological Chemistry* **288**, 8610-8618 (2013).

19 Rosenbluth, M. J., Lam, W. A. & Fletcher, D. A. Analyzing cell mechanics in hematologic diseases with microfluidic biophysical flow cytometry. *Lab Chip* **8**, 1062-1070 (2008).

20 Hou, H. W. *et al.* Deformability study of breast cancer cells using microfluidics *Biomedical Microdevices* **11**, 557-564 (2009).

21 Gossett, D. R. *et al.* Hydrodynamic stretching of single cells for large population mechanical phenotyping. *Proc Natl Acad Sci U S A* **109**, 7630-7635 (2012).

22 Sharma, S., Santiskulvong, C., Rao, J., Gimzewski, J. K. & Dorigo, O. The role of Rho GTPase in cell stiffness and cisplatin resistance in ovarian cancer cells. *Integr Biol (Camb)* (2014).

23 Sharma, S. V. *et al.* Correlative nanomechanical profiling with super-resolution F-actin imaging reveals novel insights into mechanisms of cisplatin resistance in ovarian cancer cells. *Nanomedicine* **8**, 757-766 (2011).

24 Frank, R. S. & Tsai, M. A. The behavior of human neutrophils during flow through capillary pores. *J Biomech Eng* **112**, 277-282 (1990).

25 Byun, S. *et al.* Characterizing deformability and surface friction of cancer cells. *Proc Natl Acad Sci U S A* **110**, 7580-7585 (2013).

26 Gabriele, S., Benoliel, A. M., Bongrand, P. & Theodoly, O. Microfluidic investigation reveals distinct roles for actin cytoskeleton and myosin II activity in capillary leukocyte trafficking. *Biophys J* **96**, 4308-4318 (2009).

27 Hendrickson, G. R. & Lyon, L. A. Microgel Translocation through Pores under Confinement. *Angew Chem Int Edit* **49**, 2193-2197 (2010).

28 Agbangla, G. C., Climent, E. & Bacchin, P. Experimental investigation of pore clogging by microparticles: Evidence for a critical flux density of particle yielding arches and deposits. *Sep Purif Technol* **101**, 42-48 (2012).

29 Wyss, H. M., Blair, D. L., Morris, J. F., Stone, H. A. & Weitz, D. A. Mechanism for clogging of microchannels. *Phys Rev E* **74** (2006).

30 Ekpenyong, A. E. *et al.* Viscoelastic properties of differentiating blood cells are fate- and function-dependent. *PLoS One* **7**, e45237 (2012).

31 Wu, T. H. *et al.* The F-actin and adherence-dependent mechanical differentiation of normal epithelial cells after TGF-beta1-induced EMT (tEMT) using a microplate measurement system. *Biomed Microdevices* **16**, 465-478 (2014).

32 Schneider, D. *et al.* Tension Monitoring during Epithelial-to-Mesenchymal Transition Links the Switch of Phenotype to Expression of Moesin and Cadherins in NMuMG Cells. *Plos One* **8** (2013).

33 Pylayeva-Gupta, Y., Grabocka, E. & Bar-Sagi, D. RAS oncogenes: weaving a tumorigenic web. *Nat Rev Cancer* **11**, 761-774 (2011).

34 Guadamillas, M. C., Cerezo, A. & Del Pozo, M. A. Overcoming anoikis--pathways to anchorage-independent growth in cancer. *J Cell Sci* **124**, 3189-3197 (2011).

35 Thiery, J. P. Epithelial-mesenchymal transitions in tumour progression. *Nature Reviews Cancer* **2**, 442-454 (2002).

36 De Craene, B. *et al.* The transcription factor snail induces tumor cell invasion through modulation of the epithelial cell differentiation program. *Cancer Research* **65**, 6237-6244 (2005).

37 Martin, F. T. *et al.* Potential role of mesenchymal stem cells (MSCs) in the breast tumour microenvironment: stimulation of epithelial to mesenchymal transition (EMT). *Breast cancer research and treatment* **124**, 317-326 (2010).

38 Byun, S. *et al.* Characterizing deformability and surface friction of cancer cells. *Proceedings of the National Academy of Sciences of the United States of America* **110**, 7580-7585 (2013).

39 Tsai, M. A., Waugh, R. E. & Keng, P. C. Passive Mechanical Behavior of Human Neutrophils: Effects of Colchicine and Paclitaxel. *Biophysical Journal* **74**, 3282-3291 (1998).

40 Tsai, M. A., Frank, R. S. & Waugh, R. E. Passive Mechanical Behavior of Human Neutrophils: Effects of Cytochalasin B. *Biophys J* **66**, 2166-2172 (1994).

41 Zhou, J. & Giannakakou, P. Targeting microtubules for cancer chemotherapy. *Curr Med Chem Anticancer Agents* **5**, 65-71 (2005).

42 Yvon, A. M., Wadsworth, P. & Jordan, M. A. Taxol suppresses dynamics of individual microtubules in living human tumor cells. *Mol Biol Cell* **10**, 947-959 (1999).

43 Liebmann, J. E. *et al.* Cytotoxic Studies of Paclitaxel (Taxol) in Human Tumor-Cell Lines. *Brit J Cancer* **68**, 1104-1109 (1993).

44 Godwin, A. K. *et al.* High-Resistance to Cisplatin in Human Ovarian-Cancer Cell-Lines Is Associated with Marked Increase of Glutathione Synthesis. *P Natl Acad Sci USA* **89**, 3070-3074 (1992).

45 Santiskulvong, C. *et al.* Dual Targeting of Phosphoinositide 3-Kinase and Mammalian Target of Rapamycin Using NVP-BEZ235 as a Novel Therapeutic Approach in Human Ovarian Carcinoma. *Clinical Cancer Research* **17**, 2373-2384 (2011).

46 Sharma, S. *et al.* Correlative nanomechanical profiling with super-resolution F-actin imaging reveals novel insights into mechanisms of cisplatin resistance in ovarian cancer cells. *Nanomed-Nanotechnol* **8**, 757-766 (2012).

47 Harada, T. *et al.* Nuclear lamin stiffness is a barrier to 3D migration, but softness can limit survival. *J Cell Biol* **204**, 669-682 (2014).

48 Engler, A. J., Sen, S., Sweeney, H. L. & Discher, D. E. Matrix elasticity directs stem cell lineage specification. *Cell* **126**, 677-689 (2006).

49 Halder, G., Dupont, S. & Piccolo, S. Transduction of mechanical and cytoskeletal cues by YAP and TAZ. *Nat Rev Mol Cell Bio* **13**, 591-600 (2012).

50 Elimelech, M. & Bhattacharjee, S. A novel approach for modeling concentration polarization in crossflow membrane filtration based on the equivalence of osmotic pressure model and filtration theory. *J Membrane Sci* **145**, 223-241 (1998).

51 Hong, S., Faibish, R. S. & Elimelech, M. Kinetics of permeate flux decline in crossflow membrane filtration of colloidal suspensions. *J Colloid Interf Sci* **196**, 267-277 (1997).

CHAPTER 2

A scalable filtration method for high throughput screening based on cell deformability

Abstract

Cell deformability is a label-free biomarker of cell state in physiological and disease contexts ranging from stem cell differentiation to cancer progression. Harnessing deformability as a phenotype for screening applications requires a method that can simultaneously measure the deformability of hundreds of cell samples and can interface with existing high throughput facilities. Here we present a scalable cell filtration device, which relies on the pressure-driven deformation of cells through a series of pillars that are separated by micron-scale gaps on the timescale of seconds: less deformable cells occlude the gaps more readily than more deformable cells, resulting in decreased filtrate volume which is measured using a plate reader. The key innovation in this method is that we design customized arrays of individual filtration devices in a standard 96-well format using soft lithography, which enables multiwell input samples and filtrate outputs to be processed with higher throughput using automated pipette arrays and plate readers. To validate high throughput filtration to detect changes in cell deformability, we show the differential filtration of human ovarian cancer cells that have acquired cisplatin-resistance, which is corroborated with cell stiffness measurements using quantitative deformability cytometry. We also demonstrate differences in the filtration of human cancer cell lines, including ovarian cancer cells that overexpress transcription factors (Snail, Slug), which are implicated in epithelial-to-mesenchymal transition; breast cancer cells (malignant *versus* benign); and prostate cancer cells (highly *versus* weekly metastatic). We additionally show how the filtration of ovarian cancer cells is affected by treatment with drugs known to perturb the cytoskeleton and the nucleus. Our results across multiple cancer cell types with both genetic and pharmacologic manipulations demonstrate the potential of this scalable filtration device to screen cells based on their deformability.

Graphical abstract

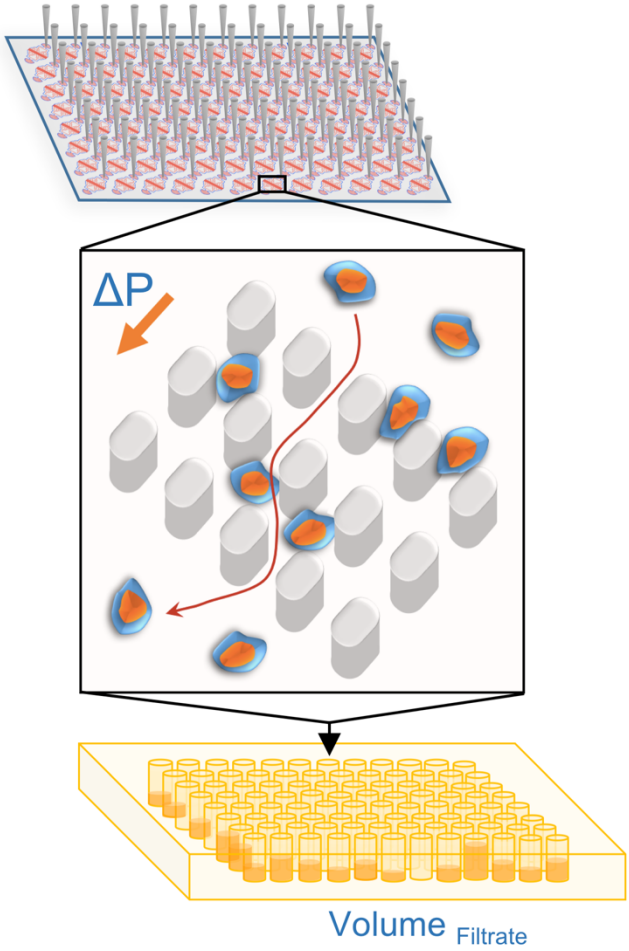

Introduction

High throughput (HT) assays enable screening of cells against thousands of compounds in chemical libraries[1-4]. Typical screens are based on molecular readouts such as gene or protein expression[5-7], or cellular behaviors such as proliferation[8,9], apoptosis[10,11], or invasion[12,13]. Screens based on such molecular and cellular metrics have enabled the identification of drugs with clinical efficacy[14,15]. For example, the commonly used anti-cancer agent, paclitaxel, was discovered in a high throughput screen based on its ability to stop cell proliferation[16]. While the development of treatment strategies using existing drugs has led to significant progress in improving patient survival and disease outcome[17-21], the majority of deaths occur due to metastasis and

recurrence[22-24]. Thus, there is an urgent need to identify novel therapeutic agents. A promising strategy to discover new compounds is by assaying alternative cellular phenotypes that are implicated in cancer progression and metastasis[25], such as cellular metabolism[26], adhesion[13,27], or deformability[28-31].

Screening for chemotherapeutics based on the intrinsic deformability of cells has exciting potential. A variety of clinically used chemotherapy agents, such as daunorubicin and paclitaxel, increase the stiffness of cancer cells[28,32-34]; this induced stiffening may result from cell death[32] and/or stabilization of microtubules to cause cell cycle arrest and stop proliferation[28,35]. Other desirable targets for cancer therapies include Rho GTPase[36] and Rho-associated protein kinase[37], which regulate actin structure, dynamics, and cell motility; these are also major regulators of cellular deformability[36,38,39]. Since the deformability of cancer cells is associated with cellular invasion[29,40-42], compounds that make cancer cells stiffer may also decrease their invasion. Consistent with this idea, we previously found that ovarian cancer cells (OVCA433) with induced expression of transcription factors implicated in epithelial-to-mesenchymal transition are more deformable than epithelial-like cells[28]; EMT is also accompanied by increased cell invasion[43]. Our previous work also shows that ovarian cancer cells with acquired resistance to the common chemotherapy agent cisplatin have mesenchymal-type features and are more deformable than cisplatin-sensitive cells[28]. Thus, identifying small molecules based on their ability to revert the deformability of cancer cells—especially mesenchymal-like, drug-resistant cells—to levels of less invasive and/or normal cells could provide a route to identify complementary compounds that inhibit cancer cell behaviors such as proliferation and motility.

While cancer cell deformability as a phenotype has potential for drug discovery, there are thousands of drugs in typical libraries for high throughput screening. However, existing mechanotyping methods rely on sequential measurements of individual cell samples. Methods to measure cell mechanical properties, such as atomic force microscopy or magnetic twisting cytometry, achieve measurements of elastic modulus through detailed force-deformation profiling

on single cells, but have limited throughput[44-47]. Microfluidic-based methods enable rapid measurements of the deformability of single cell populations[48-50], but rely on customized image analysis of individual cells and samples sequentially, which is a computationally expensive bottleneck. Such methods are thus challenging to integrate into high throughput facilities that rely on treating and processing hundreds of samples in multiwell plates simultaneously. If a method to measure cell deformability could be integrated into existing high throughput sample handling platforms that use multiwell inputs and readouts, this would facilitate deformability to be used as a phenotype for drug discovery.

To enable simultaneous measurements of cell deformability, we recently developed the parallel microfiltration method[28,51]. Parallel microfiltration relies on the filtration of a cell suspension across a polycarbonate membrane with micron-scale pores; stiffer cells are more likely to occlude pores compared to more deformable cells. The concept of filtration for measuring cell deformability has been established for different red and white blood cell types[52-54], as well as cancer cells[28,41,42]. While we previously established proof-of-concept measurements of cell deformability using a prototype parallel microfiltration device, there are numerous challenges to scaling up this method. The prototype device requires measuring the retained sample volumes across the plate, which involves additional steps of liquid handling. Moreover, manual assembly is required to set up the device: commercially available polycarbonate membranes are manually placed in the prototype device, which is tightened to achieve a pressure-tight seal[28]. Such manual processing introduces user variation, and thus measurement variability. All of these challenges hinder the scale-up of parallel microfiltration for robust, HT assays.

Here we present a scalable high throughput filtration (HTF) method that enables multiple samples to be measured simultaneously. Inspired by strategies to scale-up microfluidic devices for HT applications[55-59], the core of HTF is a custom-fabricated array of 96 microfiltration devices; each device contains a series of pillars with well-defined micron-scale gaps from 6 to 14 μm that are smaller than the diameter of single cells. Cells are driven to passively deform through the

gaps on the timescale of seconds to minutes in response to applied pressure. The ability of cells to deform through the gaps determines the fluidic resistance of a single device: a larger number of cells that occlude gaps results in a higher fluidic resistance, less flow through the filtration device, and thus a smaller filtrate volume. Importantly, the volume of collected filtrate can be rapidly measured in multiwell format using a plate reader, thereby enabling automation of cell filtration measurements. To characterize the HTF method and operational parameters, we measure the filtration of cisplatin-sensitive (OVCAR5 Cis-S) *versus* -resistant human ovarian cancer (OVCAR5 Cis-R) cells, which we independently confirm have distinct elastic moduli using quantitative deformability cytometry[60]. To validate the HTF method to distinguish cell samples, we screen human ovarian cancer (OVCA433 GFP, Snail and Slug) cells with induced EMT by overexpression of transcription factors (Snail, Slug), and treat these cells with a panel of cytoskeletal and nuclear perturbing drugs that modulate cell deformability. To demonstrate broader applicability of HTF for screening cells based on cell deformability, we filter malignant human breast cancer cells (MDA-MB-468, MDA-MB-231) *versus* non-tumorigenic breast epithelial (MCF10A) cells, and weakly metastatic prostate cancer (DU145) cells *versus* DU145 cells transformed with knock down of nuclear envelope protein, emerin (DU145 Emerin KD), which are highly metastatic. Taken together, our results demonstrate the potential of HTF as a scalable platform for screening based on cell deformability.

Methods

Cell culture: Human ovarian cancer (OVCA433), breast cancer (triple negative MDA-MB-468 and MDA-MB-231), and prostate cancer (DU145) cells are cultured in DMEM (+L-Glutamine, +Glucose, +Sodium Pyruvate) supplemented with 10% FBS, 1% Anti-anti (Gibco). For OVCA433 GFP (control), SNAI1-overexpressing cells (OVCA433 Snail), and SNAI2-overexpressing cells (OVCA433 Slug)[28] we use the same media with the addition of blasticidin S HCl (5 μg/ml, Corning Cellgro). To culture the cisplatin-sensitive and -resistant cells, OVCAR5 Cis-S/OVCAR5 Cis-R,

we use Dulbecco's Modified Eagle Medium (DMEM) with 10% FBS, 1% Penicillin-Streptomycin, and 10 μM cisplatin (Sigma-Aldrich) for the resistant cells. To culture immortalized non-tumorigenic breast epithelial (MCF10A) cells, we use Mammary Epithelial Cell Growth Basal Medium (MEBM) (Lonza) supplemented with bovine pituitary extract (52 μg/mL), hydrocortisone (0.5 μg/mL), human EGF (10 ng/mL), and insulin (5 μg/mL) (MEGM Bullet Kit, Lonza) as well as 100 ng/mL cholera toxin (Sigma Aldrich). DU145 Emerin KD cells are cultured in DMEM with 10% FBS, 1% Penicillin-Streptomycin, and 2 μg/mL puromycin (Thermo Fisher Scientific). Prior to filtration measurements, cells are washed with 1x Phosphate-Buffered Saline (PBS, DNase-, RNase- & Protease- free, Mediatech, Manassas, USA), treated with trypsin, and resuspended in fresh medium to a density of 0.5 x 10^6 cells/mL. To minimize clusters of cells, cell suspensions are passed through a 35 μm cell strainer (BD Falcon) prior to each filtration measurement.

Drug treatments: Stock solutions of paclitaxel (451656, Corning Cellgro), cytochalasin-D (C8273, Sigma-Aldrich), colchicine (C9754, Sigma-Aldrich), paclitaxel (T7402, Sigma-Aldrich), blebbistatin (ab120425, Abcam), SB43154 (1614, Tocris), verteporfin (5305, Tocris), and trichostatin-A (1406, Tocris) are prepared according to manufacturer instructions. Cells are treated with 0.1 to 10 μM of drugs as indicated for 24 h prior to measurements.

Device fabrication: To fabricate the HTF microfluidic device array, two polydimethylsiloxane (PDMS, Sylgard 184 silicone elastomer, Dow Corning) layers are individually fabricated and then covalently bonded together. To produce the first layer that contains the 10 μm-height filtration devices, we spin coat SU-8 3005 photoresist (Microchem) at spin speed of 100 rpm to a thickness of 10 μm on a 6" silicon wafer (Silicon Valley microelectronics). The thickness of the photoresist is confirmed to be 9.7 ± 0.1 μm using a Dektak 150 Surface Profilometer (Veeco). A 10:1 w/w base to crosslinker ratio of PDMS is poured onto the master wafer, degassed using a desiccator vacuum for 20 minutes, and cured at 65 °C for 2 h. We use the same protocol to mold the second

layer that contains outlets that are cast using a 96 x 250 µL array of pipette tips. The surfaces of the two layers to be bonded are then exposed to UV light in the presence of ozone[61] for 5 minutes using a UVO cleaner 42 (Jetlight). Outlets in the second PDMS layer are aligned with the inlet regions of the filtration devices in the first PDMS layer and pressed gently to bond. Filtration measurements are performed 24 h after bonding to ensure consistent surface properties across experiments[62].

HT-cell filtration: Cell suspension (350 µL) at 0.5 x 10^6 cells/mL or otherwise shown cell concentration is loaded into each well of the 96-well loading plate. We adapt a plasmid filtration plate (HyperSep filter plate, Thermo Fisher) with filters removed as the loading plate. To measure cell number, we use an automated cell counter (TC20, BioRad); these measurements also yield cell size distributions. Defined air pressure is applied using pressurized air and monitored using a pressure gauge (0 - 100 kPa, Noshok Inc., Berea, OH, USA). To measure the filtrate volume, we determine the absorbance of the filtrate volume using plate reader. To rapidly optimize parameters for a particular cell type, we temporarily seal unused sections of the filtration device array by taping wells in the loading plate using laboratory paper tape (VWR).

Absorbance measurements: To quantify filtrate volumes, we measure the absorbance of the resultant cell suspensions in the 96-well collection plate. Since the cell medium contains phenol red, we measure absorbance at 560 nm using a plate reader (Infinite M1000, Tecan).

Cellular imaging: To image the cells that occlude the interpillar gaps during filtration, cells are labeled with Calcein-AM (5 µM, Invitrogen) prior to filtering through devices that are bonded to a glass coverslip. Images are acquired using a fluorescence microscope (Zeiss Observer A.1 Axio) equipped with a 10x objective (10x/EC Plan-Neofluar, 0.3 Ph1 M27, Zeiss), a light source (HBO

103W/2 mercury vapor short-arc lamp), and filter set 13 (Zeiss). To quantify % occluded gaps, we count the total number of gaps and occluded gaps.

Cell cycle analysis: To perform cell cycle analysis, adhered cells are harvested and resuspended in fresh medium to a density of 2 x 10^6 cells/mL. Cells are washed once in PBS containing 1% FBS (Gibco) by centrifugation and resuspended in 70% ethanol (Fisher Scientific) solution made in PBS. Cells are fixed in the ethanol solution overnight at -20 °C. Cells are washed once in PBS by centrifugation and stained with propidium iodide (PI) staining solution at a density of 2 x 10^6 cells/mL for 30 minutes at 37 °C. PI staining solution contains 50 ug/mL PI (Thermo Fisher Scientific), 2.5 mg/mL RNase solution (Invitrogen) in PBS. To minimize clusters of cells, cell suspensions are passed through cell strainer with 35 μm mesh size (BD Falcon) prior to analysis using flow cytometry (LSRFortessa cell analyzer, BD Falcon).

q-DC: Quantitative deformability cytometry (q-DC) is a microfluidic method that enables single-cell measurements of apparent elastic modulus, fluidity, and transit time through micron-scale constrictions[60]. To fabricate devices using soft lithography, a 10:1 w/w base to crosslinker ratio of polydimethylsiloxane (PDMS) is poured onto a master wafer. The device is subsequently bonded to a glass coverslip (1.5 thickness) using plasma treatment. Within 24 h of device fabrication, cell suspensions of 2 × 10^6 cells/mL are driven through constrictions of 9 μm (width) x 10 μm (height) by applying 55 kPa of air pressure. We capture images of cellular deformations on the millisecond timescale using a high-speed CMOS camera with a capture rate of 1600 frames/s (Vision Research, Wayne, New Jersey) that is mounted on an inverted microscope (Zeiss, Oberkochen, Germany) equipped with a 20x/0.40NA objective (Zeiss). We use a customized MATLAB code to analyse the time-dependent strain of individual cells. To determine the applied stress, we use agarose calibration particles that we fabricate using oil-in-water emulsions[60]. Stress-strain curves

are obtained for single cells and a power-law rheology model is fitted to compute cellular elastic modulus and fluidity[60].

Statistical methods: HTF results are expressed as mean ± SD. We use the Student's t-test method to analyze significance and obtain p-values. For the non-parametric distributions of apparent elastic modulus, fluidity, transit time and cell size, we use the Mann-Whitney U test to determine statistical significance.

HTF device concept

Theoretical framework. To drive the flow of cell suspension through individual filtration devices (**Fig 1A**), we apply air pressure uniformly across the array of devices. Each device contains rows of pillars spaced with an interpillar gap size that is ~2x smaller than the median cell diameter; thus, while cell medium flows freely through the gaps, cells that transit through gaps are required to deform with ~40 to 60% strains[60]. If a cell does not transit, it occludes the gap (**Fig 1B**). The probability of occlusion depends on the driving pressure, filtration time, cell-to-gap size ratio, and cell deformability[28,41,42,60]. For suspensions of cells that have a similar size distribution and are filtered at a fixed driving pressure, cell deformability is a major contributor to filtration[28,41,42,63,64]: stiffer cells with higher elastic moduli tend to occlude narrow gaps more frequently than more compliant cells with lower elastic moduli[28,65,66]. While cells are in contact with the pillar surface as they transit through narrow gaps, transit is dominated by the ability of cells to deform and change shape[60,64,67,68].

To understand the physical mechanism of HT filtration, we investigate how key experimental parameters—filtration time, cell density, and driving pressure—affect the filtration of a suspension of human ovarian cancer (OVCAR5 Cis-R) cells. We first investigate the time-dependence of filtration by imaging the pillar array over the filtration time period. At timescales of

30 to 120 s, we observe a monotonic increase in the number of occlusions as an increasing number of cells block the interpillar gaps (**Fig 1C, D**).

To further understand the changes in fluidic resistance that occur with filtration, we perform Monte Carlo simulations to predict filtrate volume over time. We consider the filtration device as an electric circuit[69] (**Fig 1A**), where R is the fluidic resistance, P_{inlet} is the driving pressure, P_{atm} is atmospheric pressure, and Q is the resultant fluid flow:

$$P_{inlet} - P_{atm} = QR.$$

As we observe experimentally that the number of occluded gaps increases linearly as a function of time (**Fig 1D**), we model the change in fluidic resistance as a function of the number of occluded gaps,

$$R(t) \sim \frac{R_{initial}}{\left(1 - \frac{N_{occluded}}{N_{total}}\right)},$$

where R_{intial} is the initial fluidic resistance, $N_{occluded}$ is the number of occluded gaps at a given time (t), and N_{total} is the total number of gaps. The Monte Carlo simulation determines the filtrate volume per time by iterating through time steps of 1 ms (**Fig 1E**). As cells occlude gaps, the fluidic resistance increases, which is consistent with a modified Darcy's Law[28]. Experimental measurements of filtrate volume obtained by filtration of OVCAR5 cisplatin-resistant (Cis-R) cells are in agreement with the simulations (**Fig 1E**), which validates this model describing the filtration process.

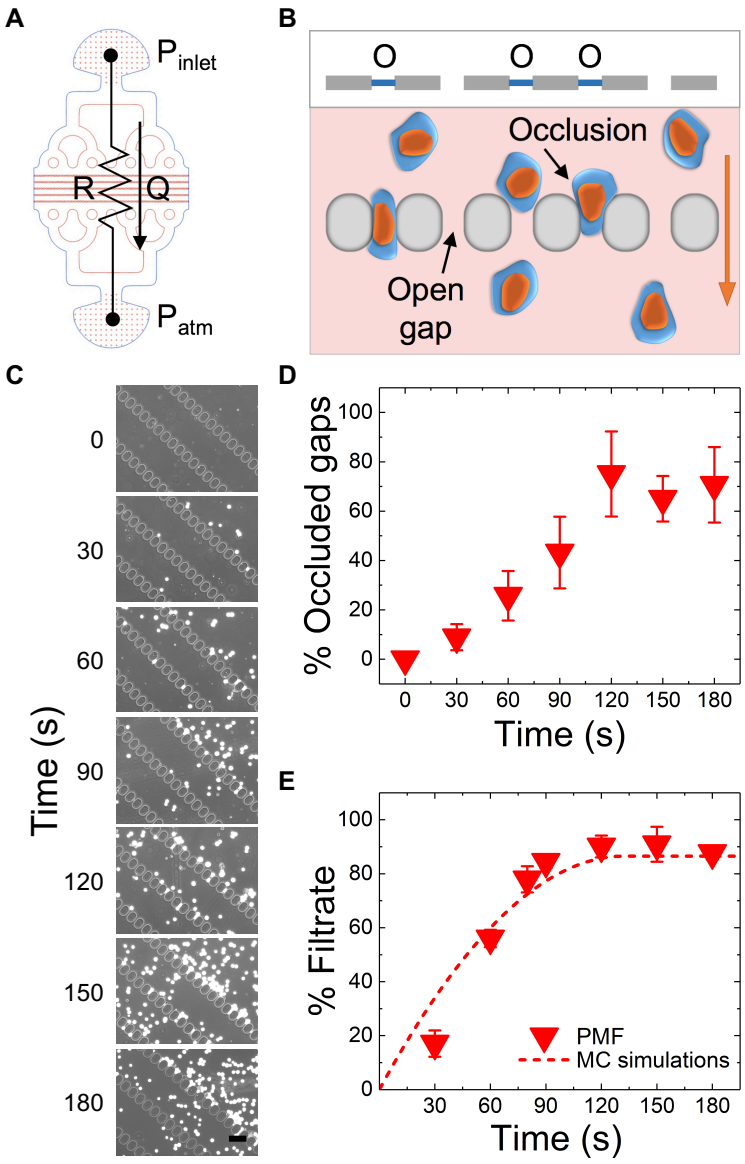

Figure 1. Defining the physical mechanism of HT filtration. (A) To simulate the filtration process, we consider the filtration device as an electric circuit, where *R* is the fluidic resistance, *Q* is the flow, P_{inlet} is the driving pressure, and P_{atm} is atmospheric pressure. (B) Schematic illustration showing simulation setup whereby fluidic resistance is determined by the number of occluded (O) *versus* open gaps. (C) Images of the pillar array over the filtration time. Brightfield images are overlaid with fluorescence to show OVCAR5 Cis-R cells (labeled with Calcein-AM) trapped in the array of pillars. Scale, 100 μm. (D) Quantification of occluded 10 μm gaps in HTF devices over the filtration time course for OVCAR5 Cis-R cells filtered at a driving pressure of 28 kPa and 0.5 x 10^6 cells/mL. Each data point represents mean ± SD from two independent experiments. (E) The percentage of the initial loaded volume collected as filtrate is defined as % Filtrate. Plot shows % Filtrate as a function of time. Triangles show experimental data obtained for OVCAR5 Cis-R cells filtered through 10 μm gaps at a driving pressure of 28 kPa for 90 s with 0.5 x 10^6 cells/mL. Each data point represents mean ± standard deviation (SD) over three independent experiments. Dashed line shows results of Monte Carlo (MC) simulations.

HTF device fabrication & operation

Device fabrication. To scale up the filtration assay so that multiple cell samples can be measured simultaneously, we fabricate an array of 96 microfluidic filtration devices using soft lithography. The HTF device array consists of two polydimethylsiloxane (PDMS) layers, which are each fabricated separately and then bonded together (**Fig 2A**). One PDMS layer contains the individual filtration devices that are fabricated using standard photolithography methods to have a customized array of micron-scale gaps (**Fig 2B-D**) and a height of 10 μm[70]. To produce inlets that align with 96-well plates, we use an array of 96 x 250 μL pipette tips as a mold (**Fig 2A**). The other layer contains the outlets and is fabricated by pouring PDMS onto a plain silicon wafer and casting holes using the same array of 96 pipette tips; the resultant holes are then aligned with the outlets of the devices in the upper layer. The two layers are covalently bonded together by exposing to UV light in the presence of ozone[61,71]. To enable insertion of tubing simultaneously across 96 wells, we custom-fabricate a spacer plate out of polylactic acid using 3D printing (**Fig 2E10**), and affix outlet tubing that inserts into the molded outlets of the second PDMS layer. To load samples into the devices, we fabricate a loading plate that consists of a 96-well plate with protrusions at the bottom of each well (**Fig 2E6**), which insert directly into the inlet holes of the top PDMS layer (**Fig 2E9**). The assembled two-layer HTF device array with the attached loading and spacer plates is inserted into a custom-built plate holder (**Fig 2E8**), which is placed on top of a standard 96-well plate (**Fig 2E11**) in which the filtrate is collected. While we demonstrate here fabrication of a 96-array device, the procedure is scalable and could be modified to generate arrays of devices that interface with a range of plate sizes from 24 to 384-wells. Importantly, the customizable architecture of the HTF device enables fabrication of device arrays that have a range of gap sizes, which can enable rapid determination of the optimal gap size for filtration in a single experiment.

Device operation. To load the device, suspensions of cells in media are transferred into the loading plate using a 96-pin multichannel head. To apply uniform air pressure to drive cell suspensions through the filtration devices uniformly across the device array, we secure a pressure chamber (**Fig 2E2**) on top of the plate holder using clamps (**Fig 2E5**); placement of a rubber sealing pad (**Fig 2E4**) between the holder and the pressure chamber ensures air-tight sealing. To apply a well-defined magnitude of positive air pressure we use compressed air (via **Fig 2E3**), which is monitored using a pressure gauge (**Fig 2E1**), as displayed in **Fig 2F**. Upon applying air pressure, the cell suspensions are driven to enter into each device; the resultant filtrate containing cells and media that have filtered through the device is measured by determining the absorbance of phenol red (560 nm), which is contained in the cell media, as an indicator of filtrate volume; such measurements can be obtained using a plate reader in a multiwell plate format. To equate absorbance and filtrate volume, we generate a standard curve and confirm that the presence of cells in the media has no effect on absorbance (**Supp Fig 1A**), substantiating that absorbance measurements can be used to reliably report filtration volume.

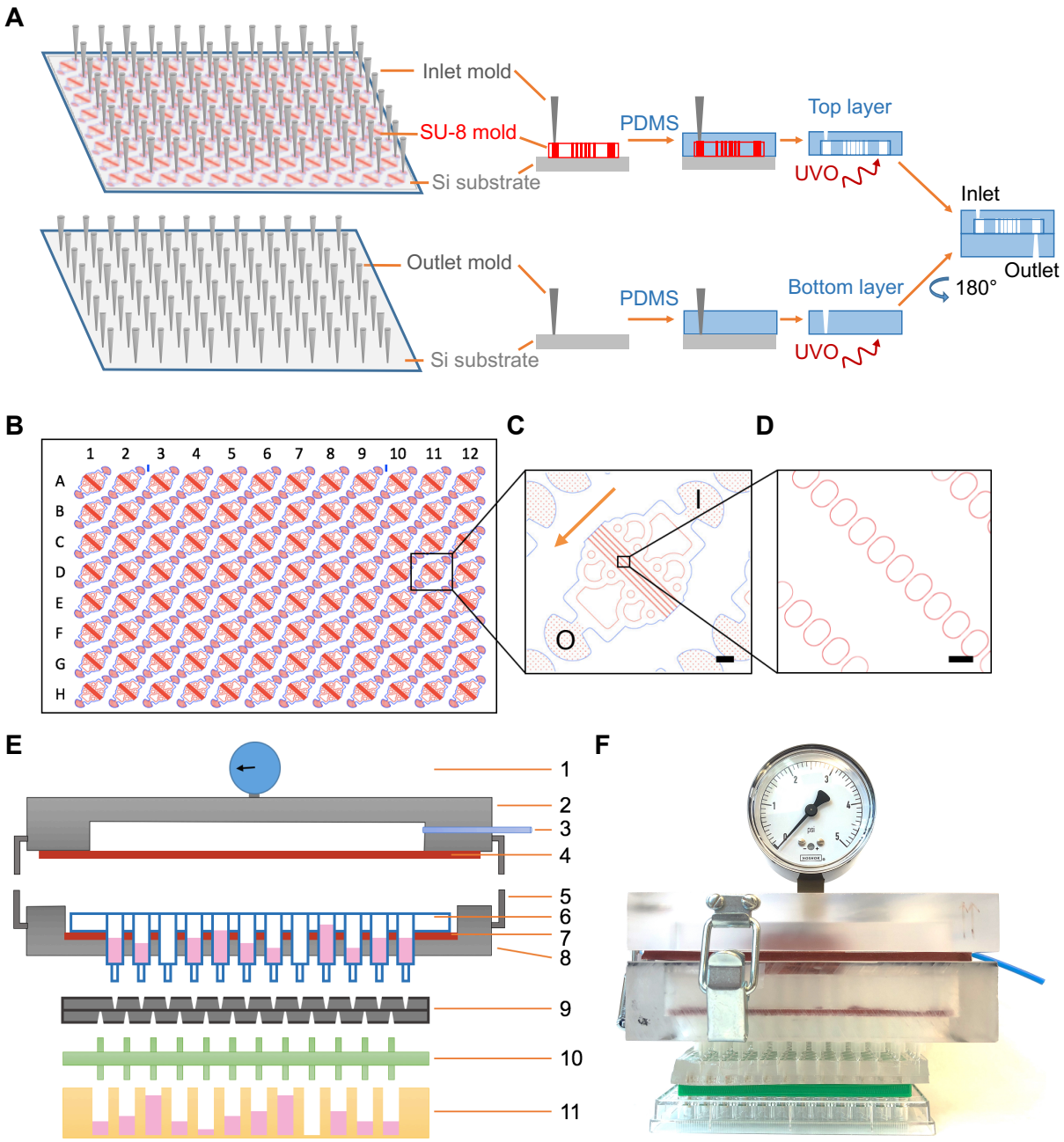

Figure 2. Architecture of the HTF system. (A) Schematic showing fabrication of the two-layer PDMS array of devices that is fabricated by bonding together top and bottom PDMS layers. Inlets and outlets are molded using a standard 96-array of pipette tips. (B) Plan view of array of 96 filtration devices. Inset shows: (C) single filtration device. Arrow indicates direction of fluid flow from inlet (I) to outlet (O). Scale, 1 mm. Inset shows: (D) array of pillars with defined interpillar gap size through which cells are filtered. Scale, 100 μm. (E) Schematic of HTF system: 1. Pressure gauge; 2. Pressure chamber; 3. Connection to pressure source; 4. Rubber sealing pad; 5. Clamps; 6. Loading plate; 7. Rubber sealing pad; 8. Custom fabricated plate holder; 9. PDMS array of devices; 10. Spacer plate with affixed tubing; and 11. Standard 96 well filtrate collection plate. (F) Photo of the HTF system.

Results and Discussion

Optimizing conditions for the HTF assay

We first demonstrate the process of optimizing HTF for a single cell type using OVCAR5 Cis-R cells for proof-of-concept. A key parameter for cell filtration is the gap size. The magnitude of filtration at a given pressure and time depends on the probability that cells will occlude the gaps, which is determined by cell deformability and cell size relative to the gap size[62,65]. When the gap size is larger than the cell diameter, no deformation is required for cells to flow through the gaps. When the gap size is smaller than the cell size, cells are required to deform through the gap. With increasingly smaller gaps there is increasing probability of occlusion. We previously established filtration conditions for OVCAR5 Cis-R cells with 10 μm pore membranes that yield a filtrate volume of ~40-60%[28]; this is optimal to simultaneously detect samples with both increased or decreased filtration in a parallel assay. Therefore, we use HTF devices with 10 μm gap size to optimize cell density and filtration pressure for these OVCAR5 Cis-R cells.

Since the number of cells flowing through the pillars per volume per time sets the rate of occlusion, filtration measurements are sensitive to cell density[28]. With a low cell density there are fewer occlusions and thus minimal changes to fluidic resistance, which precludes differential measurements between samples. By contrast, with higher cell densities, cells may cluster at the interpillar gaps, which can be observed over longer filtration times (**Fig 1C**); such clustering can result in decreased filtrate volume but may be sensitive to cell-cell interactions rather than single cell deformability. To determine the optimal cell density for filtration of human ovarian cancer cells, we assess the filtration of OVCAR5 Cis-R cells over a range of cell densities from 0.1 x 10^6 to 3.0 x 10^6 cells/mL at a fixed filtration pressure and time (28 kPa, 90 s). With increasing cell density, we observe a reduction in absorbance indicating decreased filtrate volume (**Supp Fig 1B**); this is consistent with the higher probability of occlusion and subsequent increased fluidic resistance. With cell densities > 1.5 x 10^6 cells/mL, we find there are no further observable changes in filtration, reflecting significant occlusion of interpillar gaps. At densities < 0.3 x 10^6 cells/mL, we

observe 88.5 ± 4.9% filtrate; since the dead volume of the device is ~44 µL, this is the maximum measurable filtrate. Based on these findings, we determine the optimal cell density for filtration of human ovarian cancer cells is 0.5 x 10^6 cells/mL; at this density a sufficient number of occlusions occurs to yield a measurable filtrate while requiring the minimal number of cells.

Another essential parameter in filtration is the driving pressure, which drives fluid flow and thus impacts the number of cells that arrive at the pillars per unit time. The driving pressure must be sufficient to generate flow of cell suspension through the array of pillars, yet not excessive to completely filter the sample volume, which would preclude differential filtration measurements. To define the optimal driving pressure for OVCAR5 Cis-R cells, we conduct a pressure sweep from 14 kPa to 35 kPa. With increasing driving pressure, we observe increased filtration, with % filtrate values that range from 41.4 to 88.5% (**Supp Fig 1C**). The driving pressure for a particular experiment should be set according to the goals of the screen. For example, to design a screen where desired hits increase cell deformability, a control filtrate value around ~20% will ensure detection of compounds that result in the largest increase in % filtrate; to identify compounds that decrease cell deformability and thereby lower % filtrate, the control % filtrate should be ~80%. It is important to note that to rapidly optimize pressure, time, and gap size for a particular cell type, sections of the customized 96-device array can be used by temporarily sealing unused wells in the loading plate using laboratory paper tape. Moreover, while we only show optimization of HTF parameters for OVCAR5 Cis-R cells, the settings can be readily applied to other cancer cell types with similar cell size distributions (cell to gap size ratio from ~1.3 to 1.8).

We next demonstrate the optimization of HTF to maximize the difference in readouts between 2 cell samples. As proof-of-concept, we establish conditions for HTF to distinguish between the OVCAR5 Cis-R and OVCAR5 Cis-S cells, which we previously found have distinct filtration properties using the parallel microfiltration prototype device[28]. We first optimize driving pressure to maximize the difference in % filtrate between OVCAR5 Cis-S and Cis-R cells. The optimal driving pressure should maximize the difference in filtration between cell types within the

range of ~7 to 88% filtrate, which is the dynamic range of filtrate measurements. To establish the optimal driving pressure for OVCAR5 Cis-S and Cis-R cells, we perform a pressure sweep from 14 kPa to 35 kPa at a fixed filtration time of 90 s (**Supp Fig 1C**). We find the Cis-R cells have higher % filtrate than Cis-S cells, consistent with our previous observations of the increased filtration of Cis-R *versus* Cis-S cells through the 10 μm-pores of a polycarbonate membrane[28]. As we observe the maximum difference in filtrate between OVCAR5 Cis-S and Cis-R at 28 kPa, we select this driving pressure for subsequent experiments. The observed differential filtration of OVCAR5 Cis-S *versus* Cis-R cells reflects a difference in how these cells deform through narrow gaps (Fig 3A). A difference in cell size could impact filtration, however, comparisons of cell size distributions between Cis-S and Cis-R cells reveal no significant differences (**Supp Fig 2A**), indicating that cell size alone cannot explain the differential filtration. Cell physical properties also vary with stages of the cell cycle[48,72], however, we find no significant differences in cell cycle stage between Cis-R and Cis-S cells (**Supp Fig 2B**).

HTF is sensitive to cell deformability

To test the effects of cell deformability on filtration of OVCAR5 Cis-R and Cis-S cells, we pharmacologically perturb the cytoskeleton by treating cells with paclitaxel, which stabilizes microtubules and causes cells to be stiffer[28,34,35]. We find that treatment of OVCAR5 Cis-R cells with 0.1 μM paclitaxel results in a reduction of % filtrate to 23.5 ± 9.7% compared to vehicle control of 87.6 ± 4.9% ($p = 5.3 \times 10^{-4}$) (**Fig 3B**); this is consistent with increased cell stiffness following paclitaxel treatment. We also observe a smaller but significant reduction in filtrate of paclitaxel-treated OVCAR5 Cis-S cells from 34.1 ± 15.4% to 15.8 ± 5.8% ($p = 9.0 \times 10^{-4}$); this smaller effect may be attributed to the narrow range for decrease in filtrate absorbance in the lower end of the dynamic range. We verify that paclitaxel treatment does not have a significant effect on size of the Cis-R and Cis-S cells, indicating that differential filtration of these paclitaxel-treated cells reflects changes in cell deformability (**Supp Fig 2C)**.

To confirm the distinct mechanical properties of the OVCAR5 Cis-R and Cis-S cells using an independent method, we measure the apparent elastic modulus (E_a), fluidity (β), and transit time (TT) of these cells through micron-scale constrictions of a microfluidic device using quantitative deformability cytometry (q-DC)[60]. We find that Cis-R cells have a ~21.9% lower E_a (**Fig 3C, D**) and ~10.0% increased β compared to Cis-S cells (**Fig 3E, F**), indicating they are more compliant (median $E_{a\_Cis\text{-}R}$ = 1.32 kPa *versus* $E_{a\_Cis\text{-}S}$ = 1.69 kPa , p = 1.4 x 10^{-8}; median $\beta_{Cis\text{-}R}$ = 0.33 *versus* $\beta_{Cis\text{-}S}$ = 0.30, p = 3.9 x 10^{-6}). Cis-R cells also exhibit a faster transit time through micron-scale constrictions compared to Cis-S cells (median $TT_{Cis\text{-}R}$ = 15.0 ms *versus* $TT_{Cis\text{-}S}$ = 34.8 ms, p = 3.9 x 10^{-33}) (**Fig 3G, H**). Since measurements of E_a and β using q-DC are sensitive to the magnitude of deformation[60], and the constriction size is fixed, these measurements could also be sensitive to cell size; however, we find no significant correlation between the measured cell diameters (d) and q-DC measurements (Pearson's r: $(E_a \text{ vs } d)_{Cis\text{-}R\_}$ = 0.0, $(E_a \text{ vs } d)_{Cis\text{-}S}$ = 0.0; $(\beta \text{ vs } d)_{Cis\text{-}R}$ = -0.1, $(\beta \text{ vs } d)_{Cis\text{-}S}$ = 0.0; $(TT \text{ vs } d)_{Cis\text{-}R}$ = 0.0, $(TT \text{ vs } d)_{Cis\text{-}S}$ = 0.1). Taken together, these findings substantiate that differences in cell deformability can be detected by differences in % filtrate using HTF.

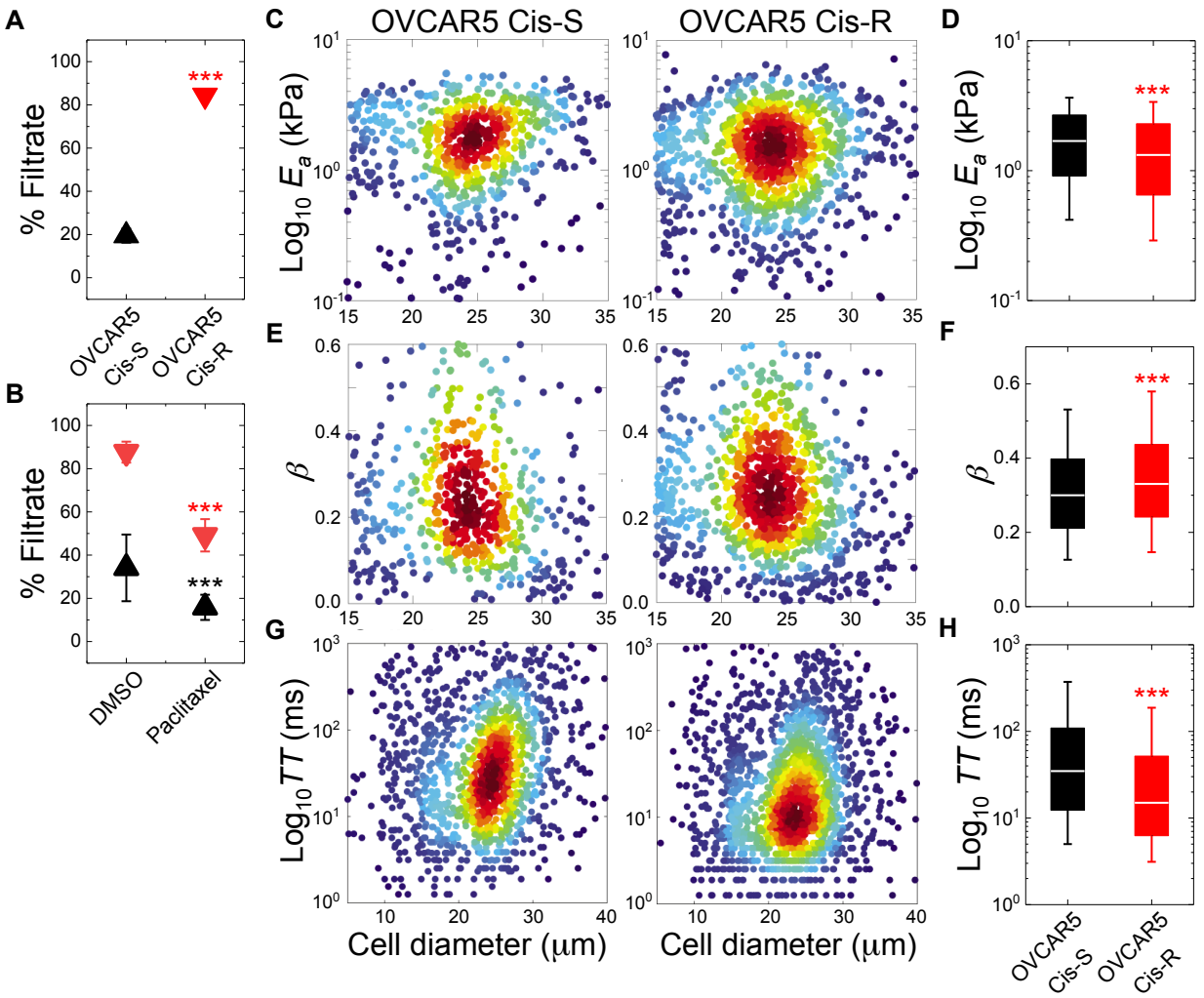

Figure 3. HTF is sensitive to cell deformability. Differential filtration of (A) human ovarian cancer OVCAR5 Cis-R and Cis-S cells and (B) OVCAR5 Cis-R and Cis-S cells treated with 0.1 μM of the microtubule-stabilizing drug paclitaxel for 24 h prior to filtration through 10 μm gaps at 28 kPa, 90 s, and 0.5 x 10^6 cells/mL. Data points in A and B represent mean ± SD from three independent experiments. Statistical significance is determined using student's t-test. (C) Density scatter plots for measurements of apparent cell elastic modulus (E_a) using quantitative deformability cytometry (q-DC). Each dot represents a single cell. N > 700 per sample. (D) Box plots showing E_a measurements. (E) Density scatter plots for measurements of cell fluidity (β) using q-DC. Each dot represents a single cell. N > 700 per sample. (F) Box plots showing β measurements. (G) Density scatter plots for measurements of cell transit time (TT) using q-DC. Each dot represents a single cell. N > 1300 per sample. (H) Box plots showing TT measurements. Box plots show the 25th and 75th percentiles; whiskers denote 10th and 90th percentiles; and line is the median. Statistical significance is determined using the Mann Whitney U test. *** $p < 0.001$; ** $p < 0.01$; * $p < 0.05$.

Resolving cell types based on differential filtration

To validate ability of HTF to measure differences in filtration based on cell deformability, we investigate a set of three cell lines that represent both epithelial- and mesenchymal-like

phenotypes. EMT is implicated in cancer progression and metastasis, as mesenchymal-type cells tend to be more motile and invasive[43]. We and others previously showed that mesenchymal-type cells are more deformable than epithelial-type cells[28,73]. To investigate the filtration of epithelial- and mesenchymal-type cells using HTF, we compare human ovarian cancer (OVCA433) cells that are epithelial-type (OVCA433 GFP) and mesenchymal-type by transforming cells to overexpress genes (SNAI1, SNAI2) that are master regulators of EMT (OVCA433 Snail, OVCA433 Slug)[28].

To determine HTF conditions that maximize the difference in filtrate between epithelial-type control (OVCA433 GFP) cells and mesenchymal-type (OVCA433 Snail, OVCA433 Slug) cells, we first confirm the optimal interpillar gap size. Given the median cell size of 15 μm for OVCAR433 GFP, OVCAR433 Slug, and OVCAR433 Snail cells (**Supp Fig 2D**), we investigate filtration through devices with varying interpillar gap sizes from 6 to 14 μm within a single 'calibration' experiment (**Fig 4A**). Our findings confirm that a gap size of 10 μm achieves the largest difference in filtrate volume between epithelial and mesenchymal-type cells at a fixed driving pressure of 28 kPa and 60 s filtration time (p_{Snail} = 9.6 x 10^{-4}, p_{Slug} = 3.0 x 10^{-3}) (**Fig 4B**). We observe no significant differences in cell size distributions for these cells (**Supp Fig 2D**), thereby excluding differences in size as a cause of the differential filtration. We find no significant differences in cell cycle stage among these cell lines (**Supp Fig 2E**), which could also impact cell deformability[48,72]. We also observe no differences in filtration of these cells with or without surfactant (Pluronics F-127) (**Supp Fig 2F**), which minimizes cell-PDMS interactions[62]. These findings are consistent with previous observations that the ability of cells to transit through micron-scale pores is largely determined by cell deformability rather than surface effects on these ~90 s timescales[60,64,67,68]. Another possible origin of the decreased filtrate of the epithelial-type cells may be increased cell-cell interactions. However, we previously found that despite the higher E-cadherin expression of OVCA433 GFP cells compared to OVCA433 Snail and Slug, there were no significant differences in cell clustering on the timescales of these filtration measurements[28].

Taken together, these observations suggest the increased filtration of the mesenchymal-type cells reflects their increased deformability. More broadly, this process of optimizing gap size to maximize resolution between samples within a single calibration experiment provides a framework for adapting HTF to new cell types and screening applications.

To further investigate the applicability of HTF to other cell types, we conduct filtration experiments with human breast cancer cells including malignant triple negative (MDA-MB-468 and MDA-MB-231) as well as immortalized breast epithelial (MCF10A) cells[74]. Given the similar size distributions of the breast and ovarian cell lines (**Supp Fig 2A, D, G**), we first tested the same HTF conditions as optimized for the ovarian cancer cell lines (10 μm gap, 28 kPa for 60 s). With these conditions, we observe a significant ~10.4 to 33.5% increased filtrate for malignant breast cancer cells compared to the benign cells ($p_{MDA\text{-}MB\text{-}468} = 1.3 \times 10^{-2}$; $p_{MDA\text{-}MB\text{-}231} = 1.7 \times 10^{-5}$) indicating that the malignant cells are more deformable than the benign cells (**Fig 4C**). These observations are consistent with previous reports that malignant human cell lines[40,75,76] and cells from patient pleural effusions[46] have a reduced elastic modulus compared to benign cells. We also confirm the effect of pharmacological perturbation of the cytoskeleton by treatment of malignant MDA-MB-231 cells with 0.1 μM paclitaxel, which results in a reduction of % filtrate to 39.3 ± 10.3% compared to vehicle control of 66.4 ± 3.2% ($p = 1.4 \times 10^{-3}$) (**Fig 4D**); this is in line with the effect of paclitaxel on filtration of OVCAR5 Cis-R and Cis-S cells. We verify that the observed reduction in filtrate is not due to the effect of paclitaxel on the size of MDA-MB-231 cells, indicating that differential filtration of paclitaxel-treated cells reflects changes in cell deformability (**Supp Fig 2H)**.

We additionally filter weakly metastatic prostate cancer (DU145) cells in parallel with highly metastatic cells that we generated by knockdown of the nuclear envelope protein, emerin (DU145 Emerin KD)[77]. As these prostate cancer cells have a similar size distribution as the other cell types (**Supp Fig 2A, D, I**), we also tested the same filtration settings as for the ovarian cancer cells. We find that the highly metastatic cells with emerin KD have increased % filtrate (61.1 ± 13.9%) compared to the untransformed, weakly metastatic cells (17.0 ± 11.1%) ($p_{DU145\ Emerin\ KD}$=

1.4 x 10^{-6}) (**Fig 4E**). These observations using HTF are consistent with previous findings of altered nuclear mechanical stability with reduced levels of emerin[78,79], including our previous study using the prototype PMF device[77]. Notably, downregulation of emerin promotes malignant transformation of cancer cells[77]. Taken together, these observations confirm the application of HTF for screening cells that derive from distinct tissues.

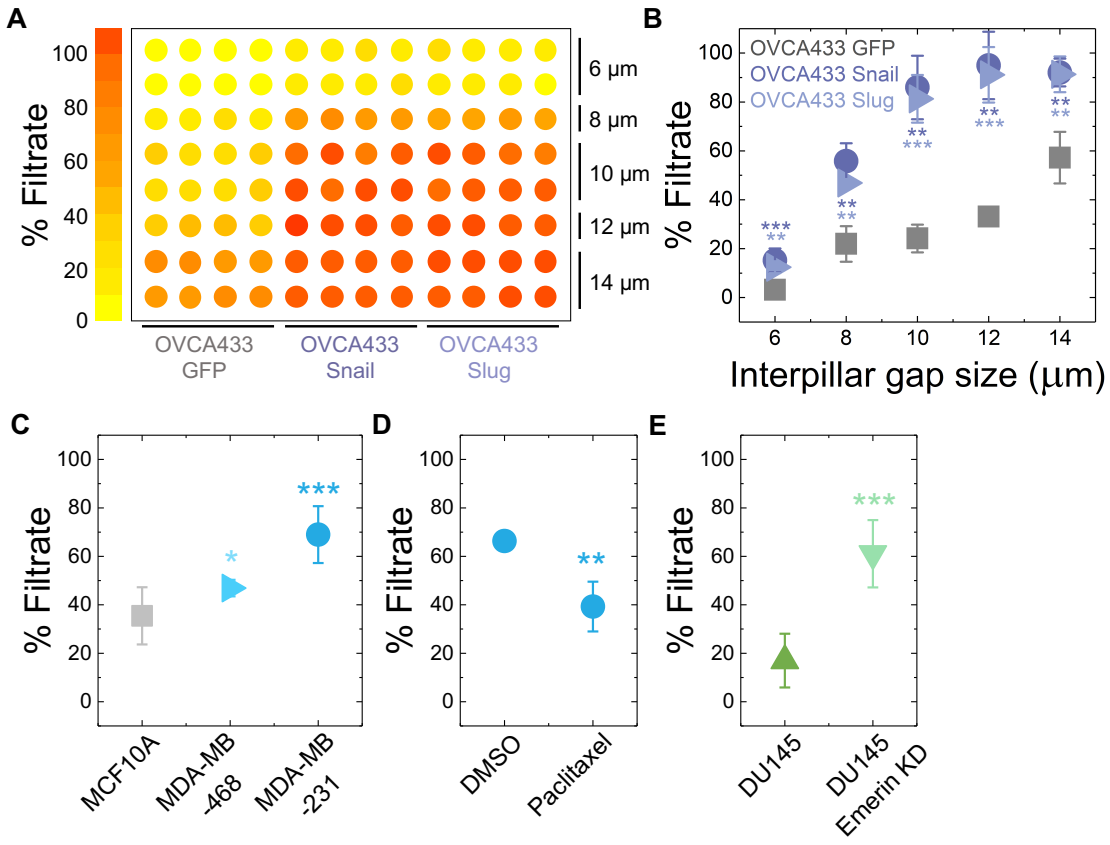

Figure 4. Using HTF to distinguish cell types. (A) Heat map of % filtrate for epithelial- (GFP) *versus* mesenchymal-type (Snail, Slug) human ovarian cancer (OVCA433) cells with different interpillar gap sizes in parallel. (B) % Filtrate *versus* gap size for OVCA433 cells. (C) Differential filtration of human breast cancer cells (MDA-MB-468, MDA-MB-231) and normal breast epithelial (MCF10A) cells. (D) MDA-MB-231 cells treated with 0.1 µM of paclitaxel for 24 h prior to filtration. (E) Differential filtration of human prostate cancer cells that are weakly metastatic (DU145) and transformed by knockdown[77] of emerin to be highly metastatic (DU145 Emerin KD). Filtration through 10 µm gaps at 28 kPa, 60 s, and 0.5 x 10^6 cells/mL for all cell types. Data points represent mean ± SD from three independent experiments and statistical significance is determined using student's t-test. *** $p < 0.001$; ** $p < 0.01$; * $p < 0.05$.

Cell filtration is sensitive to cytoskeletal and nuclear perturbations

To establish the role of molecular mediators of cellular deformability in regulating filtration, we treat the EMT panel of human ovarian cancer (OVCA433 GFP, OVCA433 Snail, and OVCA433 Slug) cells with compounds that are well established to alter cell and nuclear mechanical properties and/or mechanosignaling pathways (**Fig 5**). Such pharmacological perturbations are commonly used to validate that a new mechanotyping technology is sensitive to changes in cell physical properties[28,50,80]. To perturb the cytoskeleton, we treat cells with compounds to inhibit actin polymerization (cytochalasin D), activate actin polymerization (colchicine), stabilize microtubules (paclitaxel), and inhibit myosin II activity (blebbistatin). We also treat cells with additional compounds that are known to alter cell mechanotype through signaling pathways that result in cytoskeletal changes including inhibitors of transforming growth factor (TGF)-β (SB43154) and the yes-associated-protein (YAP) transcription factor (verteporfin), which is implicated in cellular mechanosensing at the scale of tissues and organs[81,82]. To further investigate the effects of nuclear physical properties on cell filtration, we treat cells with the histone deacetylase inhibitor (trichostatin-A), which is established to make cell nuclei more deformable[83].

Using the filtration conditions established to maximize the difference in filtrate volume between the epithelial- and mesenchymal-type cells, the OVCA433 Snail and Slug mesenchymal-type cells exhibit 77.3 ± 5.8% and 80.2 ± 8.0% filtrate whereas the reference filtrate for DMSO treated OVCA433 GFP control, epithelial-type cells is 22.6 ± 4.4%. In a screen including these three cell types, it is thus possible to identify compounds that increase filtrate volume for the epithelial-type OVCA433 GFP cells and decrease filtrate of the mesenchymal-type OVCA433 cells overexpressing Snail and Slug cells, which have reference filtrates of 77.3% and 80.2% that are close to the upper limit of ~88% filtrate.

As shown in **Fig 5**, we find that cytoskeletal-perturbing drugs consistently alter cell filtration. We first investigate actin, which is a major component of the cytoskeleton; the organization and levels of filamentous[84] actin are key determinants of cell deformability[28,40]. To

inhibit polymerization of F-actin, we treat cells with cytochalasin D[85]; this results in a significant increase in % filtrate for the OVCA433 GFP cells to 81.6 ± 8.7% ($p = 4.4 \times 10^{-4}$), which is consistent with observations that inhibiting actin polymerization makes cells more deformable[86,87]. We also observe slight increases in filtrate for OVCA433 Slug to 86.7 ± 3.6% ($p = 5.7 \times 10^{-2}$) and OVCA433 Snail cells to 85.3 ± 6.6% ($p = 8.3 \times 10^{-2}$); the reduced effects of cytochalasin D treatment on the filtration of mesenchymal-type cells reflect the initial filtrates near the upper limit of 77.3% and 80.2% for OVCA433 Snail and Slug cells, which precludes measurements of larger increases in filtrate. By contrast, activating polymerization of F-actin with 10 μM colchicine[88] induces a significant decrease in filtrate of mesenchymal-type cells to 37.2 ± 2.9% for Snail and 39.4 ± 3.7% to Slug cells ($p_{Snail} = 1.5 \times 10^{-3}$, $p_{Slug} = 1.7 \times 10^{-3}$); these observations are aligned with previous findings of decreased cell deformability with this concentration of drug[28,35,89]. As the reference filtrate of OVCA433 GFP cells is 19.7 ± 3.3%, we do not detect any further significant reduction in filtration of these cells with colchicine treatment (**Fig 5**). Together these findings confirm the effects of actin cytoskeleton organization on filtration volume, which further validates HTF as a method to detect differences in cell deformability.

Another major cytoskeletal component is microtubules. To stabilize microtubules, we treat cells with paclitaxel[35,90]. Following this treatment, we observe significant reductions in % filtrate for OVCA433 EMT-transformed cells to 15.3 ± 6.6% and 17.5 ± 5.8% ($p_{Snail} = 1.5 \times 10^{-4}$, $p_{Slug} = 2.9 \times 10^{-4}$), compared to vehicle treatment. We also find a smaller but significant decrease in filtrate of the OVCA433 GFP cells to 9.5 ± 2.9%, ($p = 0.13 \times 10^{-2}$), which is expected as the initial filtrate for these cells is already approaching the lower end of the dynamic range. These findings are aligned with previous results that paclitaxel decreases cellular deformability[28,34,35].

Nonmuscle myosin II (NMII) is an important determinant of cell mechanotype as this protein crosslinks actin filaments and is implicated in generating physical forces that contribute to intracellular tension[91-93]. To determine the effects of NMII activity on filtration, we treat cells with the NMII inhibitor blebbistatin. We observe a slight increase in % filtrate for OVCA433 Snail to

86.0 ± 2.2% (p_{Snail} = 7.2 x 10^{-2}) and OVCA433 Slug to 84.5 ± 2.9% (p_{Slug} = 8.6 x 10^{-2}), indicating decreased cell deformability; these findings are consistent with previous reports that inhibiting NMII activity for cells in a suspended state causes them to be stiffer[91], which may be explained by the reduction in myosin-mediated actin disassembly and remodeling[94]. There is no significant decrease in filtration of OVCA433 GFP cells with inhibition of NMII activity (p = 7.3 x 10^{-2}), suggesting that NMII activity may play a different role in regulating the mechanotype of epithelial-type cells.

Two other pathways that regulate actin organization are mediated through TGF-β[95,96] and YAP[97,98]. Activation of TGF-β promotes actin stress fiber formation[95,99] and EMT[100,101]. However, we find no significant changes in % filtrate of epithelial- and mesenchymal-type OVCA433 cells with the TGF-β inhibitor SB431542, indicating that inhibiting endogenous TGF-β activity does not affect cell filtration. These findings contrast previous studies that report increased cell deformability with activation of TGF-β[102,103]; however, in those studies, cells were grown in the presence of TGF-β supplementation, whereas we assess here effects of the inhibitor without additional activation of TGF-β. To investigate the role of YAP activity, we treat cells with the YAP inhibitor, verteporfin. Loss of YAP activity leads to stabilization of actin filaments *via* RhoA GTPase[97,98]. We find that verteporfin treatment reduces the filtration of mesenchymal-type cells to 66.3 ± 1.5% for OVCA433 Snail (p_{Snail} = 6.2 x 10^{-2}) and to 63.4 ± 4.4% for OVCA433 Slug (p_{Slug} = 2.2 x 10^{-2}), which is consistent with a reduction in cell deformability due to YAP inhibition. We find no significant change in filtration for OVCA433 GFP with verteporfin (p = 9.8 x 10^{-1}), which is likely due to the lower limit of the dynamic range. While verteporfin may have additional off target effects[104,105], these observations are consistent with previous reports that loss of YAP activity results in cell stiffening through increased F-actin[97,98].

We next investigate the effect of nuclear perturbation on cell filtration. The nucleus is typically the stiffest and largest organelle, which rate-limits the deformation of cells through narrow gaps[106,107]. To determine effects of nuclear structure on cell filtration, we treat cells with the histone

deacetylase (HDAC) inhibitor, trichostatin A, which causes chromatin decondensation[108,109]. Treatment of cells with trichostatin A leads to increased % filtrate across both epithelial- and mesenchymal-type cells compared to vehicle control (p_{Snail} = 9.1 x 10^{-2}, p_{Slug} = 7.2 x 10^{-2}, p_{GFP} = 3.7 x 10^{-4}), indicating that the structural organization of the nucleus contributes to cell filtration (**Fig 5**). These findings are consistent with a previous report showing enhanced deformability of cell nuclei in intact cells with trichostatin A treatment[83]. Taken together, filtration of cells treated with this panel of compounds indicates that HTF is sensitive to perturbations of cytoskeletal and nuclear components.

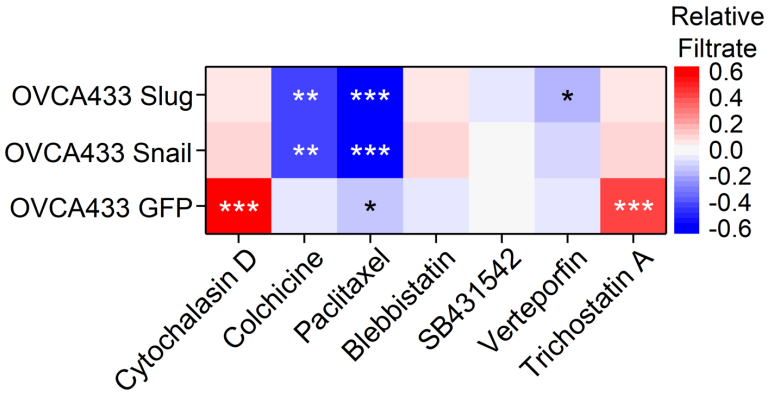

Figure 5. Effects of pharmacologic perturbations to cytoskeleton and nucleus on filtration. Treatment of OVCA433 (GFP, Snail, Slug) cells with a panel of drugs: actin polymerization inhibitor (cytochalasin D), actin polymerization activator (colchicine), microtubule stabilizer (paclitaxel), myosin II activity inhibitor (blebbistatin), TGF-β inhibitor (SB431542), YAP inhibitor (verteporfin), and HDAC inhibitor (trichostatin A). All treatments at 10 μM for 24 h prior to filtration. Color represents filtrate relative to the DMSO treated cells. Filtration through 10 μm gap size at 28 kPa for 60 s, and 0.5 x 10^6 cells/mL. Statistical significance compared to the DMSO treated control is determined using student's t-test. *** $p < 0.001$; ** $p < 0.01$; * $p < 0.05$.

To assess the quality of the HTF assay, we first characterize the variability in % filtrate measurements. The variability in % filtrate of media without any cells filtered through HTF device arrays is indicated by the SD of ± 6.6% with gap size of 10 μm, for 20 s at 28 kPa (**Supp Fig 3A**). For filtration of human ovarian cancer (OVCA433) cells we observe a SD of ± 10.6% in % filtrate across device arrays with a confidence interval of -0.6 to 20.4% using filtration conditions of 10 μm gap size, 28 kPa for 60 s and 0.5 x 10^6 cells/mL (**Supp Fig 3B**).

To further assess the quality of the HTF assay for a higher throughput screen, we use the filtration results across the panel of cytoskeletal and nuclear perturbing compounds (**Fig 5**): this enables us to evaluate the *Z'*-factor, which provides a metric for evaluating the statistical robustness of filtration measurements based on the difference in maximum and minimum readouts[110]. The *Z'*-factor reflects the dynamic range of HTF measurements and also accounts for data variation as it is determined by the mean and standard deviation of drug treated samples with maximum (μ_{c+} ,σ_{c+}) and minimum (μ_{c-} ,σ_{c-}) filtrates for each cell type,

$$Z' = 1 - \frac{(3\sigma_{max} + 3\sigma_{min})}{|\mu_{max} - \mu_{min}|}.$$

A value of *Z'* > 0.5 is an indication of high assay quality. As proof-of-concept, we use data of OVCA433 GFP cells treated with cytochalasin D that exhibits maximum filtrate and with paclitaxel that results in the minimum filtrate. Each of these compounds are established to increase and decrease cellular deformability, respectively[28]; the resultant *Z'* = 0.61 for the OVCA433 GFP cells. We also determine *Z'* values of 0.63 for OVCA433 Snail and 0.61 OVCA433 Slug cells, reflecting the good quality of the HTF assay. While the *Z'*-factor provides a metric to evaluate assay quality without intervention of test compounds, we further assess the suitability of HTF for a higher throughput screen to identify hit compounds that modulate cell deformability by evaluating the *Z*-factor[110],

$$Z = 1 - \frac{(3\sigma_s + 3\sigma_c)}{|\mu_s - \mu_c|},$$

where μ_s, σ_s are the sample mean and standard deviation, and μ_c, σ_c are the control mean/standard deviation. For an ideal HT assay, *Z* = 1, while 0.5 < *Z* < 1 indicates an excellent assay with greater likelihood of identifying statistically robust hits; by contrast, *Z* < 0 indicates that the screen will not yield any meaningful results. Envisioning a screen to identify hits that cause mesenchymal-type cells to become less invasive, and thereby less deformable, we consider the untreated cells as the control and the paclitaxel-treated cells as the sample; this yields *Z* = 0.34

to 0.40. For a screen to identify hits that cause OVCA433 GFP epithelial-type cells to become more deformable, we consider untreated OVCA433 GFP as the control and cytochalasin D-treated cells as the sample, which yields $Z = 0.34$. While these are relatively low Z-factors for a high quality HT screen, values of Z' and $Z > 0$ indicate that the assay is functional and further optimization is needed to successfully configure HTF for a particular HT screen[110].

One strategy to improve the Z-factor is to reduce filtrate variability between devices; this could be achieved by optimizing device geometry to minimize the presence of air bubbles or other factors that cause variability in flow during filtration. Another strategy to increase the Z-factor is to reduce the dead volume of the HTF setup. This sets the upper limit of measurable filtrate volume and thus dynamic range of HTF measurements. Into the future, injection molding[111] or micromachining[56,112] may enable more consistent fabrication of filtration devices that also eliminate the need for separate components such as loading and outlet plates. Additional future analysis is required to precisely define how sensitive HTF is to small changes in cell elastic modulus by filtration of calibration particles or cells treated with a compound that results in known changes in cell stiffness; in this way, the sensitivity of filtration volume to changes in elastic modulus could be precisely quantified.

As with all HT-screening methods, the power of HTF lies in the ability to rapidly screen samples using a readout that is quick, user-friendly, and inexpensive to obtain. Top 'hit' compounds can be identified based on their ability to induce the largest changes in filtrate volume. We show here that filtration is modulated by cell deformability. However, other factors, such as cell size, cell cycle stage, cell-cell clustering, and density of the cell suspension, also regulate filtration. Validation of top hits in greater detail using secondary orthogonal assays can be used to select hits for the desired trait(s) that impact filtration.

With the challenges in identifying effective treatment strategies for cancer, cell filtration provides an elegant way to screen cells in a way that complements specific molecular biomarkers,

such as E-cadherin and vimentin for EMT-status[113], EpCAM and MUC-1 for cancer stem cells[114], or Ki67 for cell proliferation[115]. We show here that filtration is sensitive to the altered deformability of chemoresistant cancer cells as well as epithelial- *versus* mesenchymal-type cancer cells, which have distinct mechanical properties[73]. Cancer cell deformability shows strong associations with invasion in many contexts[29,40,76,116], and may have functional consequences in metastasis where cells are required to undergo large deformations[25,107]. Molecular mediators that regulate mechanotype also generate forces required for cell movement and shape changes[117]. Thus, HTF could be a complementary tool for drug discovery that harnesses cell deformability as a surrogate phenotype to rapidly evaluate the effects of drugs or novel genes to inhibit invasion. HTF could also be used to address basic research questions through a CRISPR/Cas9 or shRNA screen to define molecular mediators of cell deformability. While we envision HTF is amenable to screening established cell lines and/or patient-derived cells, future efforts to scale down the device volume could enable testing of primary patient samples. A distinct advantage of HTF is that the assay requires minutes to assess cell deformability using filtration; by contrast, existing methods that screen based on cell invasion, motility, or even proliferation, require 10-100 hours per assay[12,13,118]. While HTF offers these unique advantages, complementary assays to measure other factors that may contribute to cell invasion/migration, such as adhesion[119] and cell-cell interactions[120,121], could be used to identify synergistic treatments. Future work will define the extent to which HTF may identify novel hits in the HT screening space relative to existing methods.

Conclusion

Here we describe the HTF method, which provides a scalable platform for simultaneous measurements of cell filtration. We show that HTF captures differences in the filtration of different cell types, including malignant *versus* benign, cisplatin-resistant *versus* cisplatin-sensitive cells, epithelial-type *versus* mesenchymal-type cells, as well as the effects of small molecules that alter the cytoskeleton and nucleus. As HTF evaluates the ability of single cells to passively deform

through narrow gaps on the timescale of seconds to minutes, the method offers unique advantages that complement existing cell invasion assays which measure the ability of cells to actively migrate through narrow geometries[122-124]. Importantly, HTF bridges the gap in throughput between measurements of cell deformability and HT screening, which opens up opportunities to uncover novel molecules or pathways that regulate cell deformability. While we have demonstrated here the application of cell filtration to screen cancer cells, changes in cell physical properties are implicated in a range of diseases from blood disorders[125] to neurodegenerative diseases such as Alzheimer's[126]. Cell filtration thus has potential to be used as a scalable readout for drug discovery in diverse disease contexts.

Supplementary Figures

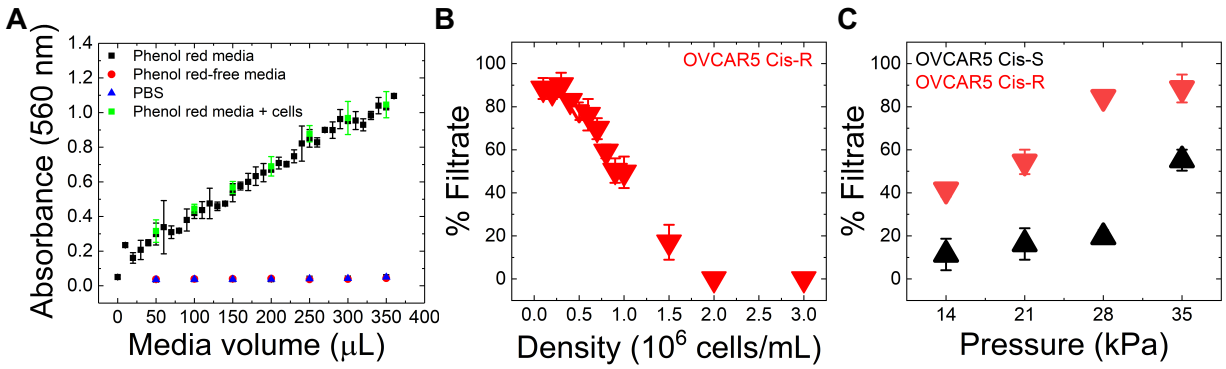

Supplementary Figure 1. Optimization of HT filtration for sensitive- *versus* resistant-human ovarian cancer (OVCAR5) cells. (A) Absorbance measurements at 560 nm as a function of cell medium volume yields a standard curve. Measurements of cell suspension in phenol red containing media obtained for OVCAR5-CisR cells at 0.5 x 10^6 cells/mL. Below media volumes of ~25 µL, reliable absorbance measurements in a 96-well plate format cannot be obtained, which thus sets the lower limit for filtrate to be ~7% of the initial volume loaded. % Filtrate is determined by volume of filtrate relative to initial volume of a suspension of human ovarian cancer (OVCAR5) cells on: (B) Density of cell suspension. OVCAR5 Cis-R cells are filtered through a device with gap size of 10 µm at 28 kPa over 90 s. Cell density is measured to be within ± 0.04 x 10^6 cells/mL, which is smaller than the symbols. (C) Driving pressure to filter the OVCAR5 Cis-S and Cis-R cell suspension , 0.5 x 10^6 cells/mL, through a device with interpillar gap size of 10 µm over 90 s. Driving pressure is measured to be within ± 0.14 kPa, which is smaller than the symbols. Each data point represents mean ± SD from three independent experiments.

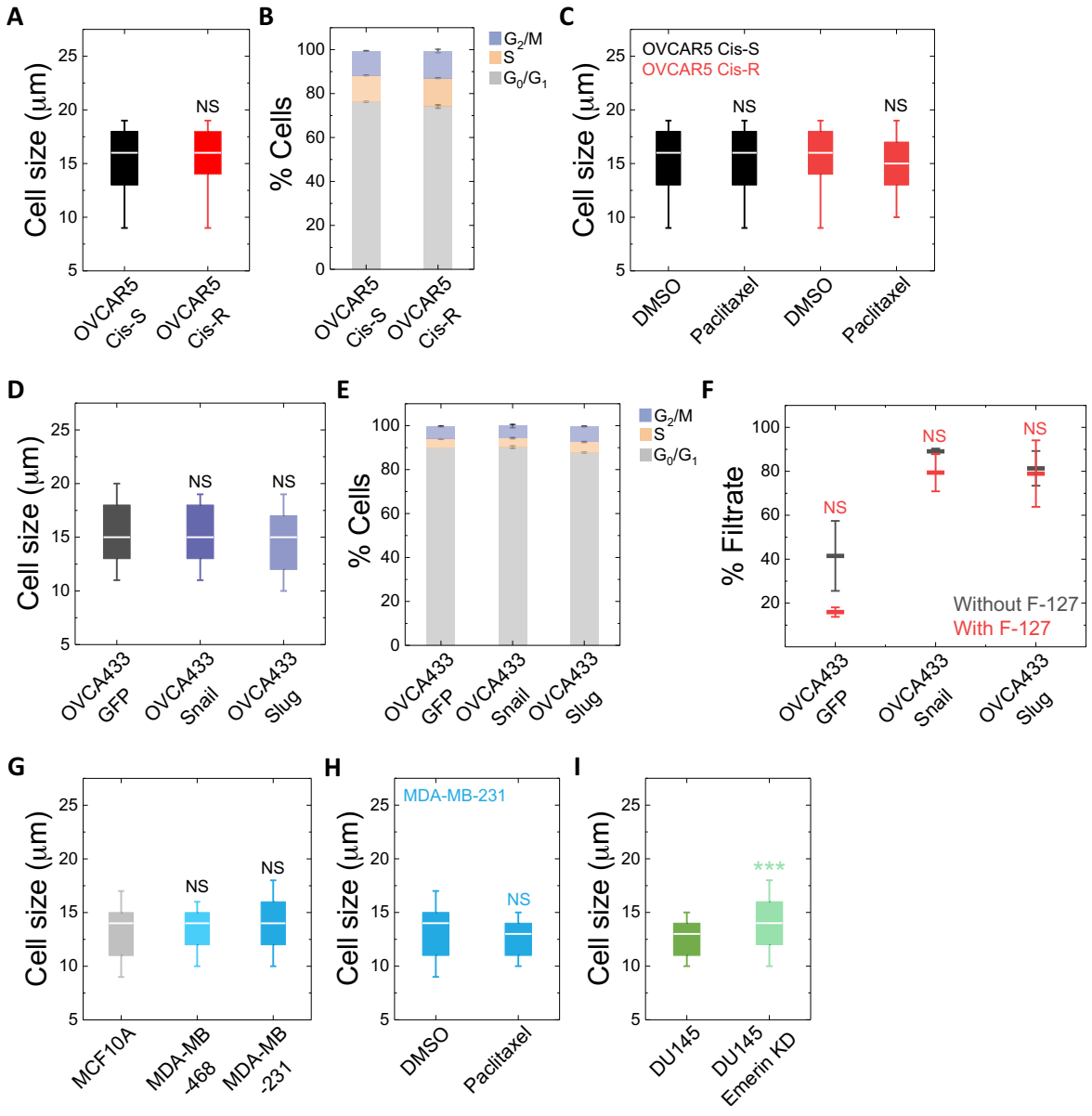

Supplementary Figure 2. Characterization of cell size, cell cycle distribution, and effect of treatment with surfactant (pluronics F-127) on filtration. (A) Cell size data for human ovarian cancer OVCAR5 Cis-S and Cis-R cells. (B) Difference in cell cycle distribution of OVCAR5 Cis-S and Cis-R cells is statistically not significant. (C) Cell size data for OVCAR5 Cis-S and Cis-R cells treated with 0.1 μM paclitaxel for 24 h prior to size measurements. (D) Cell size data for OVCAR433 GFP, Snail and Slug cells. (E) Difference in cell cycle distribution of OVCAR433 GFP, Snail and Slug cells is statistically not significant. (F) Treatment with surfactant (pluronics F-127) does not have a significant effect on filtration of ovarian cancer (OVCA433) cells. Differential filtration of OVCA433 GFP, Snail and Slug cell suspensions with added pluronics F-127 at 0.01% w/v through 10 μm gaps at 28 kPa, 60 s, and 0.5 x 10^6 cells/mL Each data point represents mean

± SD from two independent experiments. Cell size data for human breast cancer (G) MCF10A, MDA-MB-468 and MDA-MB-231 cells, (H) MDA-MB-231 cells treated with 0.1 μM paclitaxel for 24 h prior to size measurements, and human prostate cancer (I) DU145 and DU145 Emerin KD cells. Cell size box plots show the 25th and 75th percentiles of cell size measurements, whiskers denote 10th and 90th percentiles and line is the median cell size. N > 400 cells over three independent experiments. Statistical significance determined using Mann Whitney U test. Cell cycle data sets represent mean ± SD from two independent experiments. Statistical significance determined using student's t-test. *** $p < 0.001$; ** $p < 0.01$; * $p < 0.05$.

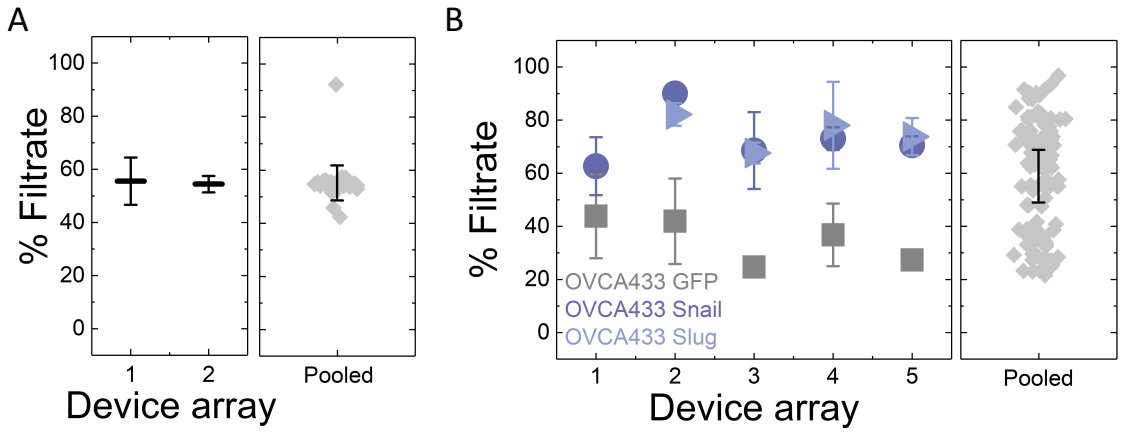

Supplementary Figure 3. Quantification of variability in filtration measurements. (A) Filtration of media without cells through HTF device arrays with gap size of 10 μm at 38 kPa for 20 s. Shown here is data from two device arrays. Pooled data indicates the pooled SD in measurements. (B) Differential filtration of OVCA433 GFP, Snail and Slug cells using five different PDMS device arrays with interpillar gap size of 10 μm at 28 kPa for 60 s and 0.5 x 10^6 cells/mL. Each data point represents mean ± SD. Pooled data indicates the pooled SD in measurements of % filtrate using HTF.

References

1. W. F. An and N. Tolliday, *Mol Biotechnol*, 2010, **45**, 180-186.
2. J. T. Fox and K. Myung, *Oncotarget*, 2012, **3**, 581-585.
3. P. Szymanski, M. Markowicz and E. Mikiciuk-Olasik, *Int J Mol Sci*, 2012, **13**, 427-452.
4. G. S. Du, J. Z. Pan, S. P. Zhao, Y. Zhu, J. M. den Toonder and Q. Fang, *Anal Chem*, 2013, **85**, 6740-6747.
5. K. Guo, A. A. Shelat, R. K. Guy and M. B. Kastan, *J Biomol Screen*, 2014, **19**, 538-546.

6. T. Miyagi, B. Shiotani, R. Miyoshi, T. Yamamoto, T. Oka, K. Umezawa, T. Ochiya, M. Takano and H. Tahara, *Cancer Sci*, 2014, **105**, 870-874.

7. A. M. Baker, W. Huang, X. M. Wang, M. Jansen, X. J. Ma, J. Kim, C. M. Anderson, X. Wu, L. Pan, N. Su, Y. Luo, E. Domingo, T. Heide, A. Sottoriva, A. Lewis, A. D. Beggs, N. A. Wright, M. Rodriguez-Justo, E. Park, I. Tomlinson and T. A. Graham, *Nat Commun*, 2017, **8**, 1998.

8. H. L. Martin, M. Adams, J. Higgins, J. Bond, E. E. Morrison, S. M. Bell, S. Warriner, A. Nelson and D. C. Tomlinson, *PLoS One*, 2014, **9**, e88338.

9. A. H. Wong, H. Li, Y. Jia, P. I. Mak, R. Martins, Y. Liu, C. M. Vong, H. C. Wong, P. K. Wong, H. Wang, H. Sun and C. X. Deng, *Sci Rep*, 2017, **7**, 9109.

10. L. Zhang, Z. Yang, L. Granieri, A. Pasculescu, A. Datti, S. L. Asa, Z. Xu and S. Ezzat, *Oncotarget*, 2016, **7**, 19948-19959.

11. O. S. Frankfurt and A. Krishan, *Anticancer Drugs*, 2003, **14**, 555-561.

12. N. A. Evensen, J. Li, J. Yang, X. Yu, N. S. Sampson, S. Zucker and J. Cao, *PLoS One*, 2013, **8**, e82811.

13. H. A. Kenny, M. Lal-Nag, E. A. White, M. Shen, C. Y. Chiang, A. K. Mitra, Y. Zhang, M. Curtis, E. M. Schryver, S. Bettis, A. Jadhav, M. B. Boxer, Z. Li, M. Ferrer and E. Lengyel, *Nat Commun*, 2015, **6**, 6220.

14. G. Cassinelli, *Tumori*, 2016, **2016**, 226-235.

15. G. W. Aherne, E. McDonald and P. Workman, *Breast Cancer Res*, 2002, **4**, 148-154.

16. R. C. Donehower, *Stem Cells*, 1996, **14**, 25-28.

17. J. K. Chan, M. K. Cheung, A. Husain, N. N. Teng, D. West, A. S. Whittemore, J. S. Berek and K. Osann, *Obstet Gynecol*, 2006, **108**, 521-528.

18. J. D. Wright, L. Chen, A. I. Tergas, S. Patankar, W. M. Burke, J. Y. Hou, A. I. Neugut, C. V. Ananth and D. L. Hershman, *Obstet Gynecol*, 2015, **125**, 1345-1352.

19. T. Shimada, T. Saito, M. Shimokawa, K. Shimamoto, S. Matsushita, S. Yamaguchi, K. Ariyoshi and M. Okadome, *Jpn J Clin Oncol*, 2017, **47**, 494-498.

20. A. Kim, Y. Ueda, T. Naka and T. Enomoto, *J Exp Clin Cancer Res*, 2012, **31**, 14.

21. J. Y. Lee, S. Kim, Y. T. Kim, M. C. Lim, B. Lee, K. W. Jung, J. W. Kim, S. Y. Park and Y. J. Won, *BMC Cancer*, 2018, **18**, 601.

22. C. N. Qian, Y. Mei and J. Zhang, *Chin J Cancer*, 2017, **36**, 38.

23. H. Zahreddine and K. L. Borden, *Front Pharmacol*, 2013, **4**, 28.

24. T. R. Wilson, P. G. Johnston and D. B. Longley, *Curr Cancer Drug Targets*, 2009, **9**, 307-319.

25. D. Wirtz, K. Konstantopoulos and P. C. Searson, *Nat Rev Cancer*, 2011, **11**, 512-522.

26. S. M. Fendt, *Front Endocrinol (Lausanne)*, 2017, **8**, 150.

27. A. Fuhrmann, A. Banisadr, P. Beri, T. D. Tlsty and A. J. Engler, *Biophys J*, 2017, **112**, 736-745.

28. D. Qi, N. Kaur Gill, C. Santiskulvong, J. Sifuentes, O. Dorigo, J. Rao, B. Taylor-Harding, W. Ruprecht Wiedemeyer and A. C. Rowat, *Sci Rep*, 2015, **5**, 17595.

29. K. D. Nyberg, S. L. Bruce, A. V. Nguyen, C. K. Chan, N. K. Gill, T. H. Kim, E. K. Sloan and A. C. Rowat, *Integr Biol (Camb)*, 2018, **10**, 218-231.

30. J. Hamann and M. Overholtzer, *Cell Res*, 2016, **26**, 637-638.

31. H. T. Tse, D. R. Gossett, Y. S. Moon, M. Masaeli, M. Sohsman, Y. Ying, K. Mislick, R. P. Adams, J. Rao and D. Di Carlo, *Sci Transl Med*, 2013, **5**, 212ra163.

32. W. A. Lam, M. J. Rosenbluth and D. A. Fletcher, *Blood*, 2007, **109**, 3505-3508.

33. S. E. Cross, Y. S. Jin, Q. Y. Lu, J. Rao and J. K. Gimzewski, *Nanotechnology*, 2011, **22**, 215101.

34. A. El Kaffas, D. Bekah, M. Rui, J. C. Kumaradas and M. C. Kolios, *Phys Med Biol*, 2013, **58**, 923-936.

35. M. A. Tsai, R. E. Waugh and P. C. Keng, *Biophys J*, 1998, **74**, 3282-3291.

36. S. Sharma, C. Santiskulvong, J. Rao, J. K. Gimzewski and O. Dorigo, *Integr Biol (Camb)*, 2014, **6**, 611-617.

37. M. Morgan-Fisher, U. M. Wewer and A. Yoneda, *J Histochem Cytochem*, 2013, **61**, 185-198.

38. A. Surcel, W. P. Ng, H. West-Foyle, Q. Zhu, Y. Ren, L. B. Avery, A. K. Krenc, D. J. Meyers, R. S. Rock, R. A. Anders, C. L. Freel Meyers and D. N. Robinson, *Proc Natl Acad Sci U S A*, 2015, **112**, 1428-1433.

39. A. Gandalovicova, D. Rosel, M. Fernandes, P. Vesely, P. Heneberg, V. Cermak, L. Petruzelka, S. Kumar, V. Sanz-Moreno and J. Brabek, *Trends Cancer*, 2017, **3**, 391-406.

40. W. Xu, R. Mezencev, B. Kim, L. Wang, J. McDonald and T. Sulchek, *PLoS One*, 2012, **7**, e46609.

41. T. H. Kim, N. K. Gill, K. D. Nyberg, A. V. Nguyen, S. V. Hohlbauch, N. A. Geisse, C. J. Nowell, E. K. Sloan and A. C. Rowat, *J Cell Sci*, 2016, **129**, 4563-4575.

42. A. V. Nguyen, K. D. Nyberg, M. B. Scott, A. M. Welsh, A. H. Nguyen, N. Wu, S. V. Hohlbauch, N. A. Geisse, E. A. Gibb, A. G. Robertson, T. R. Donahue and A. C. Rowat, *Integr Biol (Camb)*, 2016, **8**, 1232-1245.

43. H. Son and A. Moon, *Toxicol Res*, 2010, **26**, 245-252.

44. R. M. Hochmuth and D. Needham, *Biorheology*, 1990, **27**, 817-828.

45. O. Thoumine and A. Ott, *J Cell Sci*, 1997, **110 (Pt 17)**, 2109-2116.

46. S. E. Cross, Y. S. Jin, J. Rao and J. K. Gimzewski, *Nat Nanotechnol*, 2007, **2**, 780-783.

47. M. J. Rosenbluth, W. A. Lam and D. A. Fletcher, *Biophys J*, 2006, **90**, 2994-3003.

48. O. Otto, P. Rosendahl, A. Mietke, S. Golfier, C. Herold, D. Klaue, S. Girardo, S. Pagliara, A. Ekpenyong, A. Jacobi, M. Wobus, N. Topfner, U. F. Keyser, J. Mansfeld, E. Fischer-Friedrich and J. Guck, *Nat Methods*, 2015, **12**, 199-202, 194 p following 202.

49. A. Adamo, A. Sharei, L. Adamo, B. Lee, S. Mao and K. F. Jensen, *Anal Chem*, 2012, **84**, 6438-6443.

50. D. R. Gossett, H. T. Tse, S. A. Lee, Y. Ying, A. G. Lindgren, O. O. Yang, J. Rao, A. T. Clark and D. Di Carlo, *Proc Natl Acad Sci U S A*, 2012, **109**, 7630-7635.

51. N. K. Gill, D. Qi, T.-H. Kim, C. Chan, A. Nguyen, K. D. Nyberg and A. C. Rowat, 2017.

52. O. K. Baskurt, D. Gelmont and H. J. Meiselman, *Am J Respir Crit Care Med*, 1998, **157**, 421-427.

53. Y. Kikuchi, T. Arai and T. Koyama, *Med Biol Eng Comput*, 1983, **21**, 270-276.

54. H. L. Reid, A. J. Barnes, P. J. Lock, J. A. Dormandy and T. L. Dormandy, *J Clin Pathol*, 1976, **29**, 855-858.

55. J. S. Marcus, W. F. Anderson and S. R. Quake, *Anal Chem*, 2006, **78**, 956-958.

56. M. Muluneh and D. Issadore, *Lab Chip*, 2013, **13**, 4750-4754.

57. W. Y. Ma, L. C. Hsiung, C. H. Wang, C. L. Chiang, C. H. Lin, C. S. Huang and A. M. Wo, *Sci Rep*, 2015, **5**, 9656.

58. G. Du, Q. Fang and J. M. den Toonder, *Anal Chim Acta*, 2016, **903**, 36-50.

59. S. Vyawahare, A. D. Griffiths and C. A. Merten, *Chem Biol*, 2010, **17**, 1052-1065.

60. K. D. Nyberg, K. H. Hu, S. H. Kleinman, D. B. Khismatullin, M. J. Butte and A. C. Rowat, *Biophys J*, 2017, **113**, 1574-1584.

61. Y. J. Fu, H. Z. Qui, K. S. Liao, S. J. Lue, C. C. Hu, K. R. Lee and J. Y. Lai, *Langmuir*, 2010, **26**, 4392-4399.

62. K. D. Nyberg, M. B. Scott, S. L. Bruce, A. B. Gopinath, D. Bikos, T. G. Mason, J. W. Kim, H. S. Choi and A. C. Rowat, *Lab Chip*, 2016, **16**, 3330-3339.

63. R. S. Frank and M. A. Tsai, *J Biomech Eng*, 1990, **112**, 277-282.

64. S. Byun, S. Son, D. Amodei, N. Cermak, J. Shaw, J. H. Kang, V. C. Hecht, M. M. Winslow, T. Jacks, P. Mallick and S. R. Manalis, *Proc Natl Acad Sci U S A*, 2013, **110**, 7580-7585.

65. M. J. Rosenbluth, W. A. Lam and D. A. Fletcher, *Lab Chip*, 2008, **8**, 1062-1070.

66. D. J. Hoelzle, B. A. Varghese, C. K. Chan and A. C. Rowat, *J Vis Exp*, 2014, DOI: 10.3791/51474, e51474.

67. A. C. Rowat, D. E. Jaalouk, M. Zwerger, W. L. Ung, I. A. Eydelnant, D. E. Olins, A. L. Olins, H. Herrmann, D. A. Weitz and J. Lammerding, *J Biol Chem*, 2013, **288**, 8610-8618.

68. S. Gabriele, A. M. Benoliel, P. Bongrand and O. Theodoly, *Biophys J*, 2009, **96**, 4308-4318.

69. K. W. Oh, K. Lee, B. Ahn and E. P. Furlani, *Lab Chip*, 2012, **12**, 515-545.

70. D. C. Duffy, J. C. McDonald, O. J. Schueller and G. M. Whitesides, *Anal Chem*, 1998, **70**, 4974-4984.

71. B. M. Jun, F. Serra, Y. Xia, H. S. Kang and S. Yang, *ACS Appl Mater Interfaces*, 2016, **8**, 30671-30676.

72. P. Kunda, A. E. Pelling, T. Liu and B. Baum, *Curr Biol*, 2008, **18**, 91-101.

73. J. Shaw Bagnall, S. Byun, S. Begum, D. T. Miyamoto, V. C. Hecht, S. Maheswaran, S. L. Stott, M. Toner, R. O. Hynes and S. R. Manalis, *Sci Rep*, 2015, **5**, 18542.

74. K. J. Chavez, S. V. Garimella and S. Lipkowitz, *Breast Dis*, 2010, **32**, 35-48.

75. H. Babahosseini, J. S. Strobl and M. Agah, *Nanotechnology*, 2015, **26**, 354004.

76. V. Swaminathan, K. Mythreye, E. T. O'Brien, A. Berchuck, G. C. Blobe and R. Superfine, *Cancer Res*, 2011, **71**, 5075-5080.

77. M. Reis-Sobreiro, J. F. Chen, T. Novitskaya, S. You, S. Morley, K. Steadman, N. K. Gill, A. Eskaros, M. Rotinen, C. Y. Chu, L. W. K. Chung, H. Tanaka, W. Yang, B. S. Knudsen, H. R. Tseng, A. C. Rowat, E. M. Posadas, A. Zijlstra, D. Di Vizio and M. R. Freeman, *Cancer Res*, 2018, **78**, 6086-6097.

78. A. C. Rowat, J. Lammerding and J. H. Ipsen, *Biophys J*, 2006, **91**, 4649-4664.

79. J. Lammerding, J. Hsiao, P. C. Schulze, S. Kozlov, C. L. Stewart and R. T. Lee, *J Cell Biol*, 2005, **170**, 781-791.

80. J. R. Lange, J. Steinwachs, T. Kolb, L. A. Lautscham, I. Harder, G. Whyte and B. Fabry, *Biophys J*, 2015, **109**, 26-34.

81. S. Dupont, L. Morsut, M. Aragona, E. Enzo, S. Giulitti, M. Cordenonsi, F. Zanconato, J. Le Digabel, M. Forcato, S. Bicciato, N. Elvassore and S. Piccolo, *Nature*, 2011, **474**, 179-183.

82. B. Zhao, X. Ye, J. Yu, L. Li, W. Li, S. Li, J. Yu, J. D. Lin, C. Y. Wang, A. M. Chinnaiyan, Z. C. Lai and K. L. Guan, *Genes Dev*, 2008, **22**, 1962-1971.

83. K. J. Chalut, M. Hopfler, F. Lautenschlager, L. Boyde, C. J. Chan, A. Ekpenyong, A. Martinez-Arias and J. Guck, *Biophys J*, 2012, **103**, 2060-2070.

84. S. Graff-Iversen, S. A. Anderssen, I. M. Holme, A. K. Jenum and T. Raastad, *Eur J Epidemiol*, 2008, **23**, 167-174.

85. D. W. Goddette and C. Frieden, *J Biol Chem*, 1986, **261**, 15974-15980.

86. M. A. Tsai, R. S. Frank and R. E. Waugh, *Biophys J*, 1994, **66**, 2166-2172.

87. T. Wakatsuki, B. Schwab, N. C. Thompson and E. L. Elson, *J Cell Sci*, 2001, **114**, 1025-1036.

88. H. I. Jung, I. Shin, Y. M. Park, K. W. Kang and K. S. Ha, *Mol Cells*, 1997, **7**, 431-437.

89. S. Chien and K. L. Sung, *Biophys J*, 1984, **46**, 383-386.

90. I. Arnal and R. H. Wade, *Curr Biol*, 1995, **5**, 900-908.

91. C. J. Chan, A. E. Ekpenyong, S. Golfier, W. Li, K. J. Chalut, O. Otto, J. Elgeti, J. Guck and F. Lautenschlager, *Biophys J*, 2015, **108**, 1856-1869.

92. A. X. Cartagena-Rivera, J. S. Logue, C. M. Waterman and R. S. Chadwick, *Biophys J*, 2016, **110**, 2528-2539.

93. J. C. Martens and M. Radmacher, *Pflugers Arch*, 2008, **456**, 95-100.

94. L. Haviv, D. Gillo, F. Backouche and A. Bernheim-Groswasser, *J Mol Biol*, 2008, **375**, 325-330.

95. S. Boland, E. Boisvieux-Ulrich, O. Houcine, A. Baeza-Squiban, M. Pouchelet, D. Schoevaert and F. Marano, *J Cell Sci*, 1996, **109 (Pt 9)**, 2207-2219.

96. S. Edlund, M. Landstrom, C. H. Heldin and P. Aspenstrom, *Mol Biol Cell*, 2002, **13**, 902-914.

97. Y. Qiao, J. Chen, Y. B. Lim, M. L. Finch-Edmondson, V. P. Seshachalam, L. Qin, T. Jiang, B. C. Low, H. Singh, C. T. Lim and M. Sudol, *Cell Rep*, 2017, **19**, 1495-1502.

98. G. Nardone, J. Oliver-De La Cruz, J. Vrbsky, C. Martini, J. Pribyl, P. Skladal, M. Pesl, G. Caluori, S. Pagliari, F. Martino, Z. Maceckova, M. Hajduch, A. Sanz-Garcia, N. M. Pugno, G. B. Stokin and G. Forte, *Nat Commun*, 2017, **8**, 15321.

99. R. J. Pelham, Jr. and Y. Wang, *Proc Natl Acad Sci U S A*, 1997, **94**, 13661-13665.

100. J. L. Leight, M. A. Wozniak, S. Chen, M. L. Lynch and C. S. Chen, *Mol Biol Cell*, 2012, **23**, 781-791.

101. J. W. O'Connor and E. W. Gomez, *Clin Transl Med*, 2014, **3**, 23.

102. A. Kulkarni, A. Chatterjee, P. Kondaiah and N. Gundiah, *Phys Biol*, 2018, DOI: 10.1088/1478-3975/aac3ba.

103. Q. Zheng, J. Long, B. Jia, X. Xu, C. Zhang, L. Li, Z. Wen, F. Jin, W. Yao and Z. Zeng, *Clin Hemorheol Microcirc*, 2014, **56**, 25-40.

104. H. Zhang, S. K. Ramakrishnan, D. Triner, B. Centofanti, D. Maitra, B. Gyorffy, J. S. Sebolt-Leopold, M. K. Dame, J. Varani, D. E. Brenner, E. R. Fearon, M. B. Omary and Y. M. Shah, *Sci Signal*, 2015, **8**, ra98.

105. F. Gibault, M. Corvaisier, F. Bailly, G. Huet, P. Melnyk and P. Cotelle, *Curr Med Chem*, 2016, **23**, 1171-1184.

106. A. C. Rowat, J. Lammerding, H. Herrmann and U. Aebi, *Bioessays*, 2008, **30**, 226-236.

107. K. Wolf, M. Te Lindert, M. Krause, S. Alexander, J. Te Riet, A. L. Willis, R. M. Hoffman, C. G. Figdor, S. J. Weiss and P. Friedl, *J Cell Biol*, 2013, **201**, 1069-1084.

108. K. F. Toth, T. A. Knoch, M. Wachsmuth, M. Frank-Stohr, M. Stohr, C. P. Bacher, G. Muller and K. Rippe, *J Cell Sci*, 2004, **117**, 4277-4287.

109. G. Galiova, E. Bartova, I. Raska, J. Krejci and S. Kozubek, *Eur J Cell Biol*, 2008, **87**, 291-303.

110. J. H. Zhang, T. D. Chung and K. R. Oldenburg, *J Biomol Screen*, 1999, **4**, 67-73.

111. U. N. Lee, X. Su, D. J. Guckenberger, A. M. Dostie, T. Zhang, E. Berthier and A. B. Theberge, *Lab Chip*, 2018, **18**, 496-504.

112. C. Iliescu, H. Taylor, M. Avram, J. Miao and S. Franssila, *Biomicrofluidics*, 2012, **6**, 16505-1650516.

113. S. M. Thomas and J. R. Grandis, *Cell Cycle*, 2011, **10**, 2626-2627.

114. M. J. Alvarez Cubero, J. A. Lorente, I. Robles-Fernandez, A. Rodriguez-Martinez, J. L. Puche and M. J. Serrano, *Methods Mol Biol*, 2017, **1634**, 283-303.

115. L. T. Li, G. Jiang, Q. Chen and J. N. Zheng, *Mol Med Rep*, 2015, **11**, 1566-1572.

116. J. Chen, W. Zhou, Q. Jia, J. Chen, S. Zhang, W. Yao, F. Wei, Y. Zhang, F. Yang, W. Huang, Y. Zhang, H. Zhang, Y. Zhang, B. Huang, Z. Zhang, H. Jia and N. Wang, *Sci Rep*, 2016, **6**, 19304.

117. S. P. Carey, T. M. D'Alfonso, S. J. Shin and C. A. Reinhart-King, *Crit Rev Oncol Hematol*, 2012, **83**, 170-183.

118. M. L. Circu, S. S. Dykes, J. Carroll, K. Kelly, F. Galiano, A. Greer, J. Cardelli and H. El-Osta, *PLoS One*, 2016, **11**, e0146931.

119. H. A. Kenny, M. Lal-Nag, E. A. White, M. Shen, C. Y. Chiang, A. K. Mitra, Y. Zhang, M. Curtis, E. M. Schryver, S. Bettis, A. Jadhav, M. B. Boxer, Z. Li, M. Ferrer and E. Lengyel, *Nat Commun*, 2016, **7**, 10649.

120. I. Y. Wong, S. Javaid, E. A. Wong, S. Perk, D. A. Haber, M. Toner and D. Irimia, *Nat Mater*, 2014, **13**, 1063-1071.

121. S. H. Au, B. D. Storey, J. C. Moore, Q. Tang, Y. L. Chen, S. Javaid, A. F. Sarioglu, R. Sullivan, M. W. Madden, R. O'Keefe, D. A. Haber, S. Maheswaran, D. M. Langenau, S. L. Stott and M. Toner, *Proc Natl Acad Sci U S A*, 2016, **113**, 4947-4952.

122. Y. C. Chen, B. Humphries, R. Brien, A. E. Gibbons, Y. T. Chen, T. Qyli, H. R. Haley, M. E. Pirone, B. Chiang, A. Xiao, Y. H. Cheng, Y. Luan, Z. Zhang, J. Cong, K. E. Luker, G. D. Luker and E. Yoon, *Sci Rep*, 2018, **8**, 244.

123. L. A. Lautscham, C. Kammerer, J. R. Lange, T. Kolb, C. Mark, A. Schilling, P. L. Strissel, R. Strick, C. Gluth, A. C. Rowat, C. Metzner and B. Fabry, *Biophys J*, 2015, **109**, 900-913.

124. C. M. Denais, R. M. Gilbert, P. Isermann, A. L. McGregor, M. te Lindert, B. Weigelin, P. M. Davidson, P. Friedl, K. Wolf and J. Lammerding, *Science*, 2016, **352**, 353-358.

125. G. Tomaiuolo, *Biomicrofluidics*, 2014, **8**, 051501.

126. A. A. Ungureanu, I. Benilova, O. Krylychkina, D. Braeken, B. De Strooper, C. Van Haesendonck, C. G. Dotti and C. Bartic, *Sci Rep*, 2016, **6**, 25841.

CHAPTER 3

High-throughput cell deformability screening to identify novel anti-cancer compounds

ABSTRACT

Existing approaches to identify anti-cancer treatments target phenotypes such as cell proliferation and invasion. Despite advancements in drug development, the recurrence of cancer due to chemoresistance remains a major clinical challenge and, there is an urgent need for alternative strategies to identify novel anti-cancer therapies. Here we present a complementary approach to discover novel therapeutics by targeting the inherent deformability of cells. We previously found that cisplatin-resistant (Cis-R) ovarian cancer (OVCAR5) cells are more deformable than the drug-sensitive counterparts. To screen cells based on their deformability, we developed a live-cell filtration assay, high-throughput parallel microfiltration (HT-PMF). Using the HT-PMF screening method, we screen cells treated with a library of pharmacologically active compounds (LOPAC^{1280}). We identify statistically robust hits from the screen as the compounds that cause OVCAR5 Cis-R cells to become less deformable. To confirm the effect of top 6 hits on cell deformability and determine sublethal doses, we perform secondary assays. We further demonstrate that these compounds cause human ovarian cancer cells to be less invasive. To identify shared molecular mediators and pathways that regulate mechanotype, we use bioinformatic approaches to analyze the targets and downstream effectors of the top 30 hits from the mechanotype screen from publicly available data; this enables us to identify differentially expressed genes (DEGs). Furthermore, weighted key driver analysis (wKDA) of DEGs determines the important pathway hubs, called key drivers (KDs), which are predicted to drive the change in mechanotype of cells. Overall, our findings suggest that deformability-based screening can provide a complementary tool to identify novel anti-cancer drugs and deepen our understanding of the molecular mediators of altered cell mechanotype.

INTRODUCTION

There is an urgent need for effective cancer therapies. Resistance of human cancers to chemotherapy is a major clinical challenge[1]. While most tumors initially respond to anti-cancer therapies, the development of chemoresistance results in poor patient outcome; the majority of cancer deaths are due to recurrence or non-responsiveness to treatment[2]. Novel drug targets and therapeutics that complement existing treatments to stop cancer progression and block metastasis are urgently needed. Existing anti-cancer approaches have focused on identifying cytotoxic compounds that reduce cancer cell proliferation or increase cell death[3]. If we could identify compounds that block the mechanical phenotype of cells, such treatments could directly impact how cells deform and generate physical forces, which are required to move from primary tumors to form secondary tumors. Identifying treatments based on cellular mechanotype may also reveal drugs that have distinct mechanisms of action that complement common chemotherapeutics; this would enable the development of more effective, synergistic therapeutic strategies. Typical drug development methods include target-based and phenotype-based drug discovery[4]. While molecular targetbased approaches can lead to rapid identification of lead drugs, there is higher degree of uncertainty in validation of the hits[5]. Phenotype-based approaches to drug development have led to the identification of drugs that target complex disease physiology[6]. Thus, targeting cell mechanical phenotype as an alternative phenotype for identification of novel anti-cancer drugs has exciting potential.

The mechanical phenotype of cancer cells is critical in the metastatic cascade: key components of mechanotype include cellular deformability—the ability of cells to deform under mechanical stress; and cellular force generation—the magnitude of physical forces cells generate. To disseminate from the primary tumor, cancer cells generate contractile and protrusive forces to push and pull on the surrounding extracellular matrix and drive their movement[7]. Once in circulation, cells that are stiffer are more resistant to damage by fluid shear stresses[8], which are

encountered in circulation during metastatic dissemination. To seed metastatic sites, tumor cells occlude vascular capillaries. Integrin-mediated adhesion allows attachment of tumor cells to endothelium[9]; to extravasate the vasculature, cells generate forces, deform, and invade to seed new metastatic sites. Importantly, many of the same molecules that regulate mechanotype also regulate cell motility, as they are also important in cellular force generation. There is evidence that cancer cell mechanotype is associated with clinically relevant phenotypes, such as invasion[10,11]—we recently found that trend of reduced deformability of invasive cells holds across 17 different types of cancer cells with genetic and pharmacologic perturbations[10]. Emerging evidence also suggests that mechanotype is associated with chemoresistance. We previously demonstrated that platinum-resistant ovarian cancer cells are more deformable than their drug-sensitive counterparts[12]. Moreover, a variety of clinically used chemotherapy agents tend to make cancer cells less deformable[12-15]. Given the integral role of cell deformability in metastasis, cellular mechanoregulating pathways constitute promising therapeutic targets and disruption of mechanotype at any individual step in this cascade is promising strategy to prevent secondary tumor formation.

Existing methods to measure cell mechanical properties rely on sequential measurements of cell deformability, which challenges scale-up that is required to interface with high throughput screening facilities. Single cell force-probing methods are limited in throughput due to measurement rates of <1 cell/min. Methods to probe the mechanical properties of a larger number of cells include stretching cells that are adhered to a flexible polymeric substrate[16,17], mechanical imaging interferometry[18,19], and microrheology[20-22]; yet such methods are difficult to scale up since cells must be fixed in position. Exploiting flow to pass cells through micron-scale constrictions provides a measure of their deformability using bulk filtration[23-26] or microfluidic devices[27-31]. Flow is also used to transport cells through an optical trap that subjects cells to external stresses at typical rates of ~1 cell/min[32-34]. To achieve even higher throughput, cells are subjected to the

forces generated by fluid interactions at elevated flow inertia; such hydrodynamic stretching devices operate at 10^4 – 10^6 cells/min[35,36], but require optical detection, and subsequent computationally intensive analysis; this is a major limitation in scale-up that is required to achieve significant advances in detection frequency across $>10^2$ samples, and to interface with existing high throughput screening facilities.

We recently developed a novel and innovative approach to discover effective therapeutics using the inherent deformability of cells. The unique feature of the HT-PMF platform is the ability to multiplex measurements of cell deformability, which enables HT-PMF to interface with high throughput screening facilities. HT-PMF relies on the pressure-driven filtration of cells through a membrane with micron-scale pores. Less deformable cells tend to occlude pores more readily than cells that are more deformable; a sample of less deformable cells will thus have a smaller filtrate volume, which is quantified using a plate reader. In contrast to other methods for measuring cell deformability that rely on high speed imaging of cell shape and advanced image analysis, filtration results can be easily quantified within minutes using a plate reader to measure the volume of cell medium based on absorbance of phenol red (560 nm); this enables the HTF method to interface with automated liquid handling platforms to enable high throughput screening[37].

Here we present the results of the first high throughput mechanotype screen. We screened cisplatin-resistant human ovarian cancer cells (OVCAR5-CisR) against the Library of Pharmacologically Active Compounds (LOPAC^{1280}), which contains 1280 FDA-approved compounds, and identified 67 top hits (~5% of compounds) that cause a statistically significant decrease in the deformability of cisplatin-resistant cells compared to vehicle-treated control. Follow-up secondary, orthogonal assays including dose response, invasion, migration assays, and cell cycle analysis reveal the top 6 hits do not consistently affect cell cycle, but all top candidates decrease cell invasion. These findings suggest that PMF identifies compounds that

operate through a distinct mode of action that could be synergistic to existing chemotherapeutics, such as cisplatin, which primarily affect cell proliferation and promotes apoptosis. We also perform bioinformatic meta-analysis to identify key molecular mediators that lead to altered deformability due to treatment with the lead compounds. Furthermore, we identify genes that are predicted to be major drivers of cellular mechanotype. These results suggest that PMF can identify novel anti-cancer drugs, and contribute to a systems-level knowledge of the molecular mediators of cell mechanotype.

RESULTS AND DISCUSSION

Application of HT-PMF assay for HTS

We interface the parallel microfiltration method with the automated liquid handling platform to adapt for high throughput screen[37], called high throughput parallel microfiltration (HT-PMF) (**Figure 1A, Supplementary Figures 1A, B**). In HT-PMF, applied air pressure drives the samples to filter through the micron-scale pores in the polycarbonate membrane. More deformable cells easily deform through the pores resulting in lower % retention measurements, conversely, less deformable cells occlude the pores and result in higher % retention (**Figure 1B**). We also incorporate a rapid readout (% retention) measurement method using a plate reader, relying on the absorbance of phenol red in cell culture media (560 nm).

$$\% \text{ Retention} = \frac{\text{Volume retained}}{\text{Initial volume}} \times 100$$

These advances in PMF technology[12] allow rapid screening of hundreds of samples in parallel with unprecedented throughput. To identify anti-cancer compounds, and molecular modulators of altered cell mechanotype, we use screening strategy detailed in **Figure 1C**. To demonstrate proof-of-concept, we use here cisplatin-resistant ovarian cancer cells. To ensure we would identify

compounds that could be readily translated, we screen the LOPAC library, which contains 1280 FDA-approved, pharmacologically active compounds.

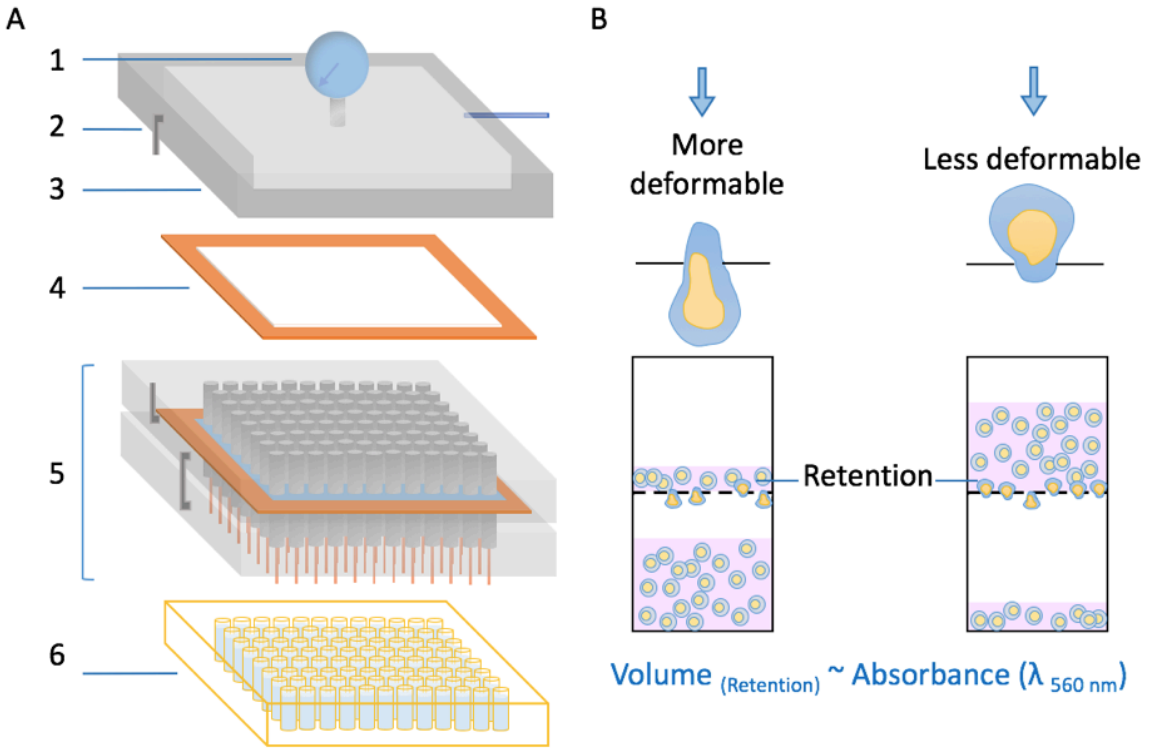

C

Number of compounds tested – 1280

HT deformability-based screen: Identify compounds that reduce deformability of human cisplatin-resistant ovarian cancer (OVCAR5-CisR) cells

Z-factor > 0.5

Top 0.5 % of hits – 6

All hits – 67 (~5%)

Identify top candidates

- Confirm effect of the top hits on cell deformability using PMF dose response assay
- Identify **differentially expressed genes (DEGs)** upon treatment with hits using **bioinformatics analysis** from publicly available data

6 compounds

DEGs

Secondary biological assays

***In vitro* validation**

- Cell growth dose response assay to determine sublethal dose; cell migration, invasion and cell cycle analysis
- Identify **key drivers (KD)** of mechanotype using weighted key driver analysis (wKDA) of DEGs

2 prioritized compounds

KD genes

Effect on patient-derived cells

- Cytotoxicity assay
- Patient risk assessment analysis

Figure 1. Schematic of mechanotype screening platform and process flow (**A**) Schematic of the HT-PMF device: 1. Pressure gauge. 2. Clamps. 3. Pressure chamber. 4. Rubber sealing pad. 5. PMF plate setup (**Supplementary Figure 1**). 6. Standard 96-well plate. (**B**) Absorbance of resulting retention volume is measured to quantify the volume of cell suspension retained above the membrane, % retention. Upon pressure application, less deformable cells result in occlusion of the pores in the polycarbonate membrane resulting in higher % retention. (**C**) Flow chart of HT-PMF deformability-based screen.

Deformability-based HTS and identification of hits

To perform the HT-PMF deformability-based screen of cells treated with LOPAC library compounds, we treat cells with compounds for 24 h prior to filtration. Hits are identified as compounds that result in largest increase in the % retention of the samples; less deformable cells cause occlusion of the pores in polycarbonate membrane resulting in increased retention volume. Hits are compounds of interest that result in reversal of the more deformable mechanotype of the drug-resistant ovarian cancer cells. We rank all the compounds in the library based on the % retention measurements and calculate the respective Z-factors (**Supplementary Figure 2**) as

$$Z = 1 - \frac{3\,SD_{Sample} + 3\,SD_{Control}}{|Mean_{Sample} - Mean_{Control}|}$$

Hits are defined as compounds with Z-factor > 0.5[38] (**Figure 2A**). Based on this criterion we identify 67 drugs as hits, ~5% of the total compounds in the library (**Figure 2B**). We discover a large percentage of 'Cytoskeletal & ECM' targeting compounds as lead compounds; compounds targeting cytoskeleton as well as ECM are known modulators of cell mechanotype. Additionally, ~91% of hits identified are in other drug classes such as, 'neurotransmitters' and 'cell cycle'. (**Supplementary Figure 3**). We prioritize the top 0.05% of the total compounds (6) as lead compounds for follow up secondary validation assays.

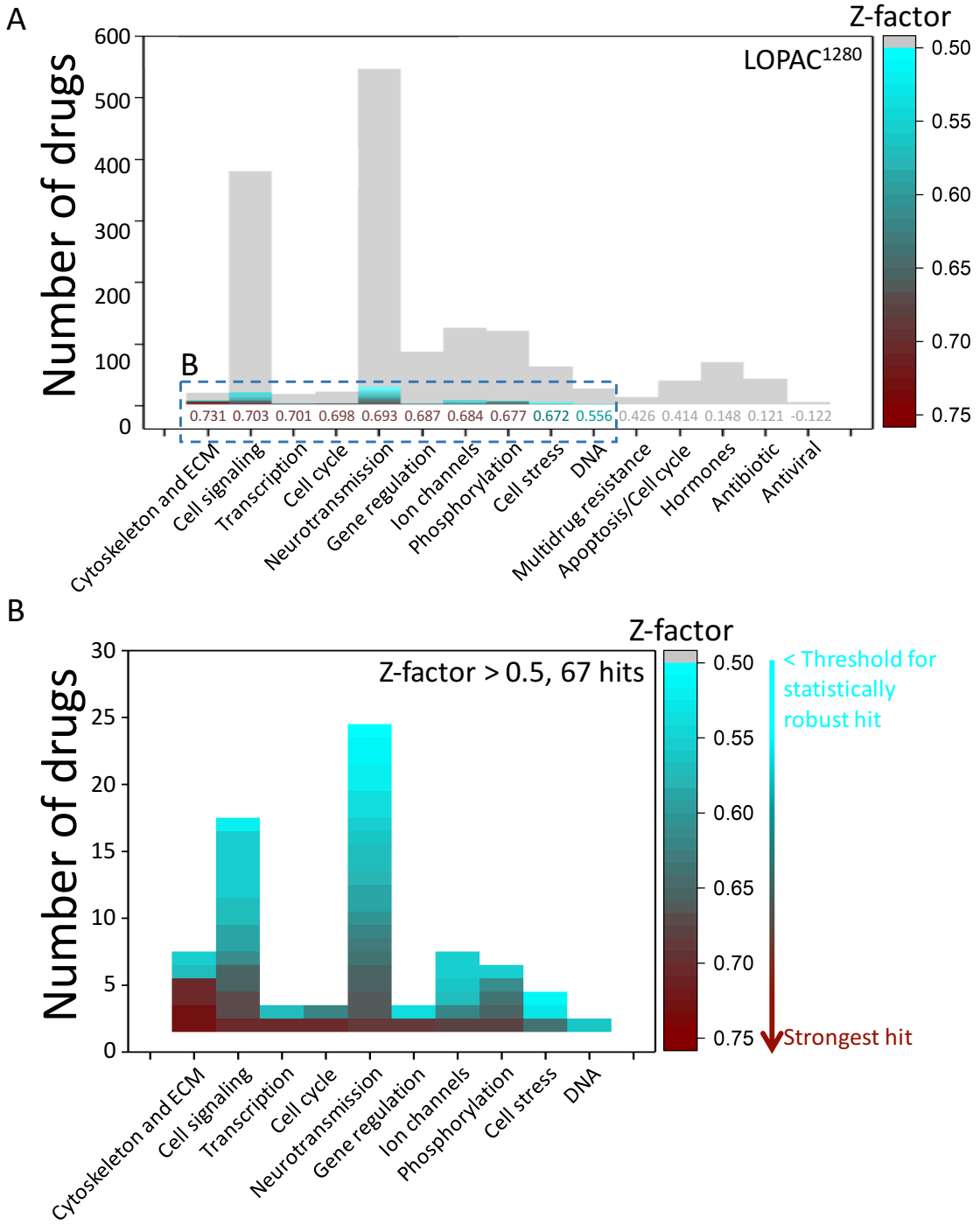

Figure 2. HTS and lead compounds identified by the screen (**A**) % Retention measurements obtained using HT-PMF are used to calculate Z-factors for all the compounds in the library. Compounds are then ranked based on their Z-factor within their respective drug classes. Drug classes are ranked (left to right) based on the highest observed Z-factor in the class. (**B**) 67 lead compounds (Z-factor > 0.5) are identified from the HTS in the indicated drug classes.

In vitro validation of identified hits

We prioritize the top 6 hits (0.5% of compounds) for *in vitro* validation (**Figure 3A**). To confirm compounds alter cellular mechanotype, we measure the effects of increasing concentrations of drug on cellular mechanotype using HT-PMF. This confirms that the identified top 6 hit compounds reduce deformability of OVCAR5 Cis-R. We observe similar decreased deformability in additional high-grade serous ovarian cancer (HGSOC) cell lines, FUOV1 (**Figure 3B**). We next performed cytotoxicity assays from 1 nM to 10 μM compound concentrations. These cytotoxicity data enabled us to determine the sublethal dose in 4 cell lines: human ovarian cancer OVCAR5 Cis-R (acquired cisplatin-resistance), FUOV1 and UWB.289 BRCA- (inherently chemoresistant), and murine ID8 (chemoresistant) cells (**Figure 3C**). These findings confirm that the top 6 compounds are not consistently killing the cells, and thereby making them stiffer.

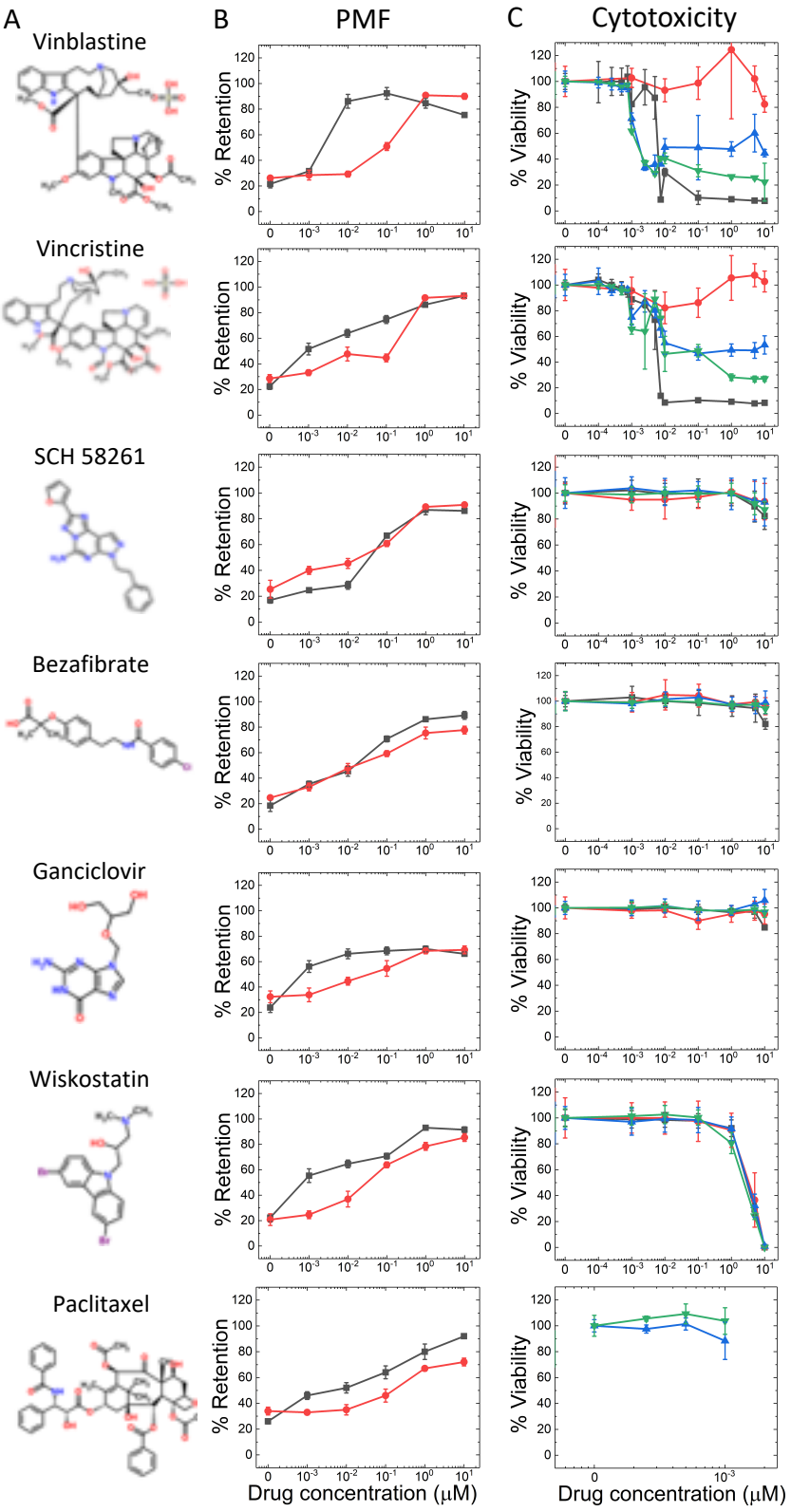
A
B
PMF
C
Cytotoxicity
Vinblastine
Vincristine
SCH 58261
Bezafibrate
Ganciclovir
Wiskostatin
Paclitaxel
% Retention
% Viability
Drug concentration (μM)
OVCAR5-CisR
FUOV1
UWB.289 BRCA-
ID8

Figure 3. Dose response assays for effect of top hits on cell deformability and cytotoxicity. (**A**) Top 6 lead compounds identified from the HT deformability-based screen. (**B**) Cells are treated with a range of concentrations of lead compounds for 24 h before filtration through 10 μm membrane at 2.1 kPa for 50 s. (**C**) Cells are treated with a range of concentrations of lead compounds for 48 h before quantification of the number of viable cells using CellTiterGlo to determine sublethal dose. Data obtained from three independent experiments. Each data point represents mean ± S.D.

Effect of lead compounds on cellular functions

To elucidate the effects of the top 6 lead compounds on cellular functions, we perform additional secondary orthogonal assays. To assay cell invasion, we measure the number of cells that invade through basement membrane extract (BME) matrix in 8 μm pores using a transwell assay; we measure cell migration through uncoated transwell membranes. We find that all top 6 drugs consistently reduce the cell invasion and migration (**Figures 4A, B**). These findings are aligned with previous reports of how more invasive cancer cells are more deformable[10], and reflects how cellular deformability and motility are regulated by shared molecular mediators, suggesting that deformability can be used as a proxy for functional change for drug screening. Since cell deformability is sensitive to cell cycle stage, we first perform cell cycle analysis. While some compounds arrest cells in G2/M phase (vinblastine, vincristine), we find that the lead compounds do not consistently lead to change in cell cycle distribution (**Figure 4C**). We next assay cell invasion, which is an important phenotype of cancer cells that reflects their ability to evade the basement membrane and colonize. Taken together, our data indicate that deformability-based screen can identify drugs that impact cell motility. probe surrogate cell phenotypes, expanding the drug discovery base to compounds that act across a distinct feature space.

Cellular mechanotype is also implicated in the delivery of chemotherapies to the tumor. Importantly, tumor physical properties also determine response to chemotherapy: recent evidence suggests that reducing tumor stiffness can improve treatment response; this can be achieved by decreasing the contractile forces exerted by cancer cells and tumor-associated

fibroblasts (CAFs) within a solid tumor. These exciting findings highlight the potential of blocking cellular mechanotype to increase the penetration of drugs into the tumor core. Moreover, comparing our top hits to the results of screens reported on the basis of cell adhesion and invasion using the same compound library[39], we find no common hits. However, differences in the model system used (here we used established ovarian cancer cell lines), as well as the drug library screened may contribute to differences. Future studies will define the extent to which mechanotype-based screening identifies novel drugs.

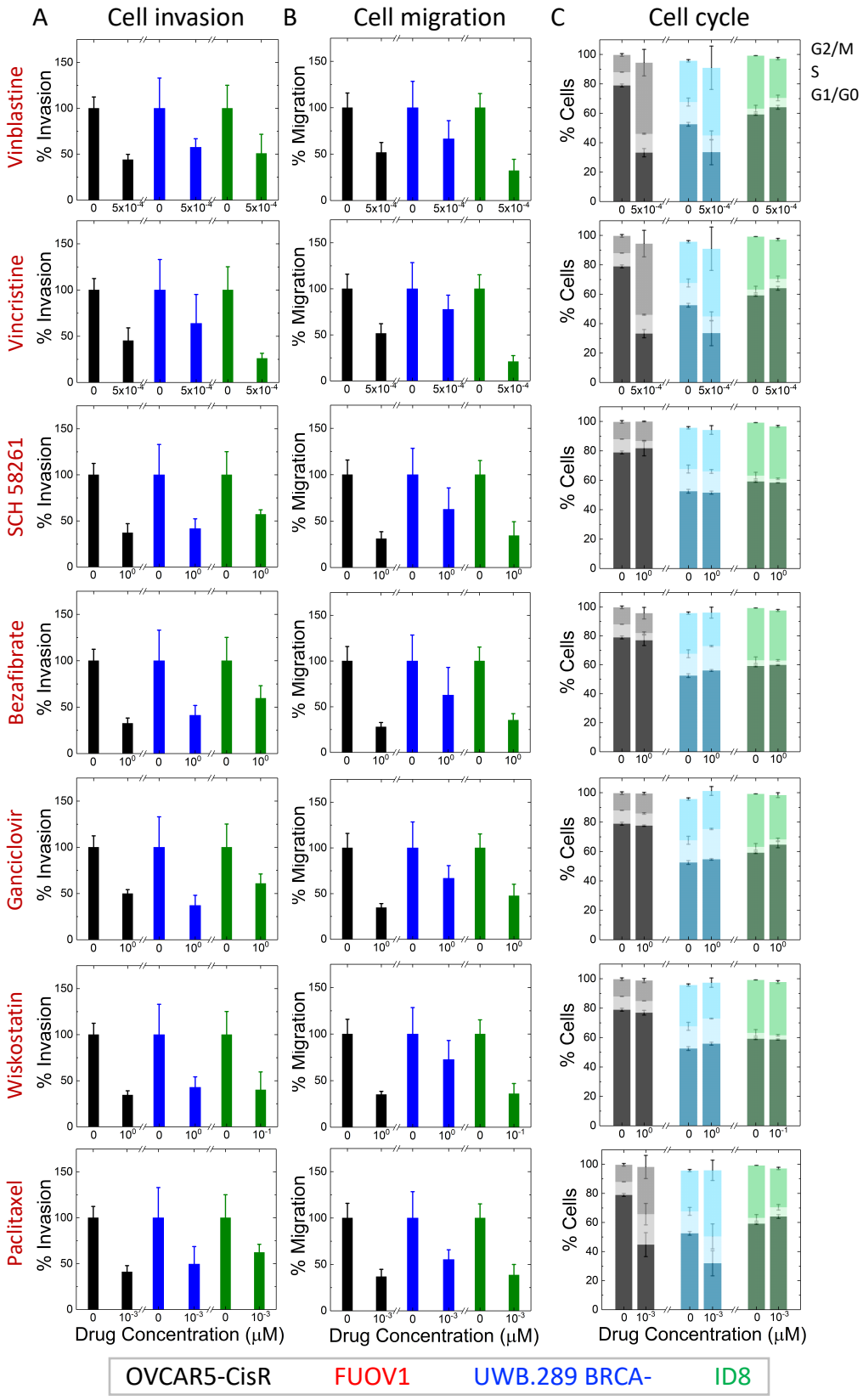
A
Cell invasion
B
Cell migration
C
Cell cycle
G2/M
S
G1/G0
Vinblastine
Vincristine
SCH 58261
Bezafibrate
Ganciclovir
Wiskostatin
Paclitaxel
% Invasion
% Migration
% Cells
Drug Concentration (μM)
OVCAR5-CisR
FUOV1
UWB.289 BRCA-
ID8

Figure 4. Functional assays to determine the effect of hits on cell invasion, migration and cell cycle. Cells are treated with the indicated sublethal concentrations of drugs for 24 h before and 24 h period during the transwell migration of cells through 8 μM transwell (**A**) coated with basement membrane extract (BME) matrix to quantify invasion, and (**B**) uncoated membrane to quantify cell migration. (**C**) Cell cycle distributions of cells with and without the drug treatments. All data obtained from three independent experiments. Each data point represents mean ± S.D.

Effect of prioritized hits on patient-derived cells

To confirm the effect of the top compounds on patient-derived cells we perform dose response cell proliferation assay. We prioritize SCH 58261 and bezafibrate for these studies as the effects of these compounds have not been studied in the context of ovarian cancer. We find that treatment of primary cells derived from ascitic fluid (AF), omentum (OMNT), and primary tumor (PT) from patients exhibit a similar dose response as the OVCA cell lines as described in Figure 3 (**Figure 5**). Similar dose response to the lead compounds implies shared drugs response between established cell lines as well as primary patient cells. Future studies will investigate the efficacy of these drugs in animal models.

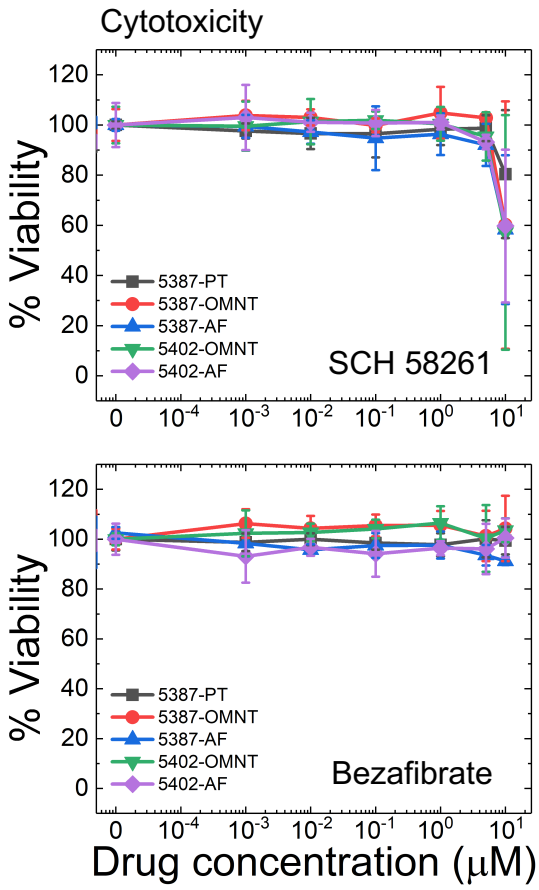

Figure 5. Effect of prioritized hits on growth of patient-derived cells. Cells are treated with a range of concentrations of indicated compounds for 48 h before quantification of the number of viable cells using CellTiterGlo to determine sublethal dose. Data obtained from three independent experiments. Each data point represents mean ± S.D.

Identification of differentially expressed gene signatures of candidate drugs based on publicly available transcriptome datasets

To better understand the molecular underpinnings of the 67 candidate drugs that induced the stiffness phenotype, we conducted a meta-analysis of existing transcriptomic datasets from studies examining various tissues from mammalian species (human, rat, and mouse) with exposure to the drugs to identify shared gene signatures and pathways across the candidate drugs. We first searched for public microarray and RNA-seq data depositories including NCBI Gene Expression Omnibus[40,41], Expression Atlas[42], drugMatrix[43], TG-GATEs[44] and identified

transcriptomic datasets from 20 out of the 67 drug candidates; some drugs were substituted with similar drugs due to the lack of transcriptome datasets of the original candidates. Tissue and organ annotations for the transcriptome datasets identified were standardized based on Brenda ontology[45]. We obtain normalized expression data from GEO, Expression Atlas, and DrugMatrix. As TG-GATEs does not provide normalized data, we used gcrma[46] to normalize array data. Normalized expression data was then log-transformed. Due to the heterogeneity of the datasets in study design, sample size, and profiling platforms, we used non-parametric rank-based analysis to identify treatment induced gene expression changes in each dataset using the GeoDE package[47]. Genes from mouse and rat were converted to human symbols based on ensmbl annotation. We then meta-analyzed across datasets using the Robust Rank Aggregation method[48], a non-parametric statistical method aimed to find highly ranked items across multiple ranking studies, to identify differential expressed genes (DEGs) across drugs at false discovery rate (FDR) < 0.01. Rank aggregation was performed separately for the up-regulated and down-regulated genes to obtain DEGs of both directions across the 20 drugs for which existing transcriptome data are available.

To identify the major pathway hubs or drivers of the mechanotypic changes due to treatment with hits, mechanotype associated with less deformable cells, we mapped the aggregate upregulated and downregulated DEGs across the candidate drugs onto the human or mouse gene networks. We identify top predicted key drivers (KDs) using the weighted key driver analysis (wKDA) approach (**Figure 6A, B**), and top genes in pathways predicted to regulate cell mechanotype using gene set enrichment analysis (GSEA) (**Figure 6B**). Interestingly, while downregulation of many KD genes is linked to less deformable mechanotype of cells treated with the hit compounds, upregulation of these genes is extensively associated with hallmark features of cancer (**Figure 6B**, described in **Supplementary Table 1**). Compared to key drivers and pathways identified in previous efforts of molecular meta-analysis[49,50], some KDs are exclusive to the presented

deformability-based screen. These differences in identified KDs could also be attributed to the different statistical analysis approaches used[49,50]. Additionally, we note that the KDs of altered deformability of cells are identified upon meta-analysis of 20 drugs with publicly available transcriptome data out of all the hits (67) identified.

To investigate how the expression of the identified hub genes is associated with low-, medium- and high-risk ovarian cancer patients, we perform the patient survival risk assessment analysis using data from TCGA ovarian cancer consortium groups using SurvExpress[51] (**Supplementary Figure 4**). We find that expression pattern of many KDs, such as JUN, PRC1, DUSP1 and COL5A1, is associated with high risk group with high prognostic factor. Taken together, these results further highlights the potential of deformability-targeting screen to identify anti-cancer compounds alongside providing detailed insight into molecular mechanism underlying altered cell mechanotype. Further experimental validation will confirm the role of key drivers in regulation of cellular mechanotype.

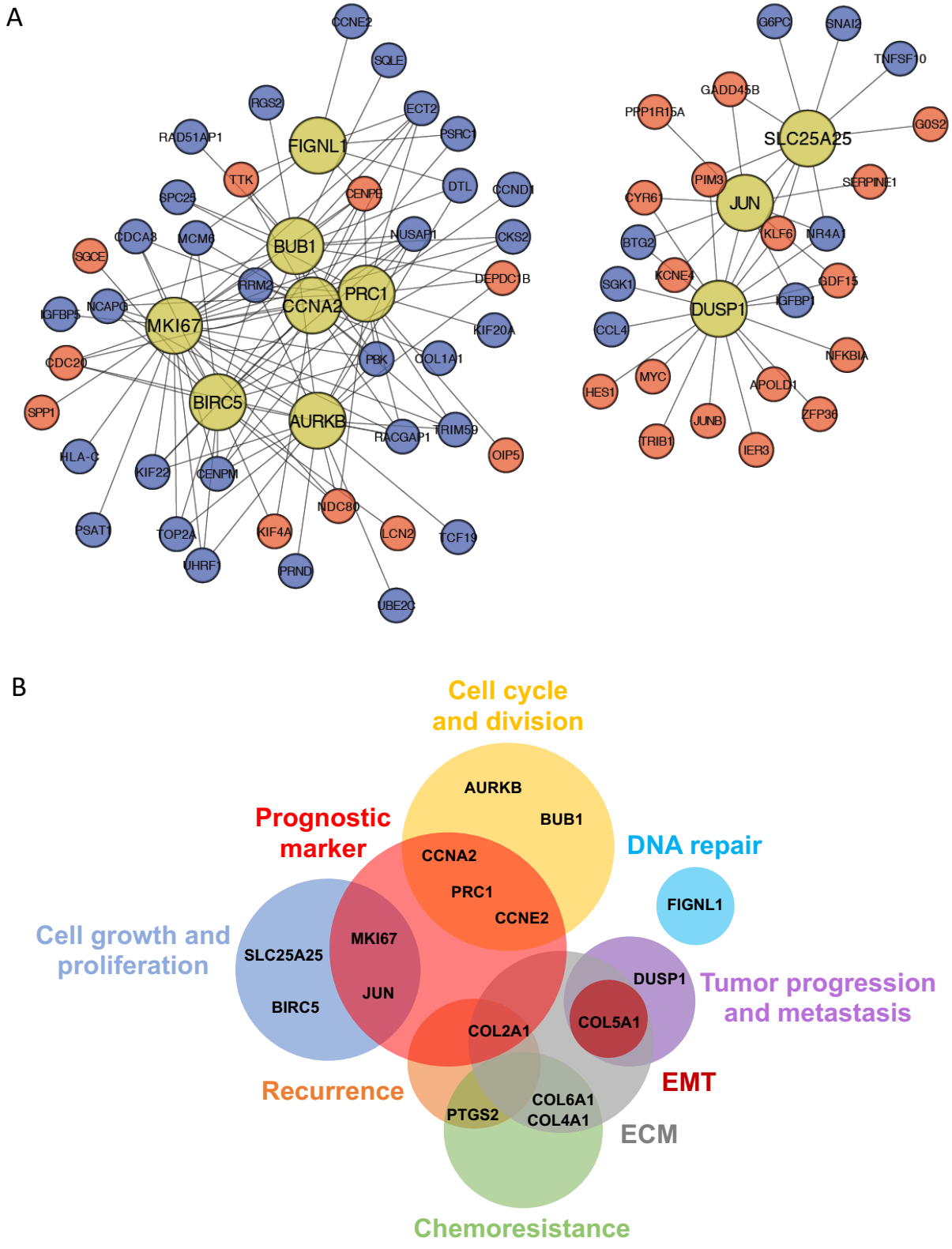

Figure 6. Predicted key drivers of cell mechanotype. Meta-analysis for ranking of the DEGs followed by wKDA and GSEA identifies the top predicted key drivers (KDs) of the mechanotypic

changes in cells as a result of treatment with the compounds identified as hits. (A) Interaction map of DEGs and predicted KDs identified using wKDA. Downregulated genes are indicated in blue, upregulated genes in red and KDs in yellow. (B) Role of top predicted KDs using wKDA and genes predicted to play a role in mechanotype regulation using GSEA in cancer related phenotypes.

METHODS

Cell culture. Human cisplatin-resistant ovarian cancer (OVCAR5 Cis-R) cells are cultured in DMEM (+L-Glutamine, +Glucose, +Sodium Pyruvate, Gibco) supplemented with 10% fetal bovine serum (FBS, Gemini), 1% penicillin-streptomycin (VWR), and 10 μM cisplatin (Sigma-Aldrich). For FUOV1 cells we use DMEM/F-12 (Gibco) with 10% FBS and 1% penicillin-streptomycin. For UWB.289 BRCA- cells we use 50% DMEM/F-12 (Gibco) and 50% RPMI-1640 (Gibco) with 5% FBS, 5% Horse serum and 1% penicillin-streptomycin. ID8 mouse ovarian cancer cells are cultured in DMEM supplemented with 4% FBS, 1% penicillin-streptomycin and 1% insulin-transferrin-selenium (Sigma). Prior to PMF measurements, cells are washed with 1X Phosphate-Buffered Saline (PBS, DNase-, RNase- & Protease- free, Mediatech, Manassas, USA), treated with trypsin, and resuspended in fresh medium.

Drug treatments. Vinblastine, vincristine, SCH 58261, bezafibrate, ganciclovir, wiskostatin and paclitaxel are all obtained from Sigma-Aldrich and reconstituted according to the manufacturer's instruction in dimethyl sulfoxide (DMSO) to prepare stock solutions.

Parallel microfiltration using HT-PMF device: The HT-PMF is setup as shown in Figure 1 and Supplementary Figure 1. Polycarbonate membrane of 10 μm pore size is used for all microfiltration experiments. Cell suspension (360 μL) at 5 x 10^{-5} cell concentration is loaded into each well of 96-well plate sample loading plate. Desired air pressure is applied using pressurized air tank and monitored using a pressure gauge (Noshok Inc., Berea, OH, USA) to drive the cells suspension through the micron-scale pores[52,53]. We determine absorbance of the retention volume using plate reader. To measure cell number and size distributions, we use an automated cell counter (TC20, BioRad).

Absorbance measurements. To quantify the retained volume from the HT-cell filtration we measure absorbance of the volume of cell suspension collected in the 96-well plate. Absorbance of phenol red in the retention volume is read at 560 nm using a plate reader (Infinite M1000, Tecan).

Dose response assays. Cells are plated in a 96-well plate (3000 per well) in cell culture media and incubated at 37 °C for 48 h to allow for cell growth and division. Cells are then stained with CellTiterGlo luminescent cell viability dye (Promega). Luminescence of the live cells is quantified at 560 nm wavelength using a (GloMax 20/20 Luminometer, Promega). Viability of drug treated cells is calculated compared to the untreated cells.

***In vitro* Invasion/migration assay.** Cell invasion assay is setup using the Culturex BME cell invasion assay kit (R&D systems) and cell migration assay is setup using the Culturex migration assay kit (R&D systems). Both the assays are setup according to manufacturer's instructions.

Pathway analysis of the drug DEGs. The up-regulated and down-regulated drug DEGs were assessed for enrichment of pathways or functional categories using enricher[54], a web-based tool which conducts gene set enrichment analysis across multiple annotation databases ranging from transcription factor targets to biological pathways. Top enriched pathways at FDR < 0.05 were reported.

Weighted Key Driver Analysis (wKDA). To prioritize potential regulators of the drug DEGs, we mapped the aggregate upregulated and downregulated DEGs across the candidate drugs onto the human or mouse gene networks to identify key drivers (KDs) using the weighted key driver analysis (wKDA) implemented in Mergeomics[55]. wKDA uniquely consider the edge weight information in the form of edge consistency score for BNs. Specifically, a network was first screened for suitable hub genes whose degree (number of genes connected to the hub) is in the top 25% of all network nodes. Once the hubs have been defined, their local one-edge neighborhoods, or subnetworks were extracted. The drug DEG genes were overlaid onto the hub

subnetworks to see if a particular subnetwork was enriched for the genes from the DEG set. The edges that connect a hub to its neighbors are simplified into node strengths (strength = sum of adjacent edge weights) within the neighborhood, except for the hub itself. The test statistic for the wKDA is: $\chi = \frac{O-E}{\sqrt{E}-\kappa}$, where O and E represent the observed and expected ratios of genes from DEG sets in a hub subnetwork, and κ is a stabilizing factor set to 1. In particular, the expected ratio $E = \frac{N_k N_p}{N}$ is estimated based on the hub degree N_k, DEG gene set size N_p and the order of the full network N, with the implicit assumption that the weight distribution is isotropic across the network. Statistical significance of the disease-enriched hubs, henceforth KDs, is estimated by permuting the gene labels in the network for 10000 times and estimating the P-value based on the null distribution. To control for multiple testing, stringent Bonferroni adjustment was used to focus on the top robust KDs.

Pathway analysis of drug DEGs

The up-regulated and down-regulated drug DEGs were assessed for enrichment of pathways or functional categories using enricher[54], a web-based tool which conducts gene set enrichment analysis across multiple annotation databases ranging from transcription factor targets to biological pathways. Top enriched pathways at FDR < 0.05 were reported.

Statistical methods. HTS is performed once and the Z-factor[38] is calculated for ranking of all the samples. All data is obtained from at least 3 independent measurements and is expressed as mean ± S.D. We use the Student's t-test method to analyze the results and to obtain p-values.

SUPPLEMENTARY FIGURES

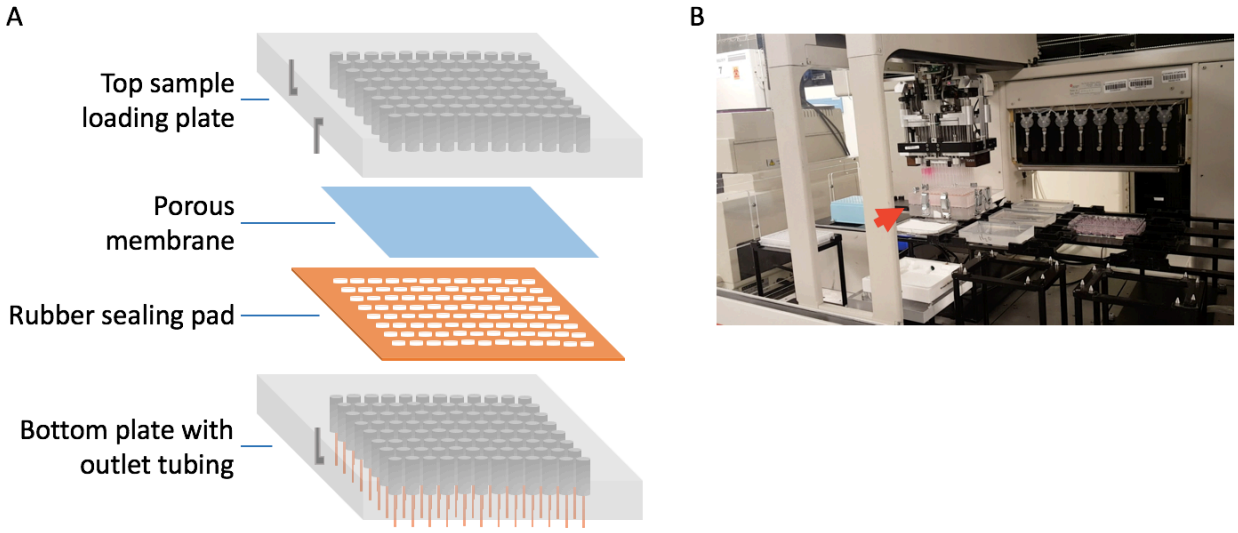

Supplementary Figure 1. Interface of the PMF device with automated HTS equipment. (**A**) PMF-plate setup. (**B**) Interface of the PMF device (red arrow) with automated liquid handling platform. Robotic arms allow processing of cell samples and transfer to HT-PMF device prior to pressure application, and transfer of retention to a standard 96-well plate for absorbance measurements.

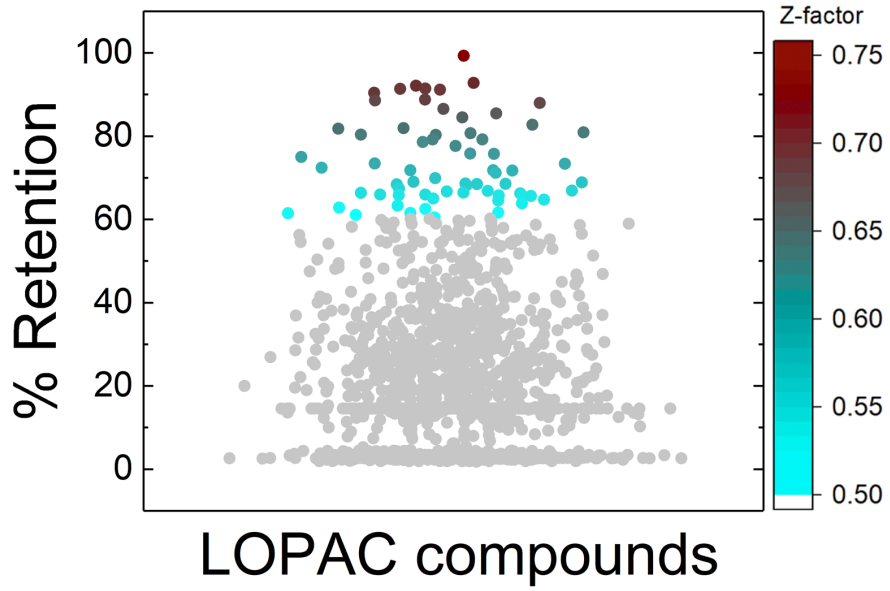

Supplementary Figure 2. Ranking of the LOPAC compounds to identify hits. % Retention of all the compounds in the library is shown. PMF conditions: 0.3 psi applied pressure for 20s, cell density 5 x 10^5 cells well. Each dot represents a drug in the library. Compounds with a Z-factor > 0.5 are identified as statistically robust hits. Top hits are indicated in dark red color.

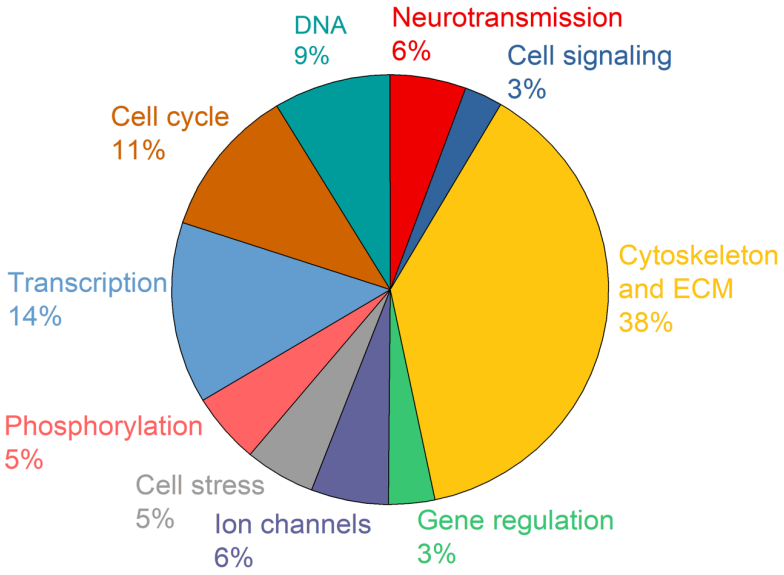

Supplementary Figure 3. Representation of drug classes in the compounds identified as hits. Pie-diagram showing percentage of drugs in each drug class identified as hits. For example, 38% of the drugs in cytoskeletal and ECM class are identified as hits.

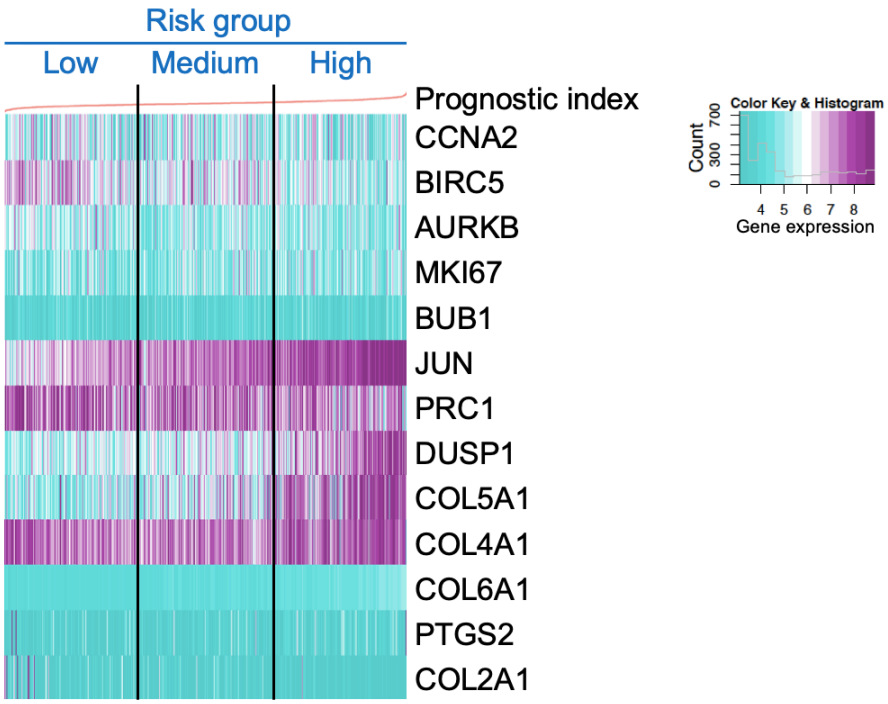

Supplementary Figure 4. Patient-risk assessment analysis of the top key driver genes identified using meta-analysis. Survival data for patients in the ovarian cancer TCGA database is ranked according to the prognostic factor and data collection if divided into low-, medium-, and high-risk groups for the indicated key driver genes. Each vertical line indicates a data from a patient. Gene expression is color mapped from low (turquoise) to high (magenta). Analysis performed using the SurvExpress patient-data analysis tool previously described[51].

Supplementary Table 1. Description of the key drivers.

KDs	Direction of change with hits	Description/role in cell function
MKI67	Downregulated	Antigen Ki-67, a nuclear protein, is a cell proliferation marker; marker for cancer diagnosis[56,57]
DUSP1	NA	Dual-specificity phosphatase-1 (DUSP1/MKP1) is a MAPK/ERK phosphatase; promotes tumorigenesis and progression in ovarian cancers[58,59]
BIRC5	NA	Encodes Survivin protein, a multitasking protein that has dual roles in promoting cell proliferation and preventing apoptosis[60,61]
AURKB	NA	Aurora kinase B, overexpression or gene amplification of Aurora kinases has been clarified in a number of cancers; regulate cytokinesis[62,63]
BUB1	Downregulated	Serine/threonine-protein kinase that performs 2 crucial functions during mitosis: spindle-assembly checkpoint signaling and chromosome alignment[62,64]
CCNA2	Downregulated	Encodes Cyclin-2, regulator of cell cycle; is a prognostic biomarker for ER+ breast cancer and tamoxifen resistance[65]
PRC1	NA	Protein Regulator of cytokinesis 1, microtubule binding and bundling protein essential to maintain the mitotic spindle midzone; linked to poor prognosis in breast cancer[66,67]
JUN	Downregulated	Proto-oncogene, regulates the expression of multiple genes Essential for cell proliferation, differentiation and apoptosis[68-70]
FIGNL1	NA	Fidgetin Like 1, encodes a member of the AAA ATPase family of proteins, recruited to sites of DNA damage where it plays a role in DNA double-strand break repair *via* homologous recombination[71,72]
SLC25A25	Downregulated	Mitochondrial protein transport molecule, Promotes growth of tumor cells[73]
PTGS2	Downregulated	Prostaglandin-Endoperoxide Synthase 2 (cyclooxygenase), involved in inflammation and mitogenesis, Cancer stem cell survival and repopulation of cancer cells during therapy[74-77]
COL2A1	Downregulated	Expression profile of COL2A1 and the pseudogene SLC6A10P predicts tumor recurrence in high-grade serous ovarian cancer[78]
COL4A1	Downregulated	Remodeling of the extracellular matrix through overexpression of collagen VI contributes to cisplatin resistance in ovarian cancer cells[79]
COL5A1	Downregulated	Upregulated in EMT cells[80]
COL6A1	Downregulated	Upregulated in carboplatin/paclitaxel resistant OVCA[81,82]
CCNE2	Downregulated	Cyclin E2 (CCNE2) as independent positive prognostic factor in advanced stage serous ovarian cancer patients[83]

REFERENCES

1. J. Zugazagoitia, C. Guedes, S. Ponce, I. Ferrer, S. Molina-Pinelo and L. Paz-Ares, *Clin Ther*, 2016. Current Challenges in Cancer Treatment. **38**(7): p. 1551-66.
2. H. C. Zheng, *Oncotarget*, 2017. The molecular mechanisms of chemoresistance in cancers. **8**(35): p. 59950-59964.
3. L. A. Baharith, A. Al-Khouli and G. M. Raab, *Stat Med*, 2006. Cytotoxic assays for screening anticancer agents. **25**(13): p. 2323-39.
4. D. C. Swinney, *Clin Pharmacol Ther*, 2013. Phenotypic vs. target-based drug discovery for first-in-class medicines. **93**(4): p. 299-301.
5. F. Sams-Dodd, *Drug Discov Today*, 2005. Target-based drug discovery: is something wrong? **10**(2): p. 139-47.
6. J. G. Moffat, F. Vincent, J. A. Lee, J. Eder and M. Prunotto, *Nat Rev Drug Discov*, 2017. Opportunities and challenges in phenotypic drug discovery: an industry perspective. **16**(8): p. 531-543.
7. D. Wirtz, K. Konstantopoulos and P. C. Searson, *Nat Rev Cancer*, 2011. The physics of cancer: the role of physical interactions and mechanical forces in metastasis. **11**(7): p. 512-22.
8. Q. Huang, X. Hu, W. He, Y. Zhao, S. Hao, Q. Wu, S. Li, S. Zhang and M. Shi, *Am J Cancer Res*, 2018. Fluid shear stress and tumor metastasis. **8**(5): p. 763-777.
9. K. K. Ganguly, S. Pal, S. Moulik and A. Chatterjee, *Cell Adh Migr*, 2013. Integrins and metastasis. **7**(3): p. 251-61.
10. K. D. Nyberg, S. L. Bruce, A. V. Nguyen, C. K. Chan, N. K. Gill, T. H. Kim, E. K. Sloan and A. C. Rowat, *Integr Biol (Camb)*, 2018. Predicting cancer cell invasion by single-cell physical phenotyping. **10**(4): p. 218-231.

11. W. Xu, R. Mezencev, B. Kim, L. Wang, J. McDonald and T. Sulchek, *PLoS One*, 2012. Cell stiffness is a biomarker of the metastatic potential of ovarian cancer cells. **7**(10): p. e46609.

12. D. Qi, N. Kaur Gill, C. Santiskulvong, J. Sifuentes, O. Dorigo, J. Rao, B. Taylor-Harding, W. Ruprecht Wiedemeyer and A. C. Rowat, *Sci Rep*, 2015. Screening cell mechanotype by parallel microfiltration. **5**: p. 17595.

13. W. A. Lam, M. J. Rosenbluth and D. A. Fletcher, *Blood*, 2007. Chemotherapy exposure increases leukemia cell stiffness. **109**(8): p. 3505-8.

14. S. E. Cross, Y. S. Jin, Q. Y. Lu, J. Rao and J. K. Gimzewski, *Nanotechnology*, 2011. Green tea extract selectively targets nanomechanics of live metastatic cancer cells. **22**(21): p. 215101.

15. A. El Kaffas, D. Bekah, M. Rui, J. C. Kumaradas and M. C. Kolios, *Phys Med Biol*, 2013. Investigating longitudinal changes in the mechanical properties of MCF-7 cells exposed to paclitaxol using particle tracking microrheology. **58**(4): p. 923-36.

16. D. R. Beriault, O. Haddad, J. V. McCuaig, Z. J. Robinson, D. Russell, E. B. Lane and D. S. Fudge, *PLoS One*, 2012. The mechanical behavior of mutant K14-R125P keratin bundles and networks in NEB-1 keratinocytes. **7**(2): p. e31320.

17. J. Lammerding and R. T. Lee, *Methods Mol Biol*, 2009. Mechanical properties of interphase nuclei probed by cellular strain application. **464**: p. 13-26.

18. J. Reed, J. Chun, T. A. Zangle, S. Kalim, J. S. Hong, S. E. Pefley, X. Zheng, J. K. Gimzewski and M. A. Teitell, *Biophys J*, 2011. Rapid, Massively Parallel Single-Cell Drug Response Measurements *via* Live Cell Interferometry. **101**(5): p. 1025-31.

19. J. Reed, M. Frank, J. J. Troke, J. Schmit, S. Han, M. A. Teitell and J. K. Gimzewski, *Nanotechnology*, 2008. High throughput cell nanomechanics with mechanical imaging interferometry. **19**(23): p. 235101.

20. A. S. Goldstein and P. A. DiMilla, *J Biomed Mater Res*, 2002. Effect of adsorbed fibronectin concentration on cell adhesion and deformation under shear on hydrophobic surfaces. **59**(4): p. 665-75.

21. J. S. Lee, P. Panorchan, C. M. Hale, S. B. Khatau, T. P. Kole, Y. Tseng and D. Wirtz, *J Cell Sci*, 2006. Ballistic intracellular nanorheology reveals ROCK-hard cytoplasmic stiffening response to fluid flow. **119**(Pt 9): p. 1760-8.

22. P. H. Wu, C. M. Hale, W. C. Chen, J. S. Lee, Y. Tseng and D. Wirtz, *Nat Protoc*, 2012. High-throughput ballistic injection nanorheology to measure cell mechanics. **7**(1): p. 155-70.

23. G. Moessmer and H. J. Meiselman, *Biorheology*, 1990. A new micropore filtration approach to the analysis of white cell rheology. **27**(6): p. 829-48.

24. D. Koutsouris, R. Guillet, J. C. Lelievre, M. T. Guillemin, P. Bertholom, Y. Beuzard and M. Boynard, *Biorheology*, 1988. Determination of erythrocyte transit times through micropores. I--Basic operational principles. **25**(5): p. 763-72.

25. D. Koutsouris, R. Guillet, R. B. Wenby and H. J. Meiselman, *Biorheology*, 1988. Determination of erythrocyte transit times through micropores. II-- Influence of experimental and physicochemical factors. **25**(5): p. 773-90.

26. M. Hanss, *Biorheology*, 1983. Erythrocyte filtrability measurement by the initial flow rate method. **20**(2): p. 199-211.

27. H. W. Hou, Q. S. Li, G. Y. H. Lee, A. P. Kumar, C. N. Ong and C. T. Lim, *Biomedical Microdevices*, 2009. Deformability study of breast cancer cells using microfluidics **11**(3): p. 557-564.

28. B. Yap and R. D. Kamm, *J Appl Physiol*, 2005. Mechanical deformation of neutrophils into narrow channels induces pseudopod projection and changes in biomechanical properties. **98**: p. 1930-9.

29. M. J. Rosenbluth, W. A. Lam and D. A. Fletcher, *Lab Chip*, 2008. Analyzing cell mechanics in hematologic diseases with microfluidic biophysical flow cytometry. **8**: p. 1062-1070.

30. S. Suresh, *Acta Biomater*, 2007. Biomechanics and biophysics of cancer cells. **3**(4): p. 413-38.

31. J. Chen, Y. Zheng, Q. Tan, E. Shojaei-Baghini, Y. L. Zhang, J. Li, P. Prasad, L. You, X. Y. Wu and Y. Sun, *Lab Chip*, 2011. Classification of cell types using a microfluidic device for mechanical and electrical measurement on single cells. **11**: p. 3174-3181.

32. J. Guck, S. Schinkinger, B. Lincoln, F. Wottawah, S. Ebert, M. Romeyke, D. Lenz, H. M. Erickson, R. Ananthakrishnan, D. Mitchell, J. Kas, S. Ulvick and C. Bilby, *Biophys J*, 2005. Optical deformability as an inherent cell marker for testing malignant transformation and metastatic competence. **88**(5): p. 3689-98.

33. F. Lautenschlager, S. Paschke, S. Schinkinger, A. Bruel, M. Beil and J. Guck, *Proc Natl Acad Sci U S A*, 2009. The regulatory role of cell mechanics for migration of differentiating myeloid cells. **106**: p. 15696-701.

34. J. M. Maloney, D. Nikova, F. Lautenschlager, E. Clarke, R. Langer, J. Guck and K. J. Van Vliet, *Biophys J*, 2010. Mesenchymal stem cell mechanics from the attached to the suspended state. **99**(8): p. 2479-87.

35. S. C. Hur, N. K. Henderson-MacLennan, E. R. B. McCabe and D. Di Carlo, *Lab Chip*, 2011. Deformability-based cell classification and enrichment using inertial microfluidics. **11**: p. 912-920.

36. D. R. Gossett, H. T. Tse, S. A. Lee, Y. Ying, A. G. Lindgren, O. O. Yang, J. Rao, A. T. Clark and D. Di Carlo, *Proc Natl Acad Sci U S A*, 2012. Hydrodynamic stretching of single cells for large population mechanical phenotyping. **109**(20): p. 7630-5.

37. D. Pils, A. Bachmayr-Heyda, K. Auer, M. Svoboda, V. Auner, G. Hager, E. Obermayr, A. Reiner, A. Reinthaller, P. Speiser, I. Braicu, J. Sehouli, S. Lambrechts, I. Vergote, S.

Mahner, A. Berger, D. Cacsire Castillo-Tong and R. Zeillinger, *Eur J Cancer*, 2014. Cyclin E1 (CCNE1) as independent positive prognostic factor in advanced stage serous ovarian cancer patients - a study of the OVCAD consortium. **50**(1): p. 99-110.

38. J. H. Zhang, T. D. Chung and K. R. Oldenburg, *J Biomol Screen*, 1999. A Simple Statistical Parameter for Use in Evaluation and Validation of High Throughput Screening Assays. **4**(2): p. 67-73.

39. H. A. Kenny, M. Lal-Nag, E. A. White, M. Shen, C. Y. Chiang, A. K. Mitra, Y. Zhang, M. Curtis, E. M. Schryver, S. Bettis, A. Jadhav, M. B. Boxer, Z. Li, M. Ferrer and E. Lengyel, *Nat Commun*, 2015. Quantitative high throughput screening using a primary human three-dimensional organotypic culture predicts *in vivo* efficacy. **6**: p. 6220.

40. C. Maison, A. Pyrpasopoulou, P. A. Theodoropoulos and S. D. Georgatos, *EMBO J*, 1997. The inner nuclear membrane protein LAP1 forms a native complex with B-type lamins and partitions with spindle-associated mitotic vesicles. **16**(16): p. 4839-50.

41. T. Barrett, S. E. Wilhite, P. Ledoux, C. Evangelista, I. F. Kim, M. Tomashevsky, K. A. Marshall, K. H. Phillippy, P. M. Sherman, M. Holko, A. Yefanov, H. Lee, N. Zhang, C. L. Robertson, N. Serova, S. Davis and A. Soboleva, *Nucleic Acids Res*, 2013. NCBI GEO: archive for functional genomics data sets--update. **41**(Database issue): p. D991-5.

42. R. Petryszak, M. Keays, Y. A. Tang, N. A. Fonseca, E. Barrera, T. Burdett, A. Fullgrabe, A. M. Fuentes, S. Jupp, S. Koskinen, O. Mannion, L. Huerta, K. Megy, C. Snow, E. Williams, M. Barzine, E. Hastings, H. Weisser, J. Wright, P. Jaiswal, W. Huber, J. Choudhary, H. E. Parkinson and A. Brazma, *Nucleic Acids Res*, 2016. Expression Atlas update--an integrated database of gene and protein expression in humans, animals and plants. **44**(D1): p. D746-52.

43. C. Wang, B. Gong, P. R. Bushel, J. Thierry-Mieg, D. Thierry-Mieg, J. Xu, H. Fang, H. Hong, J. Shen, Z. Su, J. Meehan, X. Li, L. Yang, H. Li, P. P. Labaj, D. P. Kreil, D. Megherbi, S. Gaj, F. Caiment, J. van Delft, J. Kleinjans, A. Scherer, V. Devanarayan, J.

Wang, Y. Yang, H. R. Qian, L. J. Lancashire, M. Bessarabova, Y. Nikolsky, C. Furlanello, M. Chierici, D. Albanese, G. Jurman, S. Riccadonna, M. Filosi, R. Visintainer, K. K. Zhang, J. Li, J. H. Hsieh, D. L. Svoboda, J. C. Fuscoe, Y. Deng, L. Shi, R. S. Paules, S. S. Auerbach, and W. Tong, *Nat Biotechnol*, 2014. The concordance between RNA-seq and microarray data depends on chemical treatment and transcript abundance. **32**(9): p. 926-32.

44. Y. Igarashi, N. Nakatsu, T. Yamashita, A. Ono, Y. Ohno, T. Urushidani and H. Yamada, *Nucleic Acids Res*, 2015. Open TG-GATEs: a large-scale toxicogenomics database. **43**(Database issue): p. D921-7.

45. M. Gremse, A. Chang, I. Schomburg, A. Grote, M. Scheer, C. Ebeling and D. Schomburg, *Nucleic Acids Res*, 2011. The BRENDA Tissue Ontology (BTO): the first all-integrating ontology of all organisms for enzyme sources. **39**(Database issue): p. D507-13.

46. Z. Wu, R. A. Irizarry, R. Gentleman, F. Martinez-Murillo and F. Spencer, *Journal of the American Statistical Association*, 2004. A Model-Based Background Adjustment for Oligonucleotide Expression Arrays. **99**(468): p. 909-917.

47. N. R. Clark, K. S. Hu, A. S. Feldmann, Y. Kou, E. Y. Chen, Q. Duan and A. Ma'ayan, *BMC Bioinformatics*, 2014. The characteristic direction: a geometrical approach to identify differentially expressed genes. **15**: p. 79.

48. R. Kolde, S. Laur, P. Adler and J. Vilo, *Bioinformatics*, 2012. Robust rank aggregation for gene list integration and meta-analysis. **28**(4): p. 573-80.

49. E. Bicaku, Y. Xiong, D. C. Marchion, H. S. Chon, X. B. Stickles, N. Chen, P. L. Judson, A. Hakam, J. Gonzalez-Bosquet, R. M. Wenham, S. M. Apte, W. Fulp, C. L. Cubitt, D. T. Chen and J. M. Lancaster, *Br J Cancer*, 2012. *In vitro* analysis of ovarian cancer response to cisplatin, carboplatin, and paclitaxel identifies common pathways that are also associated with overall patient survival. **106**(12): p. 1967-75.

50. S. Willis, V. M. Villalobos, O. Gevaert, M. Abramovitz, C. Williams, B. I. Sikic and B. Leyland-Jones, *PLoS One*, 2016. Single Gene Prognostic Biomarkers in Ovarian Cancer: A Meta-Analysis. **11**(2): p. e0149183.

51. R. Aguirre-Gamboa, H. Gomez-Rueda, E. Martinez-Ledesma, A. Martinez-Torteya, R. Chacolla-Huaringa, A. Rodriguez-Barrientos, J. G. Tamez-Pena and V. Trevino, *PLoS One*, 2013. SurvExpress: an online biomarker validation tool and database for cancer gene expression data using survival analysis. **8**(9): p. e74250.

52. N. K. Gill, D. Qi, T.-H. Kim, C. Chan, A. Nguyen, K. D. Nyberg and A. C. Rowat, 2017. *A protocol for screening cells based on deformability using parallel microfiltration*.

53. D. Qi, N. Kaur Gill, C. Santiskulvong, J. Sifuentes, O. Dorigo, J. Rao, B. Taylor-Harding, W. Ruprecht Wiedemeyer and A. Rowat, *Sci Rep*, 2015. Screening cell mechanotype by parallel microfiltration. **5**: p. 17595.

54. E. Y. Chen, C. M. Tan, Y. Kou, Q. Duan, Z. Wang, G. V. Meirelles, N. R. Clark and A. Ma'ayan, *BMC Bioinformatics*, 2013. Enrichr: interactive and collaborative HTML5 gene list enrichment analysis tool. **14**: p. 128.

55. L. Shu, Y. Zhao, Z. Kurt, S. G. Byars, T. Tukiainen, J. Kettunen, L. D. Orozco, M. Pellegrini, A. J. Lusis, S. Ripatti, B. Zhang, M. Inouye, V. P. Makinen and X. Yang, *BMC Genomics*, 2016. Mergeomics: multidimensional data integration to identify pathogenic perturbations to biological systems. **17**(1): p. 874.

56. L. T. Li, G. Jiang, Q. Chen and J. N. Zheng, *Mol Med Rep*, 2015. Ki67 is a promising molecular target in the diagnosis of cancer (review). **11**(3): p. 1566-72.

57. A. Mahadevappa, S. M. Krishna and M. G. Vimala, *J Clin Diagn Res*, 2017. Diagnostic and Prognostic Significance of Ki-67 Immunohistochemical Expression in Surface Epithelial Ovarian Carcinoma. **11**(2): p. EC08-EC12.

58. Y. Kang, A. S. Nagaraja, G. N. Armaiz-Pena, P. L. Dorniak, W. Hu, R. Rupaimoole, T. Liu, K. M. Gharpure, R. A. Previs, J. M. Hansen, C. Rodriguez-Aguayo, C. Ivan, P. Ram,

V. Sehgal, G. Lopez-Berestein, S. K. Lutgendorf, S. W. Cole and A. K. Sood, *Clin Cancer Res*, 2016. Adrenergic Stimulation of DUSP1 Impairs Chemotherapy Response in Ovarian Cancer. **22**(7): p. 1713-24.

59. J. Shen, Y. Zhang, H. Yu, B. Shen, Y. Liang, R. Jin, X. Liu, L. Shi and X. Cai, *Cancer Med*, 2016. Role of DUSP1/MKP1 in tumorigenesis, tumor progression and therapy. **5**(8): p. 2061-8.
60. C. Cohen, C. M. Lohmann, G. Cotsonis, D. Lawson and R. Santoianni, *Mod Pathol*, 2003. Survivin expression in ovarian carcinoma: correlation with apoptotic markers and prognosis. **16**(6): p. 574-83.
61. P. K. Jaiswal, A. Goel and R. D. Mittal, *Indian J Med Res*, 2015. Survivin: A molecular biomarker in cancer. **141**(4): p. 389-97.
62. B. Davidson, D. A. Nymoen, B. V. Elgaaen, A. C. Staff, C. G. Trope, J. Kaern, R. Reich and T. E. Falkenthal, *Virchows Arch*, 2014. BUB1 mRNA is significantly co-expressed with AURKA and AURKB mRNA in advanced-stage ovarian serous carcinoma. **464**(6): p. 701-7.
63. A. Tang, K. Gao, L. Chu, R. Zhang, J. Yang and J. Zheng, *Oncotarget*, 2017. Aurora kinases: novel therapy targets in cancers. **8**(14): p. 23937-23954.
64. T. Chong, A. Sarac, C. Q. Yao, L. Liao, N. Lyttle, P. C. Boutros, J. M. S. Bartlett and M. Spears, *J Ovarian Res*, 2018. Deregulation of the spindle assembly checkpoint is associated with paclitaxel resistance in ovarian cancer. **11**(1): p. 27.
65. T. Gao, Y. Han, L. Yu, S. Ao, Z. Li and J. Ji, *PLoS One*, 2014. CCNA2 is a prognostic biomarker for ER+ breast cancer and tamoxifen resistance. **9**(3): p. e91771.
66. M. Ehrlichova, B. Mohelnikova-Duchonova, J. Hrdy, V. Brynychova, M. Mrhalova, R. Kodet, L. Rob, M. Pluta, I. Gut, P. Soucek and R. Vaclavikova, *Genomics*, 2013. The association of taxane resistance genes with the clinical course of ovarian carcinoma. **102**(2): p. 96-101.

67. Y. Wang, F. Shi, G. H. Xing, P. Xie, N. Zhao, Y. F. Yin, S. Y. Sun, J. He, Y. Wang and S. Y. Xuan, *J Cancer*, 2017. Protein Regulator of Cytokinesis PRC1 Confers Chemoresistance and Predicts an Unfavorable Postoperative Survival of Hepatocellular Carcinoma Patients. **8**(5): p. 801-808.

68. K. Eckhoff, R. Flurschutz, F. Trillsch, S. Mahner, F. Janicke and K. Milde-Langosch, *J Cancer Res Clin Oncol*, 2013. The prognostic significance of Jun transcription factors in ovarian cancer. **139**(10): p. 1673-80.

69. Y. Xia, W. Yang, W. Bu, H. Ji, X. Zhao, Y. Zheng, X. Lin, Y. Li and Z. Lu, *J Biol Chem*, 2013. Differential regulation of c-Jun protein plays an instrumental role in chemoresistance of cancer cells. **288**(27): p. 19321-9.

70. M. Hartl, A. G. Bader and K. Bister, *Curr Cancer Drug Targets*, 2003. Molecular targets of the oncogenic transcription factor jun. **3**(1): p. 41-55.

71. J. Ma, J. Li, X. Yao, S. Lin, Y. Gu, J. Xu, Z. Deng, W. Ma and H. Zhang, *Oncol Rep*, 2017. FIGNL1 is overexpressed in small cell lung cancer patients and enhances NCI-H446 cell resistance to cisplatin and etoposide. **37**(4): p. 1935-1942.

72. Y. Huo, Z. Zheng, Y. Chen, Q. Wang, Z. Zhang and H. Deng, *Oncotarget*, 2016. Downregulation of vimentin expression increased drug resistance in ovarian cancer cells. **7**(29): p. 45876-45888.

73. O. Lytovchenko and E. R. S. Kunji, *Biochim Biophys Acta Bioenerg*, 2017. Expression and putative role of mitochondrial transport proteins in cancer. **1858**(8): p. 641-654.

74. J. Li, X. Kong, J. Zhang, Q. Luo, X. Li and L. Fang, *Cancer Cell Int*, 2013. MiRNA-26b inhibits proliferation by targeting PTGS2 in breast cancer. **13**(1): p. 7.

75. B. Liu, L. Qu and S. Yan, *Cancer Cell Int*, 2015. Cyclooxygenase-2 promotes tumor growth and suppresses tumor immunity. **15**: p. 106.

76. L. Y. Pang, E. A. Hurst and D. J. Argyle, *Stem Cells Int*, 2016. Cyclooxygenase-2: A Role in Cancer Stem Cell Survival and Repopulation of Cancer Cells during Therapy. **2016**: p. 2048731.

77. H. Sun, X. Zhang, D. Sun, X. Jia, L. Xu, Y. Qiao and Y. Jin, *Oncotarget*, 2017. COX-2 expression in ovarian cancer: an updated meta-analysis. **8**(50): p. 88152-88162.

78. M. K. Ganapathi, W. D. Jones, J. Sehouli, C. M. Michener, I. E. Braicu, E. J. Norris, C. V. Biscotti, S. A. Vaziri and R. N. Ganapathi, *Int J Cancer*, 2016. Expression profile of COL2A1 and the pseudogene SLC6A10P predicts tumor recurrence in high-grade serous ovarian cancer. **138**(3): p. 679-88.

79. R. Jin, J. Shen, T. Zhang, Q. Liu, C. Liao, H. Ma, S. Li and Z. Yu, *Oncotarget*, 2017. The highly expressed COL4A1 genes contributes to the proliferation and migration of the invasive ductal carcinomas. **8**(35): p. 58172-58183.

80. D. J. Cheon, Y. Tong, M. S. Sim, J. Dering, D. Berel, X. Cui, J. Lester, J. A. Beach, M. Tighiouart, A. E. Walts, B. Y. Karlan and S. Orsulic, *Clin Cancer Res*, 2014. A collagen-remodeling gene signature regulated by TGF-beta signaling is associated with metastasis and poor survival in serous ovarian cancer. **20**(3): p. 711-23.

81. D. Anastassiou, V. Rumjantseva, W. Cheng, J. Huang, P. D. Canoll, D. J. Yamashiro and J. J. Kandel, *BMC Cancer*, 2011. Human cancer cells express Slug-based epithelial-mesenchymal transition gene expression signature obtained *in vivo*. **11**: p. 529.

82. R. Januchowski, M. Swierczewska, K. Sterzynska, K. Wojtowicz, M. Nowicki and M. Zabel, *J Cancer*, 2016. Increased Expression of Several Collagen Genes is Associated with Drug Resistance in Ovarian Cancer Cell Lines. **7**(10): p. 1295-310.

83. C. E. Caldon and E. A. Musgrove, *Cell Div*, 2010. Distinct and redundant functions of cyclin E1 and cyclin E2 in development and cancer. **5**: p. 2.

CHAPTER 4

DYT1 dystonia patient-derived fibroblasts have increased deformability and susceptibility to damage by mechanical forces

Abstract

DYT1 dystonia is a neurological movement disorder that is caused by a loss-of-function mutation in the *DYT1*/*TOR1A* gene, which encodes torsinA, the luminal ATPase-associated (AAA+) protein. TorsinA is required for the assembly of functional linker of nucleoskeleton and cytoskeleton (LINC) complexes, and consequently the mechanical integration of the nucleus and the cytoskeleton. Despite the potential implications of altered mechanobiology in dystonia pathogenesis, the role of torsinA in regulating cellular mechanical phenotype, or mechanotype, in DYT1 dystonia remains unknown. Here, we define the mechanotype of mouse fibroblasts lacking functional torsinA as well as human fibroblasts isolated from DYT1 dystonia patients. We find that the deletion of torsinA or the expression of torsinA containing the DYT1 dystonia-causing ΔE302/303 (ΔE) mutation results in a more deformable cellular mechanotype. We observe a similar increased deformability of mouse fibroblasts that lack lamina-associated polypeptide 1 (LAP1), which interacts with and stimulates the ATPase activity of torsinA *in vitro*; as well as with depletion of the LINC complex proteins, Sad1/UNC-84 (SUN)1 and SUN2, lamin A/C, or lamin B1. Moreover, we report that DYT1 dystonia patient-derived fibroblasts are more compliant than fibroblasts isolated from unafflicted individuals. DYT1 fibroblasts also exhibit increased nuclear strain and decreased viability following mechanical stretch. Taken together, our results support a model where the physical connectivity between the cytoskeleton and nucleus contributes to cellular mechanotype. These findings establish the foundation for future mechanistic studies to understand how altered cellular mechanotype may contribute to DYT1 dystonia pathogenesis; this may be particularly relevant in the context of how neurons sense and respond to mechanical forces during traumatic brain injury, which is known to be a major cause of acquired dystonia.

Keywords: TorsinA, LINC complex, mechanotype, cell mechanical properties, nuclear envelope, lamins

1 Introduction

Dystonia is a debilitating 'hyperkinetic' neurological movement disorder, which is the third most common movement disorder worldwide behind essential tremor and Parkinson's disease (Fahn, 1988; Fahn et al., 1988; Geyer and Bressman, 2006; Defazio et al., 2007). Dystonia is characterized by involuntary sustained or intermittent muscle contractions resulting in abnormal repetitive movements and/or postures (Fahn, 1988; Albanese et al., 2013). While there are multiple treatment options to manage dystonia—such as botulinum toxin injection, oral medications, and deep brain stimulation—no curative therapies are available (Albanese et al., 2013). If we could fully define the mechanisms of disease pathogenesis, this would enable the development of effective targeted treatment strategies for dystonia patients.

Dystonia can be acquired as a result of traumatic brain injury, central nervous system infection, or environmental toxins (Albanese et al., 2013; Albanese et al., 2018). This neurological disorder can also be inherited: the most prevalent and severe inherited dystonia (Weisheit et al., 2018), DYT1 dystonia, is caused by a loss-of-function mutation in the *DYT1*/*TOR1A* gene that deletes a single glutamic acid residue (ΔE302/303, or ΔE) from the encoded torsinA protein (Ozelius et al., 1997). TorsinA is a ATPase-associated with various cellular activities (AAA+) protein, which resides within the lumen of the endoplasmic reticulum lumen and the contiguous perinuclear space of the nuclear envelope (Goodchild and Dauer, 2004; Naismith et al., 2004). AAA^+ proteins typically function as ATP-dependent molecular chaperones that structurally remodel their protein substrates (Hanson and Whiteheart, 2005). While the substrate(s) remodeled by torsinA are unknown, torsinA is thought to function within the nuclear envelope where its ATPase activity is stimulated by its membrane-spanning co-factors: lamina-associated polypeptide 1 (LAP1) and

luminal domain-like LAP1 (LULL1) (Laudermilch and Schlieker, 2016). While the ΔE mutation impairs the ability of torsinA to interact with or be stimulated by either LAP1 or LULL1 (Naismith et al., 2009; Zhao et al., 2013), a mechanistic understanding of how the ΔE mutation drives DYT1 dystonia pathogenesis at the cellular level remains unclear.

We recently identified torsinA and LAP1 as mediators of the assembly of functional linker of nucleoskeleton and cytoskeleton (LINC complexes) (Saunders and Luxton, 2016; Saunders et al., 2017), which are evolutionarily conserved nuclear envelope-spanning molecular bridges that mechanically integrate the nucleus and the cytoskeleton (Kaminski et al., 2014; Chang et al., 2015b). LINC complexes are composed of the outer and inner nuclear membrane nesprin and SUN proteins: nesprins interact with the cytoskeleton in the cytoplasm and SUN proteins in the perinuclear space, whereas SUN proteins interact with A-type lamins and chromatin-binding proteins in the nucleoplasm (Crisp et al., 2006; Wilson and Berk, 2010; Chang et al., 2015a). Our previous work demonstrated that torsinA and LAP1 are required for the assembly of transmembrane actin-associated nuclear (TAN) lines (Saunders et al., 2017), which are linear arrays of LINC complexes containing the actin-binding nesprin-2Giant (nesprin-2G) and SUN2 that harness the forces generated by the retrograde flow of perinuclear actin cables to move the nucleus towards the rear of migrating fibroblasts and myoblasts (Luxton et al., 2010; Luxton et al., 2011; Chang et al., 2015a). Consistent with these findings, DYT1 dystonia patient-derived fibroblasts and fibroblasts isolated from mouse models of DYT1 dystonia exhibit reduced motility *in vitro* (Nery et al., 2008; Nery et al., 2014). Moreover, the migration of torsinA-null neurons in the dorsal forebrain of mouse embryos *in vivo* show impaired migration (McCarthy et al., 2012; Nery et al., 2014). Since intracellular force generation is critical for cell motility, and regulated by shared mediators of mechanotype, these results suggest that DYT1 dystonia may be characterized by defective mechanobiology.

Here we test the hypothesis that torsinA regulates cellular mechanical phenotype, or mechanotype, which describes how cells deform in response to mechanical stresses. Cellular mechanotype is critical for mechanotransduction, whereby cells translate mechanical stimuli from their environment into biochemical signals and altered gene expression (Tyler, 2012; Franze, 2013). The ability of cells to withstand physical forces is also critical for their survival (Hsieh and Nguyen, 2005). For example, the external stresses of traumatic brain injury result in cell death (Raghupathi, 2004; Stoica and Faden, 2010; Hiebert et al., 2015; Ganos et al., 2016). Damage to cells can also occur during migration through narrow constrictions, including nuclear rupture, DNA damage, and ultimately cell death (Harada et al., 2014; Denais et al., 2016; Raab et al., 2016; Irianto et al., 2017). The damaging effects of such large cellular deformations depend on levels of A-type nuclear lamins, which are critical regulators of nuclear and cellular mechanotype (Lammerding et al., 2004; Swift et al., 2013; Stephens et al., 2017). The depletion of other proteins that associate with nuclear lamins, such as the inner nuclear membrane protein emerin, also result in reduced mechanical stability of the nuclear envelope (Rowat et al., 2006; Reis-Sobreiro et al., 2018) and increased nuclear deformability in response to strain (Lammerding et al., 2005). The nuclear lamina interacts with chromatin, which can also contribute to nuclear mechanical properties (Pajerowski et al., 2007; Chalut et al., 2012; Schreiner et al., 2015; Stephens et al., 2017). In addition, nuclear lamins associate with the LINC complex, which is an important mediator of the transmission of physical forces generated from the cytoskeleton to the nucleus (Stewart-Hutchinson et al., 2008; Lombardi et al., 2011; Spagnol and Dahl, 2014). Given that torsinA is required for the assembly of functional LINC complexes (Saunders et al., 2017), we speculated that DYT1 dystonia cells may exhibit altered mechanotype, which could contribute to the pathogenesis of DYT1 dystonia.

Here we show that cellular mechanotype is altered due to the expression of torsinA containing the DYT1 dystonia-causing ΔE mutation, the deletion of torsinA, or the disruption of functional

LINC complexes. We use fibroblasts as a model system, which have been used successfully to model human neurological disorders, including dystonia (Connolly, 1998; Hewett et al., 2006; Auburger et al., 2012; Burbulla and Kruger, 2012; Wray et al., 2012; Nery et al., 2014). We find that mouse embryonic fibroblasts (MEFs) derived from torsinA- or LAP1-knockout as well as ΔE-knock-in mice are more deformable than control fibroblasts. We observe a similar, more compliant mechanotype in MEFs lacking functional LINC complexes as well as A- or B-type lamins. Furthermore, we find that fibroblasts isolated from DYT1 dystonia patients are more deformable than normal fibroblasts. Interestingly we observe that DYT1 fibroblasts exhibit nuclei with greater strain and decreased cell viability following mechanical stretching. Collectively these findings establish altered cellular mechanotype as a potential biomarker of DYT1 dystonia, which will guide future studies designed to better understand dystonia pathogenesis and to identify novel therapeutic targets for treatment of this debilitating disease.

2 Materials and methods

2.1 Cells

Parental NIH3T3 fibroblasts were cultured in L-glutamine-, glucose-, and sodium pyruvate-containing Dulbecco's modified Eagle's media (DMEM) (ThermoFisher Scientific, Waltham, MA) supplemented with 10% bovine calf serum (BCS) (Gemini Bio-Products, West Sacramento, CA). NIH3T3 fibroblasts stably expressing wild type (WT), or mutant (E171Q or ΔE) versions of torsinA containing EGFP inserted after its signal sequence (SS) were created as follows: the open reading frame encoding SS-EGFP-torsinA was amplified by PCR from the previously described SS-EGFP-torsinA WT, SS-EGFP-torsinA E171Q and SS-EGFP-torsinA ΔE constructs (Saunders et al., 2017) using the primers SS-EGFP-F (5'-GGGCGCCTCGAGATGAAGCTGGGCCGGG-3') and SS-EGFP-torsinA-R (5'-GCGCCCGAATTCTCAATCATCGTAGTAATAATCTAACTTGGTG-3'), which contain 5' *Xho*I and *Eco*RI cut sites, respectively. The resulting PCR products were

each purified using the Wizard SV Gel and PCR Clean-Up System (Promega, Madison, WI) and then subcloned into the cytomegalovirus immediate-early expression cassette of the pLPCX retroviral vector (Takara Bio USA, Inc., Mountain View, CA). Phusion DNA polymerase and T4 DNA ligase were purchased from New England Biolabs (Ipswich, MA). Restriction enzymes were either purchased from New England Biolabs or Promega. The resultant pLPCX cDNA constructs and pVSV-G (Takara Bio USA, Inc.) were purified using the GeneJet Plasmid Midiprep Kit (ThermoFisher Scientific) and cotransfected into the gp293 retroviral packaging cell line (Takara Bio USA, Inc.); the subsequent isolation of retroviral particles was performed as recommended by the manufacturer. NIH3T3 fibroblasts were transduced with the resultant retrovirus and selected with 2 μg/mL puromycin (Thermo Fisher Scientific). Individual clones of the resultant cell lines were isolated using limiting dilution and maintained with 2 μg/mL of puromycin. Mouse embryonic fibroblasts (MEF) lacking Tor1a, Tor1aip1, and SUN1/2 as well as lamin A and B1 were derived from mice as previously described (Kim et al., 2010; Jung et al., 2014). All mouse MEFs used in this study were grown in DMEM with 15% BCS. Human fibroblasts (GM00023, GM00024, GM02912, GM02551, GM03208, GM03211, GM03221, and GM02304) were purchased from the Coriell Institute and cultured following vendor's instructions (Camden, NJ): GM00023, GM03208, GM03211, GM03221, GM02551 and GM02304 were grown in DMEM containing 15% fetal bovine serum (FBS) (Gemini Bio-Products, West Sacramento, CA). GM00024 were grown in DMEM supplemented with 10% FBS. GM02912 were grown in 20% FBS-containing Ham's F12 media supplemented with 2 mM L-glutamine (Sigma-Aldrich, St. Louis, MO).

2.2 Parallel microfiltration

Prior to filtration measurements, cells were washed with 1x DNase-, RNase- & Protease-free phosphate-buffered saline purchased from Mediatech (Manassas, VA), treated with trypsin (VWR, Visalia, CA), and resuspended in fresh medium to a density of 0.5 x 10^6 cells/mL. Cell

suspensions were then passed through a 35 μm cell strainer (BD Falcon, San Jose, CA) prior to each filtration measurement. Next, 350 μL of each cell suspension was loaded into each well of a 96-well loading plate (Greiner BioOne, Monroe, NC). The number and size distribution of cells in each well was quantified using an automated cell counter (TC20, BioRad Laboratories, Hercules, CA). Finally, a defined amount of air pressure, which was monitored using a 0 - 100 kPa pressure gauge (Noshok Inc., Berea, OH), was applied to the 96-well plate outfitted with a custom pressure chamber (Qi et al., 2015; Gill et al., 2017). To quantify retention volumes following filtration, we measured the absorbance at 560 nm of the phenol red-containing cell medium using a plate reader (Infinite M1000, Tecan Group Ltd., Männedorf, Switzerland).

2.3 q-DC

Standard soft lithography methods were used to fabricate the microfluidic devices for q-DC experiments. Briefly, a 10:1 w/w base to crosslinker ratio of polydimethylsiloxane (PDMS) was poured onto a previously described master wafer (Saunders et al., 2017). The device was subsequently bonded to a No. 1.5 glass coverslip (Thermo Fisher) using plasma treatment (Plasma Etch, Carson City, NV). Within 24 h of device fabrication, suspensions of 2×10^6 cells/mL were driven through constrictions of 9 μm (width) x 10 μm (height) by applying 55 kPa of air pressure across the device. We captured images of cell shape during transit through the 9 μm gaps on the millisecond timescale using a CMOS camera with a capture rate of 1600 frames/s (Vision Research, Wayne, NJ) mounted on an inverted Axiovert microscope (Zeiss, Oberkochen, Germany) equipped with a 20x/0.4NA objective (LD Achroplan 20x/0.4NA objective Korr Ph2, Zeiss) and light source (Osram Halogen Optic Lamp 100 W, 12 V). We used custom MATLAB (MathWorks, Natick, MA) code (https://github.com/knybe/RowatLab-DC-Analysis) to analyse the time-dependent shape and position changes of individual cells (Nyberg et al., 2016). To determine the mechanical stresses applied to individual cells, we used agarose calibration particles that were fabricated using oil-in-water emulsions as previously described (Nyberg et al., 2017). Stress-

strain curves were obtained for single cells and a power-law rheology model was subsequently fitted to the data to compute the elastic modulus and fluidity of the cells.

2.4 Epifluorescence microscopy

To image cell and nuclear morphology, cells grown on No. 1.5 coverslips were labeled with 5 μM Calcein-AM and 0.2 μg/mL Hoechst 33342 (ThermoFischer Scientific). For cell viability measurements, cells were stained with 50 μg/mL propidium iodide (Thermo Fisher Scientific). Images of fluorescently-labeled cells were acquired using a Zeiss Axio Observer A.1 microscope equipped with a 10x/0.3 NA EC Plan-Neofluar Ph1 M27 objective, 20x/0.8 NA Plan-Apochromat M27 objective, HBO 103W/2 mercury vapor short-arc lamp light source, BP 470/20 excitation filter, BP 505-530 emission filter, and FT 495 beam splitter. ImageJ (Bethesda, MA) was used to quantify cell and nuclear size and shape parameters from the acquired images.

2.5 Cell stretching

To subject cells to external mechanical stresses, we used a custom-built cell stretching apparatus (Kim et al., 2018). We prepared elastic PDMS membranes as previously described (Kim et al., 2018). Cells were resuspended in tissue culture media at a concentration of 5 x 10^5 cells/mL and then added to individual PDMS strips and incubated for 24 h at 37 °C in cell culture incubator. To quantify nuclear strain, the membranes with cells adhered were stretched by 2 mm (5% of the total length of the membrane) while submerged in cell culture media for 5 min prior to imaging. To determine effects of repetitive stretch on cell viability and adhesion, membranes were stretched by 2 mm at 0.5 Hz for 24 h at 37 °C. After 24 h, membrane-adhered cells were stained with fluorescent dyes and imaged as described above. To quantify the number of cells attached to the membranes after stretching, we prepared lysates of the adherent cells using a solution of 0.1 N NaOH (Sigma Aldrich) and measured the total protein content of the lysates using the BioRad Laboratories D-C protein assay kit.

2.6 Statistical methods

To determine statistical significance of data that exhibited non-parametric distributions including transit time, apparent cell elastic modulus, cell size, cell and nuclear shape, and nuclear strain, we used the Mann-Whitney U test. All other results are expressed as mean ± standard deviation and Student's t-test method was used to analyze significance and to obtain p-values.

3 Results

3.1 TorsinA and LAP1 contribute to fibroblast mechanotype

To begin to determine if DYT1 dystonia is associated with altered cellular mechanotype, we performed parallel microfiltration (PMF) (Qi et al., 2015; Gill et al., 2017) of NIH3T3 fibroblasts that have inhibited function of torsinA. In PMF, cell suspensions are filtered through porous membranes by applying air pressure. Cells that occlude the micron-scale pores due to their stiffness and/or size block the fluid flow, reducing filtrate volume, and increasing the volume of fluid that is retained in the top well, which we report as % retention (**Figure 1A**). To manipulate torsinA function, we generated lentivirus-transduced NIH3T3 fibroblasts that stably express previously described cDNA constructs encoding wild type (WT) or mutant (E171Q or ΔE) torsinA (Saunders et al., 2017). Since neither SS-EGFP-torsinA^{E171Q} nor SS-EGFP-torsinA$^{\Delta E}$ were able to rescue the rearward nuclear positioning defect in mouse embryonic fibroblasts (MEFs) isolated from torsinA-knockout (*Tor1a*$^{-/-}$) mice (Goodchild et al., 2005; Saunders et al., 2017), we rationalized that these constructs would act as dominant negative inhibitors of torsinA function in NIH3T3 fibroblasts. Consistent with this prediction, NIH3T3 fibroblasts expressing either SS-EGFP-torsinA^{E171Q} or SS-EGFP-torsinA$^{\Delta E}$ exhibited significantly lower % retention than parental non-transduced or SS-EGFP-torsinA^{WT} transduced NIH3T3 fibroblasts (**Figure 1B**). While cell size can impact filtration, we observed no significant differences in size distributions among these

cell lines (**Figure 1C**), suggesting that their altered filtration is due to differences in their cellular deformability. These data suggest that torsinA regulates the mechanotype of NIH3T3 fibroblasts.

To further investigate the relationship between torsinA and cellular mechanotype, we next performed PMF experiments on previously characterized *Tor1a*$^{+/+}$ and *Tor1a*$^{-/-}$ MEFs (Saunders et al., 2017). We found that % retention of the *Tor1a*$^{+/+}$ MEFs was significantly larger than the % retention of the *Tor1a*$^{-/-}$ MEFs (**Figure 1D**). Consistent with these findings, we observed that MEFs isolated from heterozygous (*Tor1a*$^{+/\Delta E}$) or homozygous (*Tor1a*$^{\Delta E/\Delta E}$) ΔE-knock-in mice (Goodchild et al., 2005) had a significantly lower % retention than *Tor1a*$^{+/+}$ MEFs (**Figure 1D**). Moreover, the % retention measured for MEFs derived from LAP1-knockout (*Tor1aip1*$^{-/-}$) mice was also significantly lower than control *Tor1aip1*$^{+/+}$ MEFs (**Figure 1F**). We confirmed that these observed changes in % retention were not due to significant differences in cell size distributions (**Figures 1E, G**). Because the interaction between torsinA and the luminal domain of LAP1 stimulates its ATPase activity *in vitro* (Zhao et al., 2013) and the ΔE mutation impairs the ability of torsinA to interact with LAP1 (Naismith et al., 2009), these results suggest that the interaction between torsinA and LAP1 may contribute to fibroblast mechanotype. In addition, LAP1 is critical for nuclear envelope structure (Santos et al., 2015) and interacts with nuclear lamins (Foisner and Gerace, 1993; Serrano et al., 2016), which are major determinants of cellular mechanotype (Houben et al., 2007). Thus, the loss of interaction between torsinA and LAP1 caused by the ΔE mutation may also contribute to the more compliant mechanotype that we observe in LAP1-knockout fibroblasts.

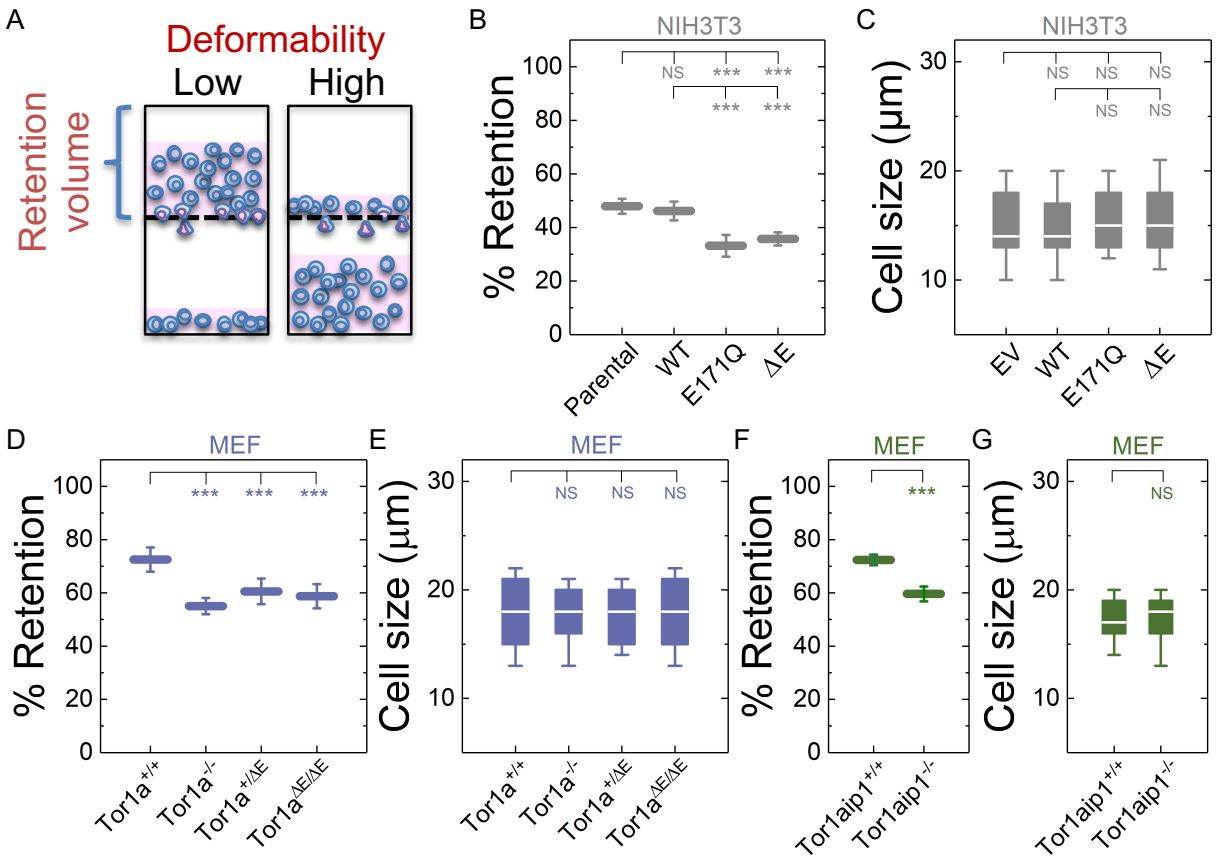

Figure 1. Fibroblasts lacking functional torsinA or LAP1 have increased deformability. (**A**) Schematic illustration of PMF. Less deformable cells tend to occlude pores, which blocks fluid flow and results in an increased volume of fluid that is retained above the membrane (% retention). (**B**) PMF measurements of NIH3T3 fibroblasts expressing the indicated SS-EGFP-tagged torsinA constructs. (**D, F**) PMF measurements of the indicated MEF lines. PMF conditions: 10 μm pore size, 2.1 kPa for 50 s. Each data point represents mean ± standard deviation (SD). Statistical significance was determined using the Student's t-test. (**C, E, G**) Cell size measurements. Boxplots show 25th and 75th percentiles; line shows median; and whiskers denote 10th and 90th percentiles. All data were obtained from three independent experiments. Statistical significance was determined using the Mann-Whitney U test. *** $p < 0.001$; ** $p < 0.01$; not significant (NS) $p > 0.05$.

3.2 Components of the LINC complex mediate cellular mechanotype

We previously showed that torsinA and LAP1 are both required for nuclear-cytoskeletal coupling through SUN2-containing LINC complexes (Saunders et al., 2017). Thus, we next asked whether or not MEFs isolated from SUN2-knockout (*SUN2*$^{-/-}$) mice (Lei et al., 2009) exhibit a similar decreased filtration as the *Tor1a*$^{-/-}$ and *Tor1aip1*$^{-/-}$ MEFs. We found that *SUN2*$^{-/-}$ MEFs had a

reduced % retention relative to control (*SUN1/2*$^{+/+}$) MEFs (**Figure 2A**). Since torsinA has also been proposed to interact with and regulate SUN1-containing LINC complexes (Jungwirth et al., 2011; Pappas et al., 2018), we also performed PMF on MEFs derived from SUN1/2-double knockout (*SUN1/2*$^{-/-}$) mice (Lei et al., 2009) and found that *SUN1/2*$^{-/-}$ MEFs had reduced retention compared to both *SUN2*$^{-/-}$ and *SUN1/2*$^{+/+}$ MEFs (**Figure 2A**). We confirmed that these changes in % retention were not due to significant differences in cell size distributions (**Figure 2B**).

We next investigated the effects of A-type lamins on cell filtration, as they are established regulators of cellular mechanotype (Lammerding et al., 2004; Swift et al., 2013) and directly interact with LAP1 (Foisner and Gerace, 1993; Serrano et al., 2016) and SUN1/2 (Chang et al., 2015b). We found that MEFs isolated from lamin A/C-knock-out (*LMNA*$^{-/-}$) mice exhibited a reduced % retention relative to MEFs isolated from control mice (*LMNA*$^{+/+}$) (**Figure 2C**). The increased deformability of the *LMNA*$^{-/-}$ MEFs that we observed is consistent with previous studies from our laboratory and others, which show that A-type lamins determine the ability of cells to deform through micron-scale pores, both during passive deformation driven by applied pressure (timescale ~ seconds) and active migration (timescale ~ hours) (Rowat et al., 2013; Denais et al., 2016; Irianto et al., 2017). In addition to A-type nuclear lamins, cells express the B-type nuclear lamins, lamin B1 and lamin B2 (Dittmer and Misteli, 2011; Reddy and Comai, 2016). Lamin B1 interacts with SUN1 (Nishioka et al., 2016) and LAP1 (Maison et al., 1997) and is required for proper nuclear-cytoskeletal coupling (Ji et al., 2007). We found that MEFs isolated from lamin-B1-knockout mice (*LMNB1*$^{-/-}$) (Vergnes et al., 2004) had reduced % retention compared to MEFs isolated from control mice (*LMNB1*$^{+/+}$) (**Figure 2C**), suggesting that lamin B1 also contributes to cellular mechanotype. These findings are in agreement with previous findings that lamin B1 is a determinant of nuclear shape and stiffness (Coffinier et al., 2011; Ferrera et al., 2014). While we observed differences in cell size distributions between *LMNA*$^{-/-}$ and *LMNA*$^{+/+}$ MEFs as well as between *LMNB1*$^{-/-}$ and *LMNB1*$^{+/+}$ MEFs, we did not observe that cells with larger median cell size

had increased % retention (**Figures 2C, D**). Taken together, these results suggest that nuclear lamins, torsinA, LAP1, and LINC complexes are important mediators of cellular mechanotype. These results are consistent with a model where cells are more deformable when the mechanical integration of the nucleus and the cytoskeleton is perturbed.

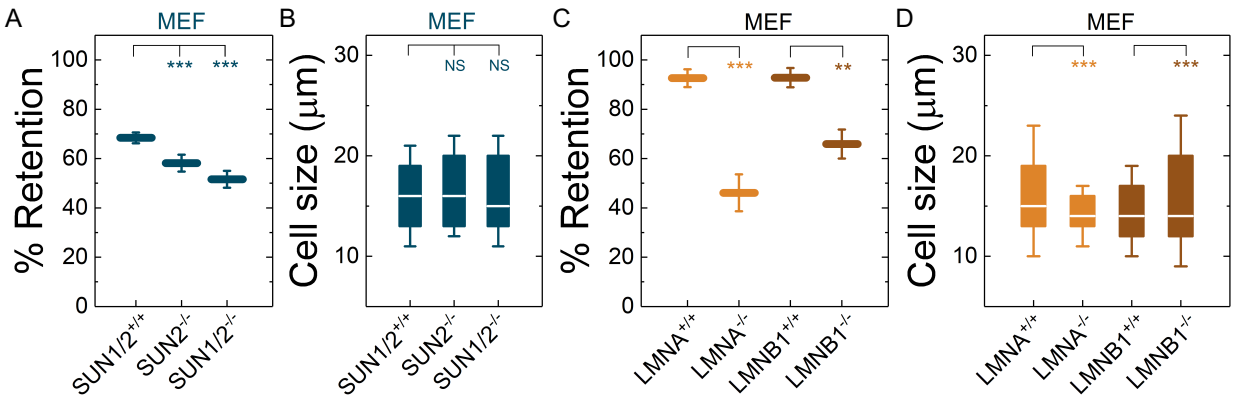

Figure 2. Fibroblasts lacking LINC complexes, A-type lamins, or lamin B1 have increased deformability. PMF measurements of the indicated MEF lines. (**A**) PMF conditions: 10 µm pore membrane, 2.1 kPa for 50 s. (**C**) PMF conditions: 10 µm pore membrane, 2.1 kPa for 40 s. Each data point represents mean ± SD. Statistical significance was determined using the Student's t-test. (**B, D**) Cell size data. Boxplots show 25th and 75th percentiles; line shows median; whiskers denote 10th and 90th percentiles. Statistical significance was determined using the Mann-Whitney U test. All data were obtained from three independent experiments. *** $p < 0.001$; ** $p < 0.01$; not significant (NS) $p > 0.05$.

3.3 Dystonia patient-derived fibroblasts are more deformable than controls

Having established that the DYT1 dystonia-causing ΔE mutation in torsinA makes cells more deformable and that torsinA and LINC complex-associated proteins are important determinants of cellular mechanotype, we next tested if fibroblasts isolated from DYT1 dystonia patients display defects in cellular mechanotype. We performed PMF on a panel of age-matched human fibroblasts isolated from normal control (GM00023, GM00024, GM02912) and DYT1 patients (GM03211, GM03221, GM02304). We found that DYT1 patient-derived fibroblasts had consistently lower % retention compared to fibroblasts isolated from unafflicted controls (**Figure**

3A). We did not observe any significant effects of cell size on retention measurements of these human fibroblasts. While there were some differences in cell size distributions across DYT1 fibroblast lines (**Figure 3B**), we consistently observed decreased % retention of the DYT1 dystonia patient-derived fibroblasts, even for the GM02304 line that has a larger median cell size (**Figure 3A**). These findings suggest that fibroblasts isolated from DYT1 dystonia patients more readily deform through micron-scale pores.

To validate the altered mechanotype of the DYT1 patient-derived fibroblasts (GM02304) *versus* control cells (GM00024), we used quantitative deformability cytometry (q-DC) (Nyberg et al., 2017). q-DC is a microfluidic method that enables single-cell measurements of transit time (*TT*), which is the time that it takes a cell to transit into the micron-scale constriction of a microfluidic device in response to applied pressure, and apparent elastic modulus (E_a). We found that DYT1 fibroblasts had reduced median *TT* relative to normal fibroblasts (median $TT_{GM02304}$ = 16.2 ms *versus* $TT_{GM00024}$ = 24.4 ms, p = 1.5 x 10^{-2}). Since *TT* tends to be shorter for more compliant cells with reduced elastic modulus (Nyberg et al., 2017), these findings corroborate the increased deformability of DYT1 fibroblasts (**Figures 3C, D**). q-DC measurements can also be impacted by cell size, but we found no significant correlations of q-DC measurements with cell diameter (*d*) by linear regression analysis (Pearson's $r_{GM02304\_TT \text{ vs } d}$ = 0.0, Pearson's $r_{GM00024\_TT \text{ vs } d}$ = -0.1), suggesting that these observations of the altered DYT1 dystonia-derived fibroblast mechanotype does not depend on cell size. Using power law rheology to extract measurements of E_a (Nyberg et al., 2017), we found that DYT1 patient-derived fibroblasts have reduced median E_a compared to controls, although the reduction was not statistically significant (**Figures 3E, F**). Collectively, our PMF and q-DC measurements indicate that DYT1 dystonia patient-derived fibroblasts are more deformable than control fibroblasts.

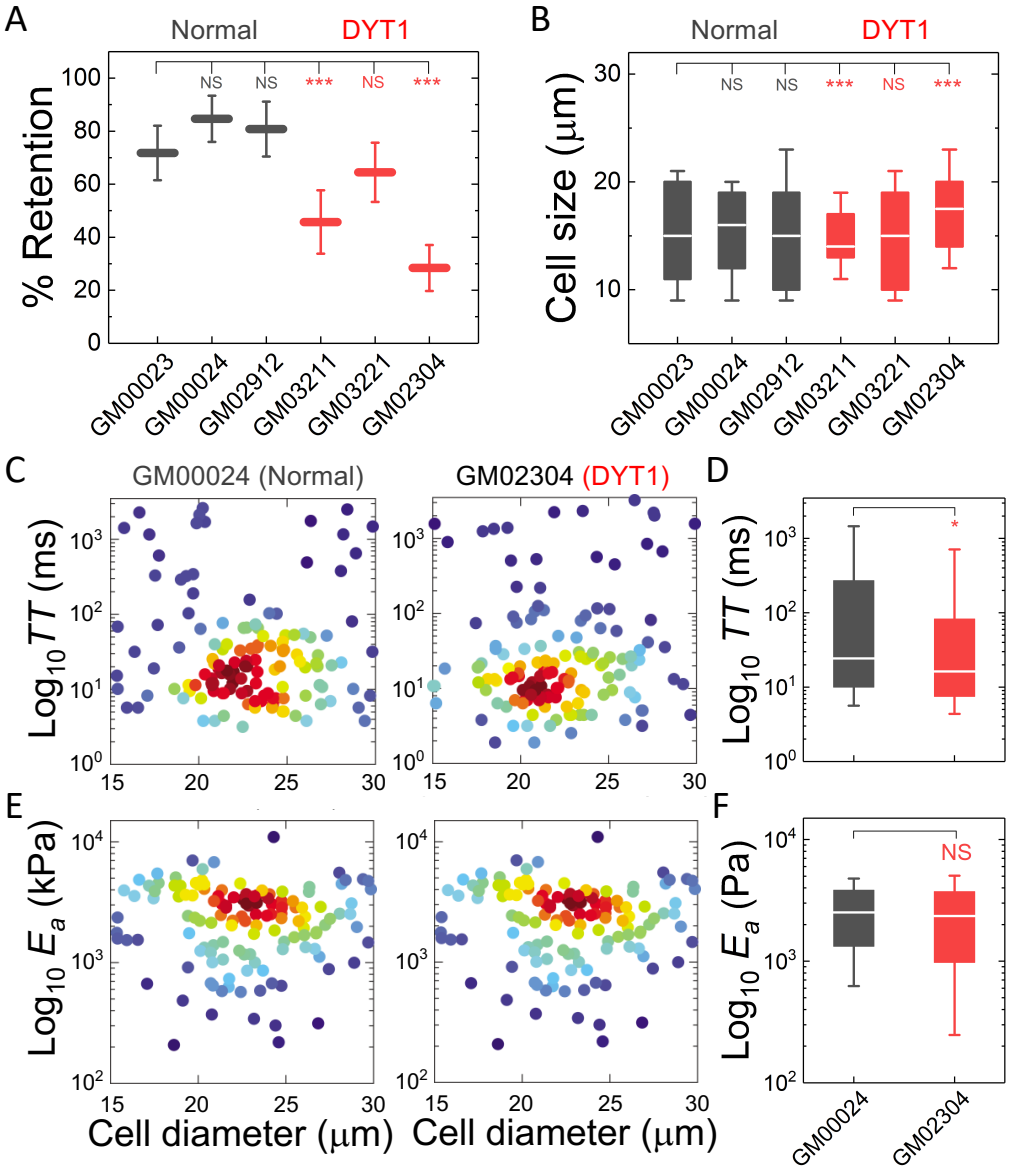

Figure 3. Dystonia patient-derived fibroblasts have increased deformability. (**A**) PMF measurements of normal and DYT1 patient-derived fibroblast lines. PMF conditions: 10 μm pore membrane, 1.4 kPa for 50 s. Each data point represents mean ± SD. Statistical significance was determined using the Student's t-test. (**B**) Cell size distributions. Boxplots show 25th and 75th percentiles; line shows median; whiskers denote 10th and 90th percentiles. (**C, E**) Density scatter plots for *TT* and E_a measurements determined by q-DC. Each dot represents a single cell. N > 190 per sample. (**D, F**) *TT* and E_a measurement boxplots show 25th and 75th percentiles; line shows median; whiskers denote 10th and 90th percentiles. Statistical significance was determined using Mann-Whitney U test. All data were obtained over three independent experiments. *** $p < 0.001$; ** $p < 0.01$; not significant (NS) $p > 0.05$.

3.4 DYT1 dystonia patient-derived fibroblasts display altered nuclear morphology

Cellular and nuclear shape reflect a balance between cell-matrix adhesion, cellular force generation, mechanical stability of the cellular cortex and nuclear envelope, as well as nuclear-cytoskeletal connectivity (Dahl et al., 2004; Dahl et al., 2008; Rowat et al., 2008; Kim et al., 2015; Murrell et al., 2015). Since the ΔE mutation in torsin A alters the mechanical integration of the nucleus and the cytoskeleton *via* the LINC complex (Nery et al., 2008; Jungwirth et al., 2011; Saunders et al., 2017), and we observed differences in cellular deformability between the DYT1 dystonia patient-derived fibroblasts and control fibroblasts, we hypothesized that fibroblasts isolated from DYT1 dystonia patients may exhibit altered cellular size as well as nuclear size and shape. To characterize these features, we performed quantitative image analysis of cells with labeled cytoplasm (Calcein AM) and nuclei (Hoechst) using epifluorescence microscopy. We first measured the area of adhered cells, which indicates the degree of cell spreading. Based on our observations of the more compliant mechanotype of DYT1 dystonia patient-derived fibroblasts and a previous report of the altered adhesion of these cells (Hewett et al., 2006), we hypothesized that DYT1 fibroblasts may have reduced spread area. However, we found no observable differences in cellular area between DYT1 and normal fibroblasts (**Supplementary Figure 1A**). Since intracellular forces pulling on the nucleus can result in an increased nuclear area (Iyer et al., 2012), we next measured the projected area of nuclei in these cells, but found no significant differences between fibroblasts isolated from DYT1 dystonia patients or controls (**Supplementary Figure 1B**). Cell-to-nuclear size ratio was also similar across cell types, indicating that nuclear and cellular size scale similarly in DYT1 dystonia patient-derived fibroblasts and control cells (**Supplementary Figure 1C**).

We next investigated nuclear shape, which is impacted by cytoskeletal-generated forces as well as the inherent mechanical stability of the nuclear envelope (Rowat et al., 2008; Makhija et al.,

2016). Given the altered physical connectivity between cytoskeleton and nucleus in DYT1 dystonia patient-derived fibroblasts, we reasoned that these cells may exhibit altered nuclear morphology. To quantify nuclear shape, we measured common metrics including aspect ratio and circularity. We found that nuclei in fibroblasts isolated from DYT1 dystonia patients have a slightly larger aspect ratio than normal fibroblast nuclei, reflecting how they are more elongated as compared to controls (**Figures 4A, B**). Consistent with this, we also found DYT1 dystonia patient-derived fibroblasts have an increased cellular aspect ratio compared to normal control fibroblasts (**Figures 4A, C**). We further investigated nuclear circularity; this shape parameter is sensitive to irregular shapes that deviate from a circle, as

$$C = 4\pi \frac{\text{Area}}{\text{Perimeter}^2}$$

and $C = 1$ for a perfect circle. However, we observed only minor differences in nuclear circularity between DYT1 dystonia patient-derived and normal fibroblasts (**Figure 4D**), which is consistent with the slightly elongated nuclear shapes that we observed in the fibroblasts isolated from DYT1 dystonia patients. Our findings that the DYT1 dystonia-causing ΔE mutation does not have a major impact on nuclear shape contrasts the known effects of reductions or mutations in A-type lamins (Rowat et al., 2013; Harada et al., 2014; Reis-Sobreiro et al., 2018), which are associated with nuclear blebbing, or lobulations, and tend to markedly reduce nuclear circularity (Funkhouser et al., 2013; Rowat et al., 2013; Reis-Sobreiro et al., 2018).

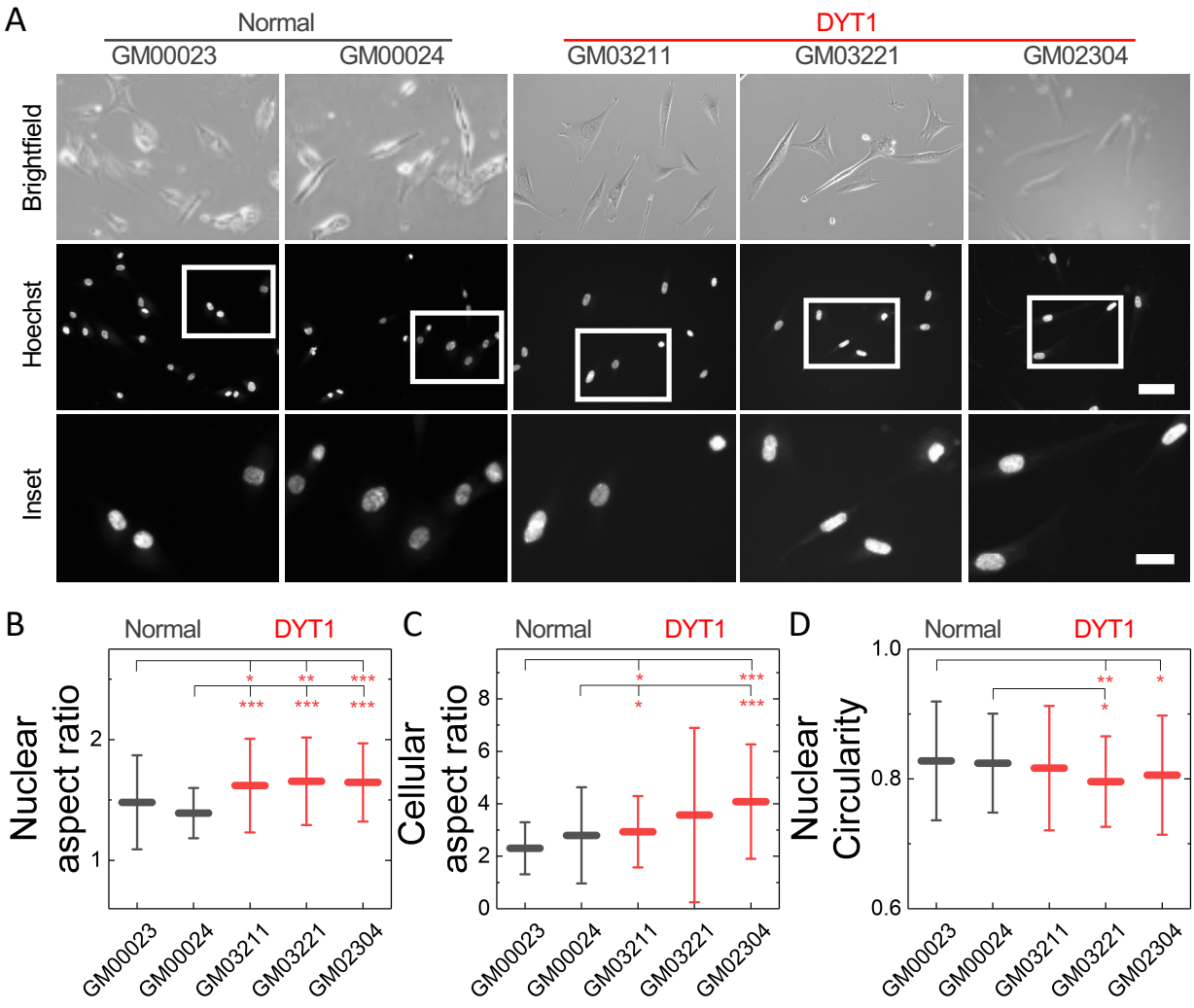

Figure 4. DYT1 patient-derived fibroblasts and nuclei are more elongated. (**A**) Representative brightfield and epifluorescence images of patient-derived normal and DYT1 fibroblasts (brightfield) and nuclei (Hoechst). Scale, 20 μm. Inset: Scale, 10 μm. Quantification of (**B**) nuclear aspect ratio, (**C**) cellular aspect ratio, and (**D**) nuclear circularity. Each data point represents mean ± SD. Data obtained from three independent experiments for N > 30 cells. Statistical significance was determined using Mann-Whitney U test. *** $p < 0.001$; ** $p < 0.01$; * $p < 0.05$; not significant (NS) $p > 0.05$ is not indicated on these plots for clarity.

3.5 DYT1 patient fibroblasts are more susceptible to damage following mechanical stretch

Nuclear lamins are critical for cell survival following exposure to physical forces, suggesting that the mechanical stability of the nucleus imparts protection from external mechanical stresses (Dahl

et al., 2004; Denais et al., 2016; Raab et al., 2016; Irianto et al., 2017; Chen et al., 2018; Kim et al., 2018). Since fibroblasts isolated from DYT1 dystonia patients are more deformable than controls, we next tested the hypothesis that DYT1 fibroblasts exhibit increased cell death following exposure to mechanical forces. To test this hypothesis, we grew DYT1 dystonia patient-derived fibroblasts (GM03211, GM02304) and normal controls (GM00023, GM00024) on an elastic collagen-coated PDMS membrane and subjected the resultant membrane with adhered cells to uniaxial mechanical stretch (5% strain). To quantify the magnitude of strain experienced by nuclei, we acquired images of cells in static and stretched conditions. We found that DYT1 dystonia patient-derived fibroblasts cells exhibited larger changes in nuclear area (strain) compared to control fibroblasts in response to the same magnitude of strain of the underlying substrate (**Figures 5A, B**). These observations of increased nuclear strain are consistent with the DYT1 fibroblast nuclei being more deformable than those in control fibroblasts. These findings also suggest that DYT1 dystonia fibroblast nuclei are deforming more in response to external mechanical stresses than control fibroblast nuclei despite the requirement of torsinA for nuclear-cytoskeletal coupling *via* the LINC complex (Saunders et al., 2017).

Since the mechanical stability of the nucleus is critical for cell survival following exposure to mechanical stresses (Harada et al., 2014; Denais et al., 2016; Raab et al., 2016; Irianto et al., 2017), we next determined the viability of DYT1 dystonia patient-derived and control fibroblasts after repeated cycles of stretch and relaxation at 5% strain and 0.5 Hz over 24 h. Visual inspection of fibroblasts in stretched *versus* static samples revealed major morphological differences between fibroblasts isolated from DYT1 dystonia patients compared to control cells after 24 h. In contrast to the aligned morphologies of control fibroblasts, which appear similar in both stretched and static samples, the stretched DYT1 fibroblasts were misaligned and exhibited irregular shapes (**Figure 5C**). To evaluate their viability after stretching, we acquired images of these cells stained with propidium iodide and used quantitative image analysis to count the number of dead

cells in each sample. While normal fibroblasts showed no significant cell death after stretching, we observed a marked 57-62% reduction in the viability of DYT1 fibroblasts compared to static control, indicating their reduced survival following exposure to mechanical stresses (**Figure 5D, Supplementary Figure 2**). Since the response of cells to stretch depends on cell-substrate adhesions, we also assessed the number of cells that remained adhered to the PDMS substrate after stretching by quantifying the total protein content of cells lysed from the PDMS membrane. We found a significant ~17-58% reduction in protein content for the stretched DYT1 cells relative to static control, showing that there was significant detachment of cells from the substrate over the 24 h stretching period. By contrast, over 90% of the control cells were adhered to the membrane after 24 h (**Figure 5E**). The increased detachment of DYT1 dystonia patient-derived fibroblasts is consistent with a previous report of altered integrin-mediated adhesion in these cells (Hewett et al., 2006; Kim et al., 2018). Collectively, these findings indicate a striking difference in the response of DYT1 dystonia patient-derived fibroblasts to mechanical stretch, which could be attributed to their reduced mechanical stability, altered mechanosensation, and/or impaired mechanosignaling. As molecular mediators of mechanotype are generally conserved across cell types (Chang et al., 2015a), we anticipate that our observations of altered mechanotype in human and mouse fibroblasts may also be observed in neurons, which may have important consequences for DYT1 dystonia pathogenesis.

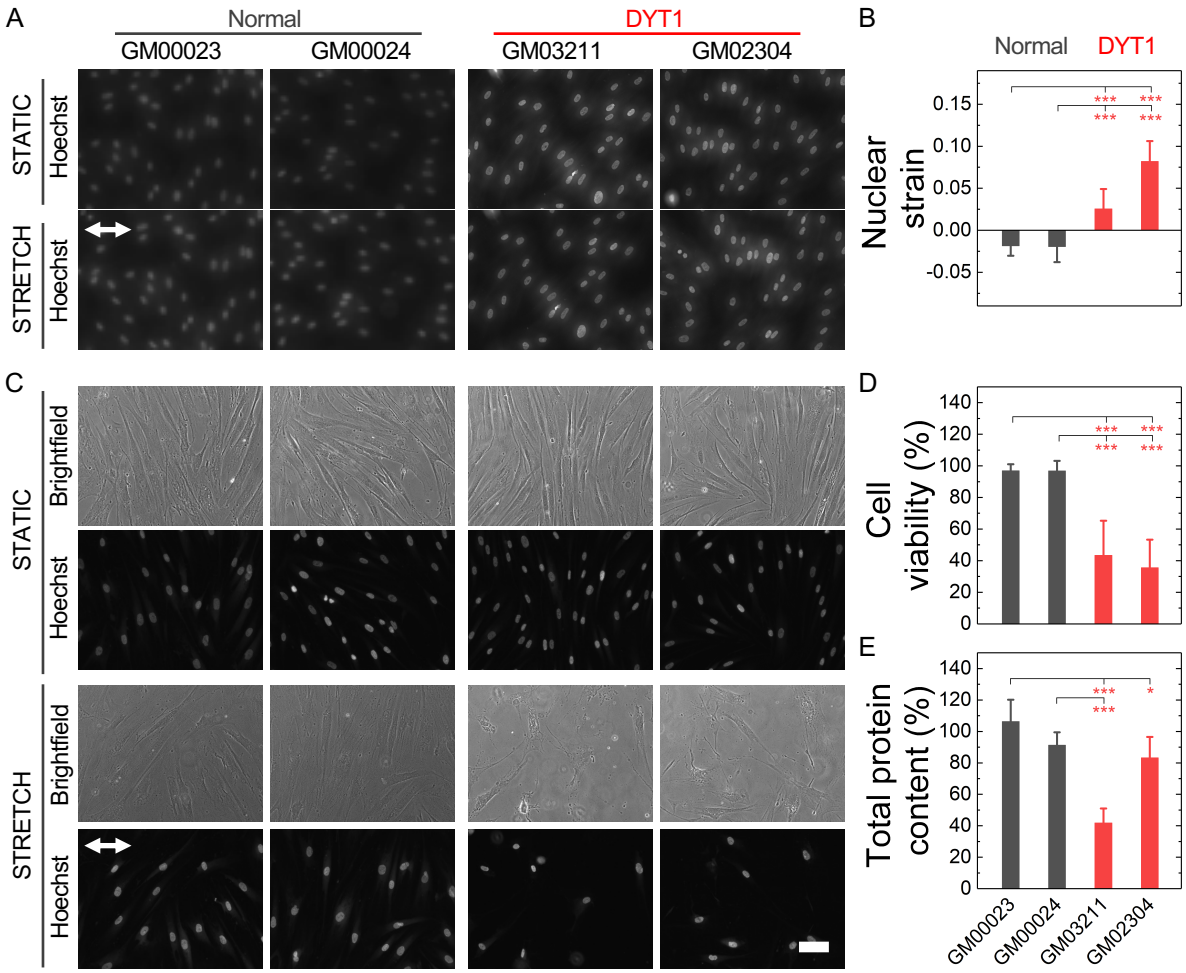

Figure 5. DYT1 patient-derived fibroblasts exhibit increased nuclear strain and are more susceptible to damage upon mechanical stretch. (**A**) Representative images of patient-derived normal and DYT1 fibroblasts stained with the nuclear dye Hoechst. Nuclear morphology was examined after cells were exposed to mechanical stretch (5% strain) for 5 min. Images show stretched (STRETCH) or non-stretched (STATIC) conditions. White arrow denotes direction of uniaxial stretch. (**B**) Quantification of nuclear strain (change in nuclear area) due to cell stretching. N > 15 cells. Statistical significance was determined using Mann-Whitney U test. (**C**) Representative images of patient-derived normal and DYT1 fibroblasts after exposure to 24 h cyclical stretch (5% strain) and static conditions. Cells were stained with Hoechst to visualize nuclei by fluorescence microscopy. Scale, 20 μm. (**D**) Cell viability of normal and DYT1 fibroblasts after exposure to stretch and static conditions. The viability data of stretched cells is normalized to static control for each cell line. N > 500 cells. (**E**) The percentage of cells that are adhered to the PDMS membranes after stretch is quantified by total protein content. Total protein content of stretched cells normalized to static control for each cell line. Each data point represents mean ± SD. Data obtained from two independent experiments. Scale, 20 μm. Statistical significance was determined using Student's t-test. *** $p < 0.001$; ** $p < 0.01$; * $p < 0.05$; and not significant (NS) $p > 0.05$ is not indicated on these plots for clarity.

4 Discussion

Here we show that DYT1 dystonia is characterized by defective cellular mechanobiology. We find that fibroblasts derived from DYT1 dystonia patients have a more compliant mechanotype than control fibroblasts. These findings are substantiated by the increased deformability of fibroblasts that are torsinA-null; that express torsinA ΔE; or that lack functional LINC complexes. It is intriguing to speculate how altered cellular mechanotype may impact DYT1 dystonia pathogenesis. Mechanotype is closely linked to cellular functions that involve physical force generation, such as motility, and mechanosensing (Anselme et al., 2018; Prahl and Odde, 2018), both of which are required during tissue morphogenesis where cells generate physical forces and sense mechanical cues (Heisenberg and Bellaiche, 2013; Pizzolo et al., 2017). Previous studies showed impaired migration of neurons in the dorsal forebrain of *Tor1a*$^{-/-}$ mouse embryos *in vivo* (McCarthy et al., 2012) and reduced motility of torsinA-null MEFs and DYT1 dystonia patient-derived fibroblasts *in vitro* (Nery et al., 2008; Nery et al., 2014). Our observations of the reduced survival of DYT1 dystonia-derived fibroblasts following mechanical stretch may also suggest that these cells have impaired mechanosensation. Like all cells, neurons adapt their own mechanotype by translating mechanical stimuli from their environment into biochemical signals through a process known as mechanotransduction (Tyler, 2012; Franze, 2013). During development, the brain exhibits evolving stiffness gradients due to the variations in the composition and architecture of the extracellular matrix (Franze, 2013; Barnes et al., 2017), which provide mechanical signals that instruct neuronal differentiation, proliferation, and survival (Iwashita et al., 2014; Koser et al., 2016). It is interesting to note that the brains of *Tor1a*$^{-/-}$ mice exhibit elevated LINC complex levels in the proliferative zone and an abnormal morphogenesis characterized by excess neural tissue (Dominguez Gonzalez et al., 2018). Since the brain morphogenesis phenotype observed in the *Tor1a*$^{-/-}$ mice was rescued by the SUN2-deletion (Dominguez Gonzalez et al., 2018), LINC complex regulation of mechanotype may be an

important consequence of torsinA activity during brain development in DYT1 dystonia. Taken together with the findings presented here, these results support the hypothesis that DYT1 dystonia may be characterized by defective mechanobiology.

Having established here that torsinA regulates cellular mechanotype and resistance to damage caused by mechanical forces, future efforts will focus on defining the underlying molecular mechanisms. Our findings are consistent with a model where torsinA, LINC complexes, and LINC complex-associated proteins each contribute to cellular mechanotype. Future molecular-level mechanotyping or imaging studies will define the extent to which protein-protein interactions between these structural components *versus* the individual proteins contributes to cellular and nuclear mechanical stability. Since many nuclear envelope proteins also interact with chromatin and regulate genomic organization (Van de Vosse et al., 2011; Zuleger et al., 2011), changes in gene expression may further impact mechanotype in DYT1 dystonia. Chromatin organization is also a determinant of cellular mechanotype (Pajerowski et al., 2007; Chalut et al., 2012; Schreiner et al., 2015; Stephens et al., 2017). Moreover, torsinA is implicated in other fundamental cellular functions including lipid metabolism and nuclear-cytoplasmic transport (Saunders and Luxton, 2016; Cascalho et al., 2017; Chase et al., 2017), which may also contribute to mechanotype. Identifying the elusive substrate(s) remodeled by torsinA within the contiguous lumen of the endoplasmic reticulum and nuclear envelope should provide further insight into the relative contribution of these torsinA-dependent processes to cellular mechanotype.

While torsinA is required for functional LINC complexes, which physically connect the nucleus and cytoskeleton (Chang et al., 2015a), it is interesting to note that DYT1 dystonia patient-derived fibroblasts exhibit increased nuclear strain following mechanical stretch, suggesting that there are still physical forces pulling on the nucleus during stretch of the underlying substrate. The increased nuclear strain may be explained by force transmission that is mediated by other protein-

protein interactions; for example, transmission of external forces to the nucleus could be regulated by microtubules (Alam et al., 2014; Chang et al., 2015a) and/or intermediate filaments, although the relationship between intermediate filaments and DYT1-causing torsinA mutations remains to be fully defined (Hewett et al., 2006; Nery et al., 2014; Saunders et al., 2017). The increased nuclear strain observed in DYT1 fibroblasts is consistent with the loss of torsinA function making the nuclear envelope more deformable, thus resulting in a larger increase in nuclear area for the same magnitude of substrate stretch. We additionally discovered that the altered mechanotype of DYT1 patient fibroblasts is associated with decreased survival following mechanical stretch. These findings are consistent with previous reports that reduced levels of lamin A/C in fibroblasts result in increased cell death following the migration of cells through narrow gaps (Wang et al., 2018). The decreased viability of DYT1 dystonia patient-derived fibroblasts could also result from increased nuclear rupture and double stranded DNA breaks that have been observed in fibroblasts as well as cancer and immune cells (Lammerding et al., 2005; Raab et al., 2016; Isermann and Lammerding, 2017); this resultant damage from mechanical stresses depends on lamin A/C expression levels, suggesting that the mechanical stability of the nuclear envelope is critical for cell survival. Our discovery of the reduced viability of DYT1 fibroblasts following mechanical stretch could also be explained by the altered apoptotic signaling that is triggered by mechanical stimuli (Raab et al., 2016). Future studies will investigate the mechanism of altered survival of DYT1 patient fibroblasts in more detail.

Finally, it is intriguing to speculate that defective mechanobiology may be a common cellular phenotype across different forms of dystonia. The shared disease mechanisms underlying the 25 other known inherited forms of dystonias remain poorly understood, but some evidence suggests altered mechanobiology may be implicated. For example, DYT2 dystonia is caused by an autosomal recessive mutation in the *HPCA* gene, which encodes the calcium-binding hippocalcin protein (Charlesworth et al., 2015) that is implicated in the regulation of the mechanoactive

extracellular signal-regulated kinase-mediated signal transduction (Huang and Ingber, 2005; Braunewell et al., 2009). Other known mutations that give rise to dystonia occur in proteins known to play a role in cellular/tissue mechanotype, including β4-tubulin, collagen-6A3, and sarcoglycan-ε (Verbeek and Gasser, 2016). For example, mutations in THAP1 (DYT6) and sarcoglycan-ε (DYT11) cause DYT6 and DYT11 dystonias; these proteins both interact with torsinA (Ledoux et al., 2013). Interestingly, torsinA and sarcoglycan-ε function together to promote proper neurological control over movement (Yokoi et al., 2010). Future studies will determine how broadly altered cellular mechanotype is conserved across different forms of dystonia. Such investigations could also shed light on how TBI can trigger dystonia symptoms, even for individuals that do not carry a known genetic mutation but may be predisposed to acquiring TBI-induced dystonia due to a mutation in another mechanoregulating gene. The motility of neurons is especially relevant in dystonia pathogenesis following TBI, where the directed migration of neurons and neural stem cells is essential for regeneration and repair (Ibrahim et al., 2016). The external mechanical stresses of TBI also result in cell death, which can have consequences for dystonia pathogenesis (Silver and Lux, 1994; Raghupathi, 2004). A deeper understanding of the mechanobiology of dystonia could further drive the discovery of novel therapeutic targets for treatment of this debilitating disease.

5 Abbreviations

AAA+: ATPase associated with various cellular activities

d: Cell diameter

E_a: Apparent cell elastic modulus

C: Circularity

LAP1: Lamina-associated polypeptide 1

LULL1: Luminal domain-like LAP1

LINC: Linkers of nucleoskeleton and cytoskeleton

MEF: Mouse embryonic fibroblast

PMF: Parallel microfiltration

q-DC: Quantitative deformability cytometry

SUN: Sad1/UNC-84

TAN: Transmembrane actin-associated nuclear

TT: Transit time

WT: Wild type

6 Supplementary Figures

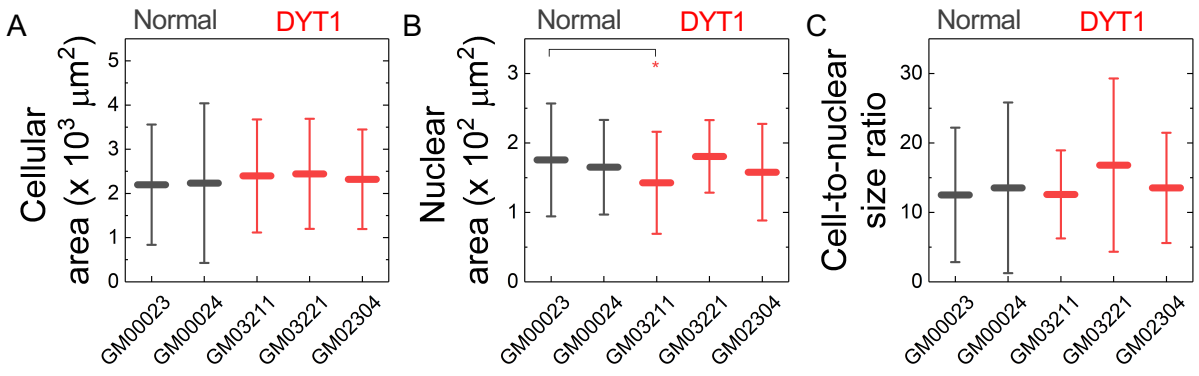

Supplementary Figure 1. Quantification of cell and nuclear area of normal and DYT1 fibroblasts. (**A**) Cellular area, (**B**) nuclear area and, (**C**) cell-to-nucleus area ratio for indicated patient-derived normal and DYT1 fibroblasts. Each data point represents mean ± SD. Data obtained from three independent experiments. Statistical significance was determined using Mann-Whitney U test and indicated where significant. * $p < 0.05$. Not significant (NS) $p > 0.05$ is not indicated on these plots for clarity.

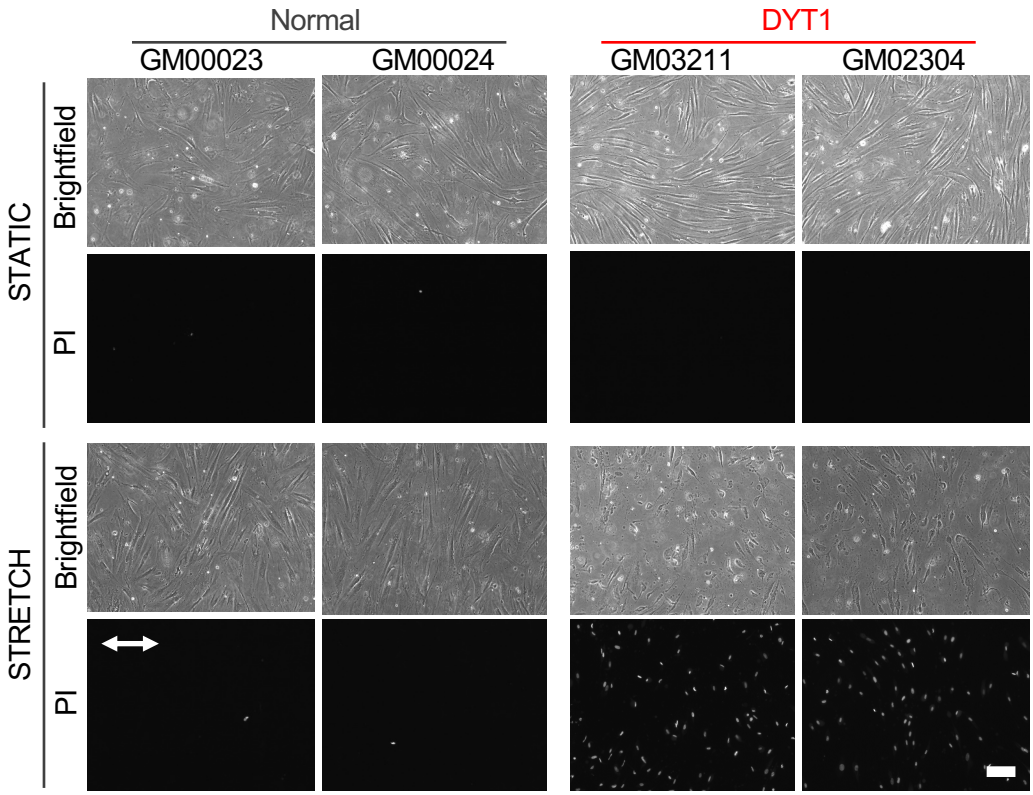

Supplementary Figure 2. DYT1 fibroblasts have reduced viability after mechanical stretching compared to normal fibroblasts. Representative images of PI-labeled cells, which indicate cell death, after stretching (stretch) compared to without mechanical stretching (static). White arrow shows the direction of uniaxial stretch. Scale, 100 μm.

7 References

Alam, S., Lovett, D.B., Dickinson, R.B., Roux, K.J., and Lele, T.P. (2014). Nuclear forces and cell mechanosensing. *Prog Mol Biol Transl Sci* 126**,** 205-215. doi: 10.1016/B978-0-12-394624-9.00008-7.

Albanese, A., Bhatia, K., Bressman, S., Delong, M., Fahn, S., Fung, V., et al. (2013). Phenomenology and classification of dystonia: a consensus update. *Mov Disord* 28(7)**,** 863-873. doi: 10.1002/mds.25475.

Albanese, A., Di Giovanni, M., and Lalli, S. (2018). Dystonia: diagnosis and management. *Eur J Neurol*. doi: 10.1111/ene.13762.

Anselme, K., Wakhloo, N.T., Rougerie, P., and Pieuchot, L. (2018). Role of the Nucleus as a Sensor of Cell Environment Topography. *Adv Healthc Mater* 7(8), e1701154. doi: 10.1002/adhm.201701154.

Auburger, G., Klinkenberg, M., Drost, J., Marcus, K., Morales-Gordo, B., Kunz, W.S., et al. (2012). Primary skin fibroblasts as a model of Parkinson's disease. *Mol Neurobiol* 46(1), 20-27. doi: 10.1007/s12035-012-8245-1.

Barnes, J., Przybyla, L., and Weaver, V. (2017). Tissue mechanics regulate brain development, homeostasis and disease. *J Cell Sci* 130(1), 71-82. doi: 10.1242/jcs.191742.

Braunewell, K., Klein-Szanto, A., and Szanto, A. (2009). Visinin-like proteins (VSNLs): interaction partners and emerging functions in signal transduction of a subfamily of neuronal Ca2+ -sensor proteins. *Cell Tissue Res* 335(2), 301-316. doi: 10.1007/s00441-008-0716-3.

Burbulla, L.F., and Kruger, R. (2012). The use of primary human fibroblasts for monitoring mitochondrial phenotypes in the field of Parkinson's disease. *J Vis Exp* (68). doi: 10.3791/4228.

Cascalho, A., Jacquemyn, J., and Goodchild, R. (2017). Membrane defects and genetic redundancy: Are we at a turning point for DYT1 dystonia. *Mov Disord* 32(3), 371-381. doi: 10.1002/mds.26880

Chalut, K.J., Hopfler, M., Lautenschlager, F., Boyde, L., Chan, C.J., Ekpenyong, A., et al. (2012). Chromatin decondensation and nuclear softening accompany Nanog downregulation in embryonic stem cells. *Biophys J* 103(10), 2060-2070. doi: 10.1016/j.bpj.2012.10.015.

Chang, W., Antoku, S., Östlund, C., Worman, H., and Gundersen, G. (2015a). Linker of nucleoskeleton and cytoskeleton (LINC) complex-mediated actin-dependent nuclear positioning orients centrosomes in migrating myoblasts. *Nucleus* 6(1), 77-88. doi: 10.1080/19491034.2015.1004947.

Chang, W., Worman, H., and Gundersen, G. (2015b). Accessorizing and anchoring the LINC complex for multifunctionality. *J Cell Biol* 208(1), 11-22. doi: 10.1083/jcb.201409047.

Charlesworth, G., Angelova, P., Bartolomé-Robledo, F., Ryten, M., Trabzuni, D., Stamelou, M., et al. (2015). Mutations in HPCA cause autosomal-recessive primary isolated dystonia. *Am J Hum Genet* 96(4), 657-665. doi: 10.1016/j.ajhg.2015.02.007.

Chase, A., Laudermilch, E., and Schlieker, C. (2017). Torsin ATPases: Harnessing Dynamic Instability for Function. *Front Mol Biosci* 4, 29. doi: 10.3389/fmolb.2017.00029

Chen, N.Y., Kim, P., Weston, T.A., Edillo, L., Tu, Y., Fong, L.G., et al. (2018). Fibroblasts lacking nuclear lamins do not have nuclear blebs or protrusions but nevertheless have frequent nuclear membrane ruptures. *Proc Natl Acad Sci U S A* 115(40), 10100-10105. doi: 10.1073/pnas.1812622115.

Coffinier, C., Jung, H.J., Nobumori, C., Chang, S., Tu, Y., Barnes, R.H., 2nd, et al. (2011). Deficiencies in lamin B1 and lamin B2 cause neurodevelopmental defects and distinct nuclear shape abnormalities in neurons. *Mol Biol Cell* 22(23), 4683-4693. doi: 10.1091/mbc.E11-06-0504.

Connolly, G.P. (1998). Fibroblast models of neurological disorders: fluorescence measurement studies. *Trends Pharmacol Sci* 19(5), 171-177.

Crisp, M., Liu, Q., Roux, K., Rattner, J., Shanahan, C., Burke, B., et al. (2006). Coupling of the nucleus and cytoplasm: role of the LINC complex. *J Cell Biol* 172(1), 41-53. doi: 10.1083/jcb.200509124.

Dahl, K.N., Kahn, S.M., Wilson, K.L., and Discher, D.E. (2004). The nuclear envelope lamina network has elasticity and a compressibility limit suggestive of a molecular shock absorber. *J Cell Sci* 117(Pt 20), 4779-4786. doi: 10.1242/jcs.01357.

Dahl, K.N., Ribeiro, A.J., and Lammerding, J. (2008). Nuclear shape, mechanics, and mechanotransduction. *Circ Res* 102(11), 1307-1318. doi: 10.1161/CIRCRESAHA.108.173989.

Defazio, G., Berardelli, A., and Hallett, M. (2007). Do primary adult-onset focal dystonias share aetiological factors. *Brain* 130(Pt 5), 1183-1193. doi: 10.1093/brain/awl355.

Denais, C., Gilbert, R., Isermann, P., McGregor, A., te Lindert, M., Weigelin, B., et al. (2016). Nuclear envelope rupture and repair during cancer cell migration. *Science* 352(6283), 353-358. doi: 10.1126/science.aad7297.

Dittmer, T., and Misteli, T. (2011). The lamin protein family. *Genome Biol* 12(5), 222. doi: 10.1186/gb-2011-12-5-222.

Dominguez Gonzalez, B., Billion, K., Rous, S., Pavie, B., Lange, C., and Goodchild, R. (2018). Excess LINC complexes impair brain morphogenesis in a mouse model of recessive TOR1A disease. *Hum Mol Genet* 27(12), 2154-2170. doi: 10.1093/hmg/ddy125.

Fahn, S. (1988). Concept and classification of dystonia. *Adv Neurol* 50, 1-8.

Fahn, S., Marsden, C., and Caine, D. (1988). Dystonia 2. Proceedings of the Second International Symposium on Torsion Dystonia. Harriman, New York, 1986. *Adv Neurol* 50, 1-705.

Ferrera, D., Canale, C., Marotta, R., Mazzaro, N., Gritti, M., Mazzanti, M., et al. (2014). Lamin B1 overexpression increases nuclear rigidity in autosomal dominant leukodystrophy fibroblasts. *FASEB J* 28(9), 3906-3918. doi: 10.1096/fj.13-247635.

Foisner, R., and Gerace, L. (1993). Integral membrane proteins of the nuclear envelope interact with lamins and chromosomes, and binding is modulated by mitotic phosphorylation. *Cell* 73(7), 1267-1279.

Franze, K. (2013). The mechanical control of nervous system development. *Development* 140(15), 3069-3077. doi: 10.1242/dev.079145.

Funkhouser, C.M., Sknepnek, R., Shimi, T., Goldman, A.E., Goldman, R.D., and Olvera de la Cruz, M. (2013). Mechanical model of blebbing in nuclear lamin meshworks. *Proc Natl Acad Sci U S A* 110(9), 3248-3253. doi: 10.1073/pnas.1300215110.

Ganos, C., Edwards, M., and Bhatia, K. (2016). Posttraumatic functional movement disorders. *Handb Clin Neurol* 139, 499-507. doi: 10.1016/B978-0-12-801772-2.00041-2.

Geyer, H., and Bressman, S. (2006). The diagnosis of dystonia. *Lancet Neurol* 5(9), 780-790. doi: 10.1016/S1474-4422(06)70547-6.

Gill, N.K., Qi, D., Kim, T.-H., Chan, C., Nguyen, A., Nyberg, K.D., et al. (2017). *A protocol for screening cells based on deformability using parallel microfiltration*.

Goodchild, R., Kim, C., and Dauer, W. (2005). Loss of the dystonia-associated protein torsinA selectively disrupts the neuronal nuclear envelope. *Neuron* 48(6), 923-932. doi: 10.1016/j.neuron.2005.11.010.

Goodchild, R.E., and Dauer, W.T. (2004). Mislocalization to the nuclear envelope: an effect of the dystonia-causing torsinA mutation. *Proc Natl Acad Sci U S A* 101(3), 847-852. doi: 10.1073/pnas.0304375101.

Hanson, P., and Whiteheart, S. (2005). AAA+ proteins: have engine, will work. *Nat Rev Mol Cell Biol* 6(7), 519-529. doi: 10.1038/nrm1684.

Harada, T., Swift, J., Irianto, J., Shin, J.W., Spinler, K.R., Athirasala, A., et al. (2014). Nuclear lamin stiffness is a barrier to 3D migration, but softness can limit survival. *J Cell Biol* 204(5), 669-682. doi: 10.1083/jcb.201308029.

Heisenberg, C.P., and Bellaiche, Y. (2013). Forces in tissue morphogenesis and patterning. *Cell* 153(5), 948-962. doi: 10.1016/j.cell.2013.05.008.

Hewett, J.W., Zeng, J., Niland, B.P., Bragg, D.C., and Breakefield, X.O. (2006). Dystonia-causing mutant torsinA inhibits cell adhesion and neurite extension through interference with cytoskeletal dynamics. *Neurobiol Dis* 22(1), 98-111. doi: 10.1016/j.nbd.2005.10.012.

Hiebert, J., Shen, Q., Thimmesch, A., and Pierce, J. (2015). Traumatic brain injury and mitochondrial dysfunction. *Am J Med Sci* 350(2), 132-138. doi: 10.1097/MAJ.0000000000000506.

Houben, F., Ramaekers, F.C., Snoeckx, L.H., and Broers, J.L. (2007). Role of nuclear lamina-cytoskeleton interactions in the maintenance of cellular strength. *Biochim Biophys Acta* 1773(5), 675-686. doi: 10.1016/j.bbamcr.2006.09.018.

Hsieh, M., and Nguyen, H. (2005). Molecular mechanism of apoptosis induced by mechanical forces. *Int Rev Cytol* 245, 45-90. doi: 10.1016/S0074-7696(05)45003-2.

Huang, S., and Ingber, D. (2005). Cell tension, matrix mechanics, and cancer development. *Cancer Cell* 8(3), 175-176. doi: 10.1016/j.ccr.2005.08.009.

Ibrahim, S., Hu, W., Wang, X., Gao, X., He, C., and Chen, J. (2016). Traumatic Brain Injury Causes Aberrant Migration of Adult-Born Neurons in the Hippocampus. *Sci Rep* 6, 21793. doi: 10.1038/srep21793.

Irianto, J., Xia, Y., Pfeifer, C., Athirasala, A., Ji, J., Alvey, C., et al. (2017). DNA Damage Follows Repair Factor Depletion and Portends Genome Variation in Cancer Cells after Pore Migration. *Curr Biol* 27(2), 210-223. doi: 10.1016/j.cub.2016.11.049.

Isermann, P., and Lammerding, J. (2017). Consequences of a tight squeeze: Nuclear envelope rupture and repair. *Nucleus* 8(3), 268-274. doi: 10.1080/19491034.2017.1292191.

Iwashita, M., Kataoka, N., Toida, K., and Kosodo, Y. (2014). Systematic profiling of spatiotemporal tissue and cellular stiffness in the developing brain. *Development* 141(19), 3793-3798. doi: 10.1242/dev.109637.

Iyer, K.V., Pulford, S., Mogilner, A., and Shivashankar, G.V. (2012). Mechanical activation of cells induces chromatin remodeling preceding MKL nuclear transport. *Biophys J* 103(7), 1416-1428. doi: 10.1016/j.bpj.2012.08.041.

Ji, J., Lee, R., Vergnes, L., Fong, L., Stewart, C., Reue, K., et al. (2007). Cell nuclei spin in the absence of lamin b1. *J Biol Chem* 282(27), 20015-20026. doi: 10.1074/jbc.M611094200.

Jung, H.J., Tatar, A., Tu, Y., Nobumori, C., Yang, S.H., Goulbourne, C.N., et al. (2014). An absence of nuclear lamins in keratinocytes leads to ichthyosis, defective epidermal barrier function, and intrusion of nuclear membranes and endoplasmic reticulum into the nuclear chromatin. *Mol Cell Biol* 34(24), 4534-4544. doi: 10.1128/MCB.00997-14.

Jungwirth, M., Kumar, D., Jeong, D., and Goodchild, R. (2011). The nuclear envelope localization of DYT1 dystonia torsinA-ΔE requires the SUN1 LINC complex component. *BMC Cell Biol* 12, 24. doi: 10.1186/1471-2121-12-24

Kaminski, A., Fedorchak, G., and Lammerding, J. (2014). The cellular mastermind(?)-mechanotransduction and the nucleus. *Prog Mol Biol Transl Sci* 126**,** 157-203. doi: 10.1016/B978-0-12-394624-9.00007-5.

Kim, C., Perez, A., Perkins, G., Ellisman, M., and Dauer, W. (2010). A molecular mechanism underlying the neural-specific defect in torsinA mutant mice. *Proc Natl Acad Sci U S A* 107(21)**,** 9861-9866. doi: 10.1073/pnas.0912877107.

Kim, D.H., Li, B., Si, F., Phillip, J.M., Wirtz, D., and Sun, S.X. (2015). Volume regulation and shape bifurcation in the cell nucleus. *J Cell Sci* 128(18)**,** 3375-3385. doi: 10.1242/jcs.166330.

Kim, P.H., Luu, J., Heizer, P., Tu, Y., Weston, T.A., Chen, N., et al. (2018). Disrupting the LINC complex in smooth muscle cells reduces aortic disease in a mouse model of Hutchinson-Gilford progeria syndrome. *Sci Transl Med* 10(460). doi: 10.1126/scitranslmed.aat7163.

Koser, D., Thompson, A., Foster, S., Dwivedy, A., Pillai, E., Sheridan, G., et al. (2016). Mechanosensing is critical for axon growth in the developing brain. *Nat Neurosci* 19(12)**,** 1592-1598. doi: 10.1038/nn.4394

Lammerding, J., Hsiao, J., Schulze, P., Kozlov, S., Stewart, C., and Lee, R. (2005). Abnormal nuclear shape and impaired mechanotransduction in emerin-deficient cells. *J Cell Biol* 170(5)**,** 781-791. doi: 10.1083/jcb.200502148.

Lammerding, J., Schulze, P., Takahashi, T., Kozlov, S., Sullivan, T., Kamm, R., et al. (2004). Lamin A/C deficiency causes defective nuclear mechanics and mechanotransduction. *J Clin Invest* 113(3)**,** 370-378. doi: 10.1172/JCI19670

Laudermilch, E., and Schlieker, C. (2016). Torsin ATPases: structural insights and functional perspectives. *Curr Opin Cell Biol* 40**,** 1-7. doi: 10.1016/j.ceb.2016.01.001

Ledoux, M.S., Dauer, W.T., and Warner, T.T. (2013). Emerging common molecular pathways for primary dystonia. *Mov Disord* 28(7)**,** 968-981. doi: 10.1002/mds.25547.

Lei, K., Zhang, X., Ding, X., Guo, X., Chen, M., Zhu, B., et al. (2009). SUN1 and SUN2 play critical but partially redundant roles in anchoring nuclei in skeletal muscle cells in mice. *Proc Natl Acad Sci U S A* 106(25), 10207-10212. doi: 10.1073/pnas.0812037106.

Lombardi, M., Jaalouk, D., Shanahan, C., Burke, B., Roux, K., and Lammerding, J. (2011). The interaction between nesprins and sun proteins at the nuclear envelope is critical for force transmission between the nucleus and cytoskeleton. *J Biol Chem* 286(30), 26743-26753. doi: 10.1074/jbc.M111.233700.

Luxton, G., Gomes, E., Folker, E., Vintinner, E., and Gundersen, G. (2010). Linear arrays of nuclear envelope proteins harness retrograde actin flow for nuclear movement. *Science* 329(5994), 956-959. doi: 10.1126/science.1189072.

Luxton, G., Gomes, E., Folker, E., Worman, H., and Gundersen, G. (2011). TAN lines: a novel nuclear envelope structure involved in nuclear positioning. *Nucleus* 2(3), 173-181. doi: 10.4161/nucl.2.3.16243

Maison, C., Pyrpasopoulou, A., Theodoropoulos, P.A., and Georgatos, S.D. (1997). The inner nuclear membrane protein LAP1 forms a native complex with B-type lamins and partitions with spindle-associated mitotic vesicles. *EMBO J* 16(16), 4839-4850. doi: 10.1093/emboj/16.16.4839.

Makhija, E., Jokhun, D.S., and Shivashankar, G.V. (2016). Nuclear deformability and telomere dynamics are regulated by cell geometric constraints. *Proc Natl Acad Sci U S A* 113(1), E32-40. doi: 10.1073/pnas.1513189113.

McCarthy, D.M., Gioioso, V., Zhang, X., Sharma, N., and Bhide, P.G. (2012). Neurogenesis and neuronal migration in the forebrain of the TorsinA knockout mouse embryo. *Dev Neurosci* 34(4), 366-378. doi: 10.1159/000342260.

Murrell, M., Oakes, P.W., Lenz, M., and Gardel, M.L. (2015). Forcing cells into shape: the mechanics of actomyosin contractility. *Nat Rev Mol Cell Biol* 16(8), 486-498. doi: 10.1038/nrm4012.

Naismith, T., Dalal, S., and Hanson, P. (2009). Interaction of torsinA with its major binding partners is impaired by the dystonia-associated DeltaGAG deletion. *J Biol Chem* 284(41)**,** 27866-27874. doi: 10.1074/jbc.M109.020164.

Naismith, T.V., Heuser, J.E., Breakefield, X.O., and Hanson, P.I. (2004). TorsinA in the nuclear envelope. *Proc Natl Acad Sci U S A* 101(20)**,** 7612-7617. doi: 10.1073/pnas.0308760101.

Nery, F., Zeng, J., Niland, B., Hewett, J., Farley, J., Irimia, D., et al. (2008). TorsinA binds the KASH domain of nesprins and participates in linkage between nuclear envelope and cytoskeleton. *J Cell Sci* 121(Pt 20)**,** 3476-3486. doi: 10.1242/jcs.029454.

Nery, F.C., Atai, N.A., da Hora, C.C., Kim, E.Y., Hettich, J., Mempel, T.R., et al. (2014). Microfluidic platform to evaluate migration of cells from patients with DYT1 dystonia. *J Neurosci Methods* 232**,** 181-188. doi: 10.1016/j.jneumeth.2014.05.027.

Nishioka, Y., Imaizumi, H., Imada, J., Katahira, J., Matsuura, N., and Hieda, M. (2016). SUN1 splice variants, SUN1_888, SUN1_785, and predominant SUN1_916, variably function in directional cell migration. *Nucleus* 7(6)**,** 572-584. doi: 10.1080/19491034.2016.1260802.

Nyberg, K., Hu, K., Kleinman, S., Khismatullin, D., Butte, M., and Rowat, A. (2017). Quantitative Deformability Cytometry: Rapid, Calibrated Measurements of Cell Mechanical Properties. *Biophys J* 113(7)**,** 1574-1584. doi: 10.1016/j.bpj.2017.06.073.

Nyberg, K.D., Scott, M.B., Bruce, S.L., Gopinath, A.B., Bikos, D., Mason, T.G., et al. (2016). The physical origins of transit time measurements for rapid, single cell mechanotyping. *Lab Chip* 16(17)**,** 3330-3339. doi: 10.1039/c6lc00169f.

Ozelius, L., Hewett, J., Page, C., Bressman, S., Kramer, P., Shalish, C., et al. (1997). The early-onset torsion dystonia gene (DYT1) encodes an ATP-binding protein. *Nat Genet* 17(1)**,** 40-48. doi: 10.1038/ng0997-40.

Pajerowski, J.D., Dahl, K.N., Zhong, F.L., Sammak, P.J., and Discher, D.E. (2007). Physical plasticity of the nucleus in stem cell differentiation. *Proc Natl Acad Sci U S A* 104(40)**,** 15619-15624. doi: 10.1073/pnas.0702576104.

Pappas, S., Liang, C., Kim, S., Rivera, C., and Dauer, W. (2018). TorsinA dysfunction causes persistent neuronal nuclear pore defects. *Hum Mol Genet* 27(3), 407-420. doi: 10.1093/hmg/ddx405.

Pizzolo, F., Salvagno, G., Caruso, B., Cocco, C., Zorzi, F., Zaltron, C., et al. (2017). Fully automated chemiluminescence vs RIA aldosterone assay in primary aldosteronism work-up. *J Hum Hypertens* 31(12), 826-830. doi: 10.1038/jhh.2017.62.

Prahl, L.S., and Odde, D.J. (2018). Modeling Cell Migration Mechanics. *Adv Exp Med Biol* 1092, 159-187. doi: 10.1007/978-3-319-95294-9_9.

Qi, D., Kaur Gill, N., Santiskulvong, C., Sifuentes, J., Dorigo, O., Rao, J., et al. (2015). Screening cell mechanotype by parallel microfiltration. *Sci Rep* 5, 17595. doi: 10.1038/srep17595.

Raab, M., Gentili, M., de Belly, H., Thiam, H., Vargas, P., Jimenez, A., et al. (2016). ESCRT III repairs nuclear envelope ruptures during cell migration to limit DNA damage and cell death. *Science* 352(6283), 359-362. doi: 10.1126/science.aad7611.

Raghupathi, R. (2004). Cell death mechanisms following traumatic brain injury. *Brain Pathol* 14(2), 215-222.

Reddy, S., and Comai, L. (2016). Recent advances in understanding the role of lamins in health and disease. *F1000Res* 5, 2536. doi: 10.12688/f1000research.9260.1.

Reis-Sobreiro, M., Chen, J., Novitskaya, T., You, S., Morley, S., Steadman, K., et al. (2018). Emerin deregulation links nuclear shape instability to metastatic potential. *Cancer Res*. doi: 10.1158/0008-5472.CAN-18-0608.

Rowat, A., Jaalouk, D., Zwerger, M., Ung, W., Eydelnant, I., Olins, D., et al. (2013). Nuclear envelope composition determines the ability of neutrophil-type cells to passage through micron-scale constrictions. *J Biol Chem* 288(12), 8610-8618. doi: 10.1074/jbc.M112.441535.

Rowat, A., Lammerding, J., and Ipsen, J. (2006). Mechanical properties of the cell nucleus and the effect of emerin deficiency. *Biophys J* 91(12), 4649-4664. doi: 10.1529/biophysj.106.086454.

Rowat, A.C., Lammerding, J., Herrmann, H., and Aebi, U. (2008). Towards an integrated understanding of the structure and mechanics of the cell nucleus. *Bioessays* 30(3), 226-236. doi: 10.1002/bies.20720.

Santos, M., Costa, P., Martins, F., da Cruz e Silva, E.F., da Cruz e Silva, O.A., and Rebelo, S. (2015). LAP1 is a crucial protein for the maintenance of the nuclear envelope structure and cell cycle progression. *Mol Cell Biochem* 399(1-2), 143-153. doi: 10.1007/s11010-014-2241-x.

Saunders, C., Harris, N., Willey, P., Woolums, B., Wang, Y., McQuown, A., et al. (2017). TorsinA controls TAN line assembly and the retrograde flow of dorsal perinuclear actin cables during rearward nuclear movement. *J Cell Biol* 216(3), 657-674. doi: 10.1083/jcb.201507113

Saunders, C., and Luxton, G. (2016). LINCing defective nuclear-cytoskeletal coupling and DYT1 dystonia. *Cell Mol Bioeng* 9(2), 207-216. doi: 10.1007/s12195-016-0432-0

Schreiner, S.M., Koo, P.K., Zhao, Y., Mochrie, S.G., and King, M.C. (2015). The tethering of chromatin to the nuclear envelope supports nuclear mechanics. *Nat Commun* 6, 7159. doi: 10.1038/ncomms8159.

Serrano, J.B., da Cruz, E.S.O.A., and Rebelo, S. (2016). Lamina Associated Polypeptide 1 (LAP1) Interactome and Its Functional Features. *Membranes (Basel)* 6(1). doi: 10.3390/membranes6010008.

Silver, J.K., and Lux, W.E. (1994). Early onset dystonia following traumatic brain injury. *Arch Phys Med Rehabil* 75(8), 885-888.

Spagnol, S., and Dahl, K. (2014). Active cytoskeletal force and chromatin condensation independently modulate intranuclear network fluctuations. *Integr Biol (Camb)* 6(5), 523-531. doi: 10.1039/c3ib40226f.

Stephens, A.D., Banigan, E.J., Adam, S.A., Goldman, R.D., and Marko, J.F. (2017). Chromatin and lamin A determine two different mechanical response regimes of the cell nucleus. *Mol Biol Cell* 28(14), 1984-1996. doi: 10.1091/mbc.E16-09-0653.

Stewart-Hutchinson, P., Hale, C., Wirtz, D., and Hodzic, D. (2008). Structural requirements for the assembly of LINC complexes and their function in cellular mechanical stiffness. *Exp Cell Res* 314(8), 1892-1905. doi: 10.1016/j.yexcr.2008.02.022.

Stoica, B.A., and Faden, A.I. (2010). Cell death mechanisms and modulation in traumatic brain injury. *Neurotherapeutics* 7(1), 3-12. doi: 10.1016/j.nurt.2009.10.023.

Swift, J., Ivanovska, I., Buxboim, A., Harada, T., Dingal, P., Pinter, J., et al. (2013). Nuclear lamin-A scales with tissue stiffness and enhances matrix-directed differentiation. *Science* 341(6149), 1240104. doi: 10.1126/science.1240104.

Tyler, W. (2012). "The mechanobiology of brain function.", in: *Nat Rev Neurosci.*).

Van de Vosse, D.W., Wan, Y., Wozniak, R.W., and Aitchison, J.D. (2011). Role of the nuclear envelope in genome organization and gene expression. *Wiley Interdiscip Rev Syst Biol Med* 3(2), 147-166. doi: 10.1002/wsbm.101.

Verbeek, D., and Gasser, T. (2016). Unmet Needs in Dystonia: Genetics and Molecular Biology-How Many Dystonias. *Front Neurol* 7, 241. doi: 10.3389/fneur.2016.00241

Vergnes, L., Péterfy, M., Bergo, M., Young, S., and Reue, K. (2004). Lamin B1 is required for mouse development and nuclear integrity. *Proc Natl Acad Sci U S A* 101(28), 10428-10433. doi: 10.1073/pnas.0401424101.

Wang, Y., Jiang, J., He, L., Gong, G., and Wu, X. (2018). Effect of lamin-A expression on migration and nuclear stability of ovarian cancer cells. *Gynecol Oncol*. doi: 10.1016/j.ygyno.2018.10.030.

Weisheit, C., Pappas, S., and Dauer, W. (2018). Inherited dystonias: clinical features and molecular pathways. *Handb Clin Neurol* 147**,** 241-254. doi: 10.1016/B978-0-444-63233-3.00016-6.

Wilson, K.L., and Berk, J.M. (2010). The nuclear envelope at a glance. *J Cell Sci* 123(Pt 12)**,** 1973-1978. doi: 10.1242/jcs.019042.

Wray, S., Self, M., Consortium, N.P.s.D.i., Consortium, N.H.s.D.i., Consortium, N.A.i., Lewis, P.A., et al. (2012). Creation of an open-access, mutation-defined fibroblast resource for neurological disease research. *PLoS One* 7(8)**,** e43099. doi: 10.1371/journal.pone.0043099.

Yokoi, F., Yang, G., Li, J., DeAndrade, M., Zhou, T., and Li, Y. (2010). Earlier onset of motor deficits in mice with double mutations in Dyt1 and Sgce. *J Biochem* 148(4)**,** 459-466. doi: 10.1093/jb/mvq078

Zhao, C., Brown, R., Chase, A., Eisele, M., and Schlieker, C. (2013). Regulation of Torsin ATPases by LAP1 and LULL1. *Proc Natl Acad Sci U S A* 110(17)**,** E1545-1554. doi: 10.1073/pnas.1300676110.

Zuleger, N., Robson, M.I., and Schirmer, E.C. (2011). The nuclear envelope as a chromatin organizer. *Nucleus* 2(5)**,** 339-349. doi: 10.4161/nucl.2.5.17846.

Cellular mechanical stability is inherent property of cells that is implicated in various physiological processes as well as disease pathologies[1,2]. Given the increasing need to develop novel therapeutic strategies in various disease contexts, characterizing cells based on the label-free biomarker, mechanotype, offers an exciting avenue for scientific research and drug discovery. In this dissertation, I present a novel high-throughput mechanotyping platform that is an essential step towards harnessing cellular mechanotype for screening applications. I have demonstrated how the PMF mechanotyping technology can be applied to various cell types (epithelial, mesenchymal, and fibroblasts), different types of cancer cells (ovarian[3], breast[4,5], and prostate[5]), including both established cell lines as well as patient-derived cells. While this dissertation investigates cell mechanotype in the context of cancer and dystonia, the PMF technology has promising potential for wider-scale translation to other disease systems (**Figure 1**).

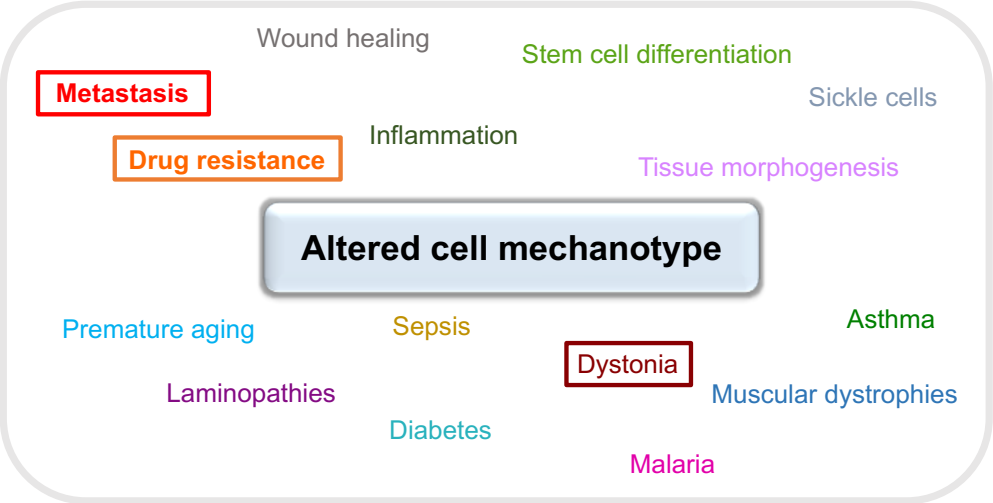

Figure 1. Altered cell mechanotype is implicated in various physiological processes and disease states.

The development of the high-throughput mechanotyping platform also enables investigation of molecular mediators of cell mechanotype. By identifying lead compounds from the deformability-based screen and analyzing molecular targets of the hits, my work contributes to building a

systems-wide understanding of molecular mediators of cancer cell mechanotype. In addition, my targeted study of a panel of specific nuclear envelope and LINC complex proteins (**Figure 2**) lays a foundation for future investigations of the role of nuclear-cytoskeletal connectivity in regulating cancer cell mechanotype. While that study focused on fibroblast cells in the context of dystonia, molecular mediators of mechanotype are generally highly conserved across cell types. An important question for future studies is how mechanotype contributes mechanistically to disease phenotypes. For example, in dystonia altered nuclear-cytoskeletal connectivity impacts mechanosensation, cell adhesion and survival. The requirement of LINC complex proteins for cell mechanotype is further substantiated by findings through a collaborative project that disruption of the inner nuclear membrane protein, emerin, makes prostate cancer cells more deformable and more invasive[5]. Cancer cells across various types of cancers exhibit altered nuclear structure and morphology, in addition to aberrant nuclear envelope protein expression[6]. Previous studies report that cancer cells exhibit increased nuclear rupture when migrating through micro-constrictions[7,8]. Taken together, findings in this dissertation facilitate future investigation into the link between cell mechanotype, nuclear-cytoskeletal connectivity, mechanosensation, cell migration, adhesion, and survival.

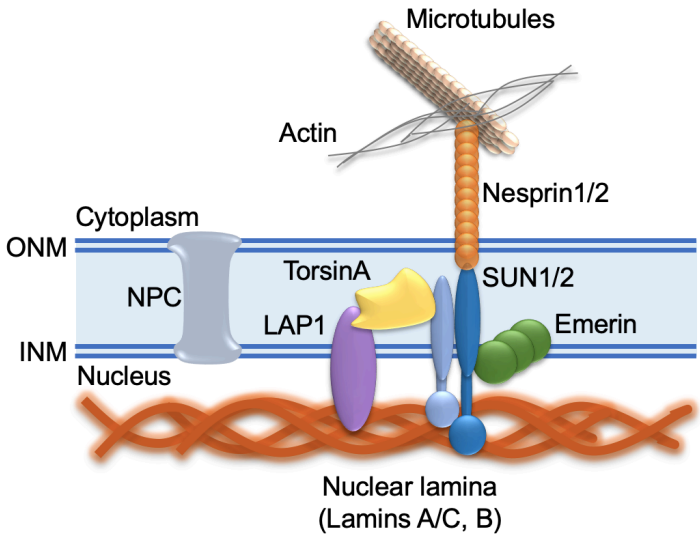

Figure 2. Linkers of nucleoskeleton and cytoskeleton (LINC complex).

References

1. S. D. Thorpe and D. A. Lee, *Nucleus*, 2017. Dynamic regulation of nuclear architecture and mechanics-a rheostatic role for the nucleus in tailoring cellular mechanosensitivity. **8**(3): p. 287-300.
2. D. E. Jaalouk and J. Lammerding, *Nat Rev Mol Cell Biol*, 2009. Mechanotransduction gone awry. **10**(1): p. 63-73.
3. D. Qi, N. Kaur Gill, C. Santiskulvong, J. Sifuentes, O. Dorigo, J. Rao, B. Taylor-Harding, W. Ruprecht Wiedemeyer and A. Rowat, *Sci Rep*, 2015. Screening cell mechanotype by parallel microfiltration. **5**: p. 17595.
4. T. H. Kim, N. K. Gill, K. D. Nyberg, A. V. Nguyen, S. V. Hohlbauch, N. A. Geisse, C. J. Nowell, E. K. Sloan and A. C. Rowat, *J Cell Sci*, 2016. Cancer cells become less deformable and more invasive with activation of beta-adrenergic signaling. **129**(24): p. 4563-4575.
5. M. Reis-Sobreiro, J. F. Chen, T. Novitskaya, S. You, S. Morley, K. Steadman, N. K. Gill, A. Eskaros, M. Rotinen, C. Y. Chu, L. W. K. Chung, H. Tanaka, W. Yang, B. S. Knudsen, H. R. Tseng, A. C. Rowat, E. M. Posadas, A. Zijlstra, D. Di Vizio and M. R. Freeman, *Cancer Res*, 2018. Emerin Deregulation Links Nuclear Shape Instability to Metastatic Potential. **78**(21): p. 6086-6097.
6. A. Mejat and T. Misteli, *Nucleus*, 2010. LINC complexes in health and disease. **1**(1): p. 40-52.
7. C. Denais, R. Gilbert, P. Isermann, A. McGregor, M. te Lindert, B. Weigelin, P. Davidson, P. Friedl, K. Wolf and J. Lammerding, *Science*, 2016. Nuclear envelope rupture and repair during cancer cell migration. **352**(6283): p. 353-8.
8. C. Denais and J. Lammerding, *Adv Exp Med Biol*, 2014. Nuclear mechanics in cancer. **773**: p. 435-70.